SAPIENZA
UNIVERSITÀ DI ROMA

Elasto-magnetic waves in metamaterials: physics and modelling

Doctorate school in Mechanical Engineering

Dottorato di Ricerca in Meccanica Teorica e Applicata – XXXI Ciclo

Candidate

Federica Mezzani

ID number 1086428

Thesis Advisor

Prof. Antonio Carcaterra

Co-Advisor

Prof. Emer. Aldo Sestieri

October 2018

Elasto-magnetic waves in metamaterials: physics and modelling
Ph.D. thesis. Sapienza – University of Rome

This thesis has been typeset by LaTeX and the Sapthesis class.

Version: April 2, 2019

Author's email: federica.mezzani@uniorma1.it

Contents

List of Figures

List of Tables

Abstract

The present work is framed in the wide topic of metamaterials. New elements portray this investigation with respect to what already existing in the current worldwide scenario. Indeed, the attention is focused on elastic metamaterials, with the idea to control wave propagation within the structure in terms of wave targeting, wave stopping and wave absorption. This is a novelty, since the concept of metamaterials is usually related to electromagnetic applications, for which all the uncommon effects, as for instance the invisible cloaking, are mainly related to the negative refraction index. A simple one-dimensional structure is analysed. More than the short-range elastic constitutive relationship, a nonlocal new long-range elastic material is here considered. This deeply affects and changes the topology of the system, leading to unexpected propagation phenomena. A mathematical model, based on the nonlocal elasticity theory of Eringen, is considered. The long-range interaction term appears as an integral function that induces a nonlinear characteristic to the conventional equation of motion. Special types of forces are chosen to model the long-range term, as they not only accurately model the elastic forces, but also lend themselves to analysis by Fourier transform. Closed form analytical solutions are achieved and it is the first time that such type of problem is so exhaustively examined. Indeed, long-range interactions have already been investigated, first by V.E. Tarasov, then by Zingales. However, Tarasov developed an analysis on the purely static response of structures, whilst this work discusses its dynamic behaviour, and Zingales performed only numerical solutions, which prevent a thorough understanding, and is mainly interested in modal analysis. The results are discussed in terms of modal analysis, dispersion relationship and propagation. It can be seen how the introduction of unconventional connections affects the typical behaviour of the structure and new phenomena, as hypersonic and superluminal propagation and negative group velocity arise. The analysis has been extended to a twin system, composed by two identical waveguides, with no structural coupling, but mutually coupled only through the long-range characteristic. An experimental campaign concludes the work. A twin waveguide system has been realized by 3D printing; several magnet holders and metallic strips acting as springs are used so to reproduce the mathematical model. The magnetic coupling recreates the long-range interaction. Different types of excitations have been applied to the primary waveguide, so to retrace first the complex frequency response and secondly the dispersion relationship. First results, even though rough, exhibit a damped response on the main waveguide, and a more complex response in the secondary waveguide, in agreement with what analytically observed.

Acknowledgments

I have always found hard to express what I think, to find the appropriate words, and so many people have helped me in this journey that it feels strange to capture how thankful I am in few lines. Here is my best attempt...
My first thought goes to Prof. Antonio Carcaterra. He has been my (our) mentor and guide. His genius and his curiosity, his way to share his passion have been teachers of life, more than just work. He taught me how to be a leader, not as a commander, but as the first person that makes the effort, that truly cares about the people he has around. He is the never ending source of inspiration and he is the paradigm of the professor I want to become. I thank Prof. Aldo Sestieri, because he always reminds me to be believe in myself and to let my unconventional way of being an engineer free to express itself. I must thank them because eventually they make me keep dreaming that, for how hard the path I have chosen will be, I can still find my way through, and if someone is so great in keeping dreams alive, then not all the words in the world could ever be enough.
I want to thank the group of Technion, Israel Institute of Technology. Prof. Izhak Bucher, Ran, Harel, Amit, Eyal, Solly, to you all, Toda raba. I will never forget how welcoming Prof. Bucher has been. Proud of his country and his group, he made us feel part of it and impatient to learn more everyday. I thank Ran for all his answers and for advising me to never stop asking questions. I thank Harel for his support, his laughters, his friendship. He reminds me to never take life too seriously. I thank Eyal for finding time for the political conversations and for explaining to me the "weird" world of the finite element analysis. I thank Amit for his astounding kindness and eventually I thank Solly and Yoav for patiently share their knowledge. I thank you all for the Hebrew lessons!! You showed us a side of Israel we would not have seen otherwise, and I will never forget it.
I thank my colleagues, Manuel, Dario, Leandro, Amir, as an effervescent workplace has no price. A special thank to Elena and Lina, who became friends, more than colleagues.
I thank my family and my boyfriend for their unquestionable support during all these years, because they will always be there for me and they trust me and believe in me no matter what.
My last thought, not because less important, but rather because special, goes to Sara and Francesco. We shared this long journey. We lived it all together, with his cheerful moments and with the most uncomfortable ones. I still do not know whether the choice of a common topic was the most appropriate one, but I know that it has given me the chance to call myself into question and to improve myself everyday. We are so different from each other, but in this, we have found our strength.

Chapter 1

Introduction and motivations

The goal of this work is to define and present the universal propagation properties of long-range interactions embedded within an elastic metamaterial. Long-range interactions and metamaterials represent one of the most powerful paradigms of modern science and technology. The plethora of applications, often interwoven to the world of micro- and nano-scale, is not only promising whatever field they are applied to, but is close to be striving imagination: biological material reconstruction, cancer detection [1], stealth technology for defence systems [2], submarine invisibility to sonar detection [3], microwave hyperthermia for malignant tumour treatment [4], swarm dynamics [5], DNA communications monitoring [6] represent only a small window over the vast sphere of metamaterials and long-range interactions.

The concept of "meta"-material derives from new propagation properties ensuing from new type of connections among the elementary components of a structure. Metamaterials are artificial composites whose properties, which are not yet found in nature, derive from the newly designed structure and not from the original components. The growing interest from the scientific community on these new materials derive from their flexible usability and, in some cases, from their capability of interaction with mechanical waves. A proper definition is given by [7]:"...They are obtained by suitably assembling multiple individual elements constructed with already available microscopic materials, but usually arranged in (quasi-)periodic sub-structures. Indeed, the properties of metamaterials do not depend only on those of their component materials, but also on the topology of their connections and the nature of their mutual interaction forces. In literature there is currently specified a particular class of metamaterials, so called mechanical metamaterials, those in which the particular properties which are "designed" for the newly synthesized material are purely mechanical".
Metamaterials represent a rather new science, though extensively studied. The subject involves mainly acoustic and electromagnetic metamaterials, for which the atypical refraction index produces uncommon effects and opens to new technological developments, as the chance to achieve invisible cloaking [8] or holographic images [9]. When dissipation and diffraction [10–14] intervene, anomalous effects involve wave propagation with negative group velocity, light stopping [15–17]

and superluminal speed [18]. The unique material properties now obtainable with acoustic metamaterials [19] have led to unprecedented control of acoustic wave propagation, resulting in many applications including acoustic cloaking, also for underwater uses [20–22]. The increasing enhancement of additive manufacturing and micro-, nano- technologies [23,24], and the consequent complex microstructures these materials are composed by support the achievement of particular dynamic behaviours, as unusual wave propagation [25] and exceptional dissipation features [26–29], i.e. all those phenomena classical dynamic can describe only by introducing unconventional mathematical models [7,30,31]. In mechanics, metamaterials can be obtained through negative effective parameters as mass, elastic modulus or anisotropic mass [32,33], but they could also be promoters of micropolar, higher-gradient and nonlocal elasticity [7,34–36].

In this context, metamaterials are designed as elastic structures in which the introduction of magnetic inclusions generates long-range interactions, overcoming the conventional concept of a system dynamics ruled by first-neighbour interplay and defining the category of the *elastic* metamaterials. The ability of the metamaterials of interaction with mechanical waves and their specific design induce singular properties responsible of the manipulation of waves: by absorbing, attenuating, blocking or deforming waves, it is possible to gain benefits that go beyond what can be usually achieved with conventional materials. The propagation control is founded on the modification of electromagnetic couplings [37], which have a clear effect on the propagation parameters and on the identification of an appropriate combination of frequency and dipole momentum so that a specific propagation behaviour can be performed.

As explained, the introduction of long-range connections within the conventional network of a material produces an alteration of the intrinsic topology of the system. If the obtained morphological scheme results in a repeating periodic pattern and if these modifications happen to be so entangled that the physical and mechanical properties of the final arrangement does not depend on the original separated configurations, but only on the new composition, doubtless the new object is a metamaterial.

Long-range schemes can appear in several shapes. A general modelling of interaction can be applied both to metamaterials and to the dynamics of a population. In a three-dimensional space and in a body characterised by a classical elastic connections, each particle is connected with the two neighbours in each direction, which means that each particle is connected with six surrounding particles.
Additive manufacturing and manipulation at microscopic level opens the chance to change the topology of a system and a question naturally arises: which type of collective motion can be obtained?
Long-range interactions can be produced either naturally, embedding external inclusions, sources of far-distance forces, as magnetic intrusions or electric charges, or artificially, by changing the elementary matrix of a material, creating, manipulating and expanding the already existing connections.
The basic foundation behind long-range interactions stands in the fact that each

particle exerts and communicates forces and that each connection between particles is a communication channel, through which information is carried. Furthermore, the information is provided in terms of the intensity of the force and the delay time, due to the finite speed of the travelling information.
The topic of long-range interactions is widely investigated and there is no science that can avoid the study of their effects. Even two of the fundamental forces, the gravitational and electromagnetic interactions, produce significant long-range forces, whose effects can be seen directly in everyday life. Long-range interactions represent an object that cannot be neglected if one is willing to portray the surrounding environment. Long-range interactions involve the outer space discoveries, and gravitational waves are *non solum* the most recent breakthrough in modern science, *sed etiam* one of the greatest exemplification of the power of far-distance forces, able to be messenger of information that not even light, in this case, could carry. It is exactly the long-range property of the gravitational force that has been the key to open a new science, the multi-messenger astrophysics [38], but also in several other fields they brought important discoveries, even though their presence is more subtle. In mechanics, Kröner [39] has been one of the first to introduce the concept of long-range interactions, applied to the strain energy of a deformed material. Eringen created a whole theory [35, 36, 40, 41] about the effects of nonlocalities, and its theory has been inspiration for many future works [42–47]. Tarasov [48–54] used long-range interactions to investigate the static response of systems, through the mean of fractional calculus. In recent years, studies of long-range interacting (LRI) systems have taken center stage also in the arena of statistical mechanics and dynamical system studies, due to new theoretical developments involving tools from as diverse a field as kinetic theory, non-equilibrium statistical mechanics, and large deviation theory, but also due to new and exciting experimental realizations of LRI systems [55].
Many branches of science deal with interconnections between basic elements, and most of the times the used communications pattern are complicated to analyse. This requires simplifications, as the hypothesis of a range of action of the interchange forces considerably short with respect to the dimensions of the system they belong to. If for many years this approach has quenched the thirst of knowledge, the new theoretical discoveries and the technological development claim a review of the fundamental theories from a different point of view and deeper investigations. Indeed, it happens very often that general models accounting only for short-range interactions reveal to be not accurate enough. The introduction of long-range forces provides new schemes that are well adapted to describe the real nature of the connections [56–59].
Even if long-range interactions are a natural essence of branches as chemistry [60–65] and quantum physics [66, 67], other sciences, from physics [68], to genetics [69], nano-science [70], optics [71–73] and swarm dynamics [74–76] started to introduce this concept in their studies. Beyond physics, the dynamics of population has a very interesting aspect that relates to the interaction range. Recent studies in crowd dynamics [77] propose models of social forces including repulsive or attractive actions, and these models can be used to predict catastrophic scenarios [78]. Traffic modeling is one of the possibilities these models offers [79]. This should not surprise. Even the mathematical approach used in this thesis to model waves generated

by a population of particle could be interpreted as the collective behaviour of a population of individuals, the mutual interactions of which produce faster or slower social effects on the global response of the community.

Even in the landscape of recent investigation of elastic metamaterials [80], the correlation between waves and nonlocality is not directly addressed and the scientific literature does not report results on anomalous elastic wave propagation analogous to those found in electromagnetics. Even though nonlocal interactions have been widely investigated [81], the absence of general results for dispersive properties in nonlocal materials is justified by the complexity of the governing equations of motion. Indeed, to correctly describe the nature of the interactions and the wave propagation integral-differential equations in space and differential in time are needed.
The core of this work is the merging of long-range interactions and elastic metamaterial. This bond defines a completely new paradigm in structural mechanics, intrinsically based on local short-range particle interaction. The features of long-range forces produce very new mechanical coupling effects, which can be both *intra-body* and *inter-body*, as for instance the case of coupled waveguides: waves generated in one of the beam propagates also in the second and vice versa, creating a new effect named twin-waves [82, 83]. Furthermore, a thorough analysis of the response of such structures based on inverse problem solutions can lead to the definition and the consequent realization of a new type of material, able to delineate a specific path of waves determined starting from the control of macroscopic physical parameters. The goal is to ensure isolation in those portion of the structure more sensitive to the vibrational motion and waves would be funnelled towards more resistant areas.

This work reports new results for wave propagation in elastic metamaterials, characterized by long-range interactions among elementary particles. The presence of such type of coupling, possible in elastic, acoustic as well as in electromagnetic and optical systems, produces integral-differential equations. The theoretical presented background has wider potential uses. In fact, the long-distance interaction is a recurring challenge in physics. Statistical mechanics of complex systems is classically based on Boltzmann theory and the collision integral represents typical "short-range" interactions. The Vlasov theory [84] attacks long-range interaction for the evaluation of the probability density of a system of charged particles as electrons or plasma ions. Long-range thermodynamic [85] produces unusual effects as negative specific heat, anomalous diffusion, ergodicity breaking and new regimes in cold gases. The model here introduced provides an interpretation of deterministic effects that can be expected for long-range interactions. These interactions, whether they occur within a single structure or whether they are meant to couple distant objects, modify the topology of the connections and, thus, the dynamic response of the system, and the result unveils special kind of waves, enlightening wave stopping, negative group velocity, cut-off and superluminal propagation.

A general map of the possible connectivity templates has been presented in [86], and all types of possible connection topologies can be reduced in four main categories,

namely: i) master-cluster connection, already introduced in [28, 29, 87–90], ii) all-to-all connection, common in quantum physics [91, 92] iii) all-to-all with reduced length of interaction, and iv) random sparse connection.
The connectivity matrix is the element that exemplifies the topology of a structure based on the connections existing between particles and in the case of classical elastic connections, it reduces to the conventional, tridiagonal stiffness matrix. The long-range connections have the effect to complete the out-of-diagonal elements, according to their type, shape and connectivity characteristics. Probably, among all, the one-to-all connections enjoys the most a widespread attention, as they can be related to the concept of "energy sinks", an alternative to the conventional way of absorbing vibrations. The several experiments carried out [26, 30, 93–95] consider a set of non-damped harmonic oscillators, linked to a master structure, defined by a single degree of freedom. The set of oscillators behaves as an energy sink, absorbing and holding vibrations from the primary structure. There is no dissipation of energy in the classical sense of heat transformation, however the energy remains in the energy sinks for a sufficiently long time so that one can consider damped the oscillatory motion of the main structure. Note that the long-range interactions existing in an "energy sink" system are of an elastic type, which implies linear governing equations of motion. Long-range interaction of contact-less type, as the ones here considered, have a nonlinear nature, which has reflection on the type of applicable equations.
In [86], the dynamics of all these systems is synthesised through a unique integral-differential equation:

$$L_x^{(n)}\{w(x,t)\} + m' \frac{\partial^2 w(x,t)}{\partial t^2} + K(x,t) * *w(x,t) = 0 \tag{1.1}$$

The inertia term appears as second order in time t, the n-th order differential operator $L_x^{(n)}$ is with respect to the space variable x, the double convolution implies a transform operation involving both space and time and K depends on the nature of the connections. For purely elastic connections $K(x,t) * *w(x,t)$ reduces to a space operation only, but the time dependence cannot be neglected in case of a delayed time information.
The great advantage of such type of formulation lies in the fact that to understand the dynamic of the system, the detailed mechanics of the single components, which might be hidden and inaccessible to direct measurements, is not required. In fact, the investigation of the dispersion relationship, associated to equation (1.1), is sufficient to analyse the global behaviour, and by simply analysing the group velocity, the propagation behaviour of such systems can be fully illustrated. Indeed, interpreting the group velocity as a comparison between the short-range and long-range actions, the propagation scenarios can be discussed in terms of a single parameter, representative of the strength of the long-range forces, compared to classic elastic ones. Wave-stopping occurs when an essential balance between short-range and long-range forces is determined: the energy does not propagate along the structure due to the absence of reflections and echoes at boundaries. Negative group velocity is obtained if the effects due to the two forces appear as opposite, and in this case this contrast is reflected on the propagation direction of waves and energy, opposite as well with respect to each other. At last, specific conditions might also lead to

hypersonic velocity.
Eventually, long-range interactions are presented and interpreted as an operator which exponentially decays with the distance, whose intensity can be either positive, as for attractive force, or negative, as for a repulsive interaction and it is controlled by a single parameter. The magnetic interaction is a physical example of long-range interactions.
This thesis is structured in five chapters: after the introduction, in Chapter 2, the linear problem of elasticity proposed by Navier and the Eringen's nonlocal theory of elasticity are presented as basic foundation of the applied mathematical model. Besides, an overlook over theories about long-range interactions is proposed as useful not only to provide a complete background, but also to highlight the novelties of the presented mathematical approach. Chapter 3 focuses on the effects of long-range interactions on the equation of motion, beyond the concept of classical elasticity. Chapter 4 presents the application of the mathematical model to the simple one-dimensional problem. The propagation behaviour is analysed for special kernels for the long-range interactions, i.e. Gaussian-like and Laplace-like forces, able to disclose analytical solutions to the equation of motion. The surprising propagation effects, as wave-stopping, negative group velocity and superluminal propagation, are discussed in details in this chapter, but further developed in Chapter 5, when the mathematical approach is applied on a *twin system*, where two rod-like structures are coupled with each other, thanks to the magnetic interaction only. The mathematical analysis anticipates the existence of unconventional propagating phenomena, which are corroborated by numerical simulations. Finite elements analysis and an experimental campaign complete the investigation. At last, the future developments of this thesis are discussed in the Conclusions.

Chapter 2

State of art on long-range forces

The present work investigates elastic metamaterials, in which the presence of long-range interactions, due to magnetic inclusions, gives rise to unconventional effects on the dynamic of a simple one-dimensional systems.
In this chapter, the guidelines of the used mathematical model are exposed and the linear problem of elasticity proposed by Navier is presented as a fundamental background, together with an overlook over theories about long-range interactions.
The extension of the concept of local elasticity is a process started many years ago. Already in 1953, dealing with periodic structures of different kinds, Brillouin dedicates attention to a larger length of interaction among elementary particles. In [96], he tackles the problem of wave propagation in several cases and when the interaction length is not reduced to first neighbours only, but it spreads over L elements, he obtains a relation between the frequency ν and the wavenumber $a = \frac{1}{\lambda}$ as the following:

$$\pi^2 r^2 M = \sum_{0<m<L} U''_m \sin^2 \pi amd = \frac{1}{2} \sum_{0<m<L} U''_m \left(1 - \cos 2\pi amd\right) \tag{2.1}$$

where U is the energy of interaction between two particles, expressed as a potential function that depends on the mutual distance, U' and U'' are its derivatives $\frac{\partial U}{\partial r}$ and $\frac{\partial^2 U}{\partial r^2}$. Since $\cos\left(2\pi amd\right)$ can be expanded as polynomial, the frequency itself is a polynomial of degree L in $\cos\left(2\pi ad\right)$. This equation means that "ν is a single-valued function of a, but a is not a single-valued function of ν" ([96]) and hence, for any frequency, there are L solutions of a. Those solutions need not all to be real, but they can in general be complex and waves propagating along the lattice are associated to real a, and waves decaying exponentially from the source point are related to imaginary or complex a. In this way, Brillouin shows how even a "simple" one-dimensional problem can lead to a more complex treating if a higher number of connections are included: "*In the case of interactions between nearest neighbours only, the boundary conditions were simple: we had only to specify the motion of the first particle. However, added interactions complicate the procedure, and the boundary conditions must be specified over a length Ld of the lattice.*"
In 1967, Kröner [39] analyses the strain energy of a deformed material in which

the spatial interactions are of a long-range type. He provides a classification of this energy based on the form in which it is expressed: a differential or *multipolar* form of a single volume integral containing gradients of the displacement up to infinite order, suitable to very small scale, almost atomic, range of interaction, and an integral form or *nonlocal* with a double volume integral, preferable to describe electric cohesive forces, seen as two-point material tensors.
However, the most popular theory about the extension of the classical concept of elasticity has been developed by Eringen in [35,36,41] and, since it inspired many authors and this work too, a paragraph is dedicated to its theory.
Furthermore, two remarkable examples of how the nonlocal elasticity theory can be successfully applied to long-range interactions are illustrated, as they show common elements with the here presented investigations. In [49–53], Tarasov presents a mathematical model based on fractional calculus, in which nonlocal connections affect the static response of the structure. Zingales in [44–47,97,98] discusses how the dynamic behaviour, analysed in terms of integral-differential equations, is influenced by this type of interactions, but only numerical solutions confirm his theory. In light of the exposed theories, the key elements of the present work and its novelties are hereafter illustrated.

2.1 Navier-Cauchy formulation

The problem of the elasticity theory is to determine the motion and the deformation of an elastic solid that undergoes external loads, as long as equilibrium laws and constitutive relationships remains valid. It considers only problems in which it is reasonable to assume displacements and deformations to be much smaller than the significant dimensions of the considered body and the constitutive relation can be translated into the Hooke's law.
The equation of the displacement field is obtained classically from the general elasticity problem. It is composed by equations of equilibrium, the pointwise compatibility and the constitutive relationships. For a three-dimensional system, this problem contains 15 unknown fields (displacement, stress and strain) and, even though an analytical solution is theoretically possible given the 15 available equations, the problem remains complex and requires a reduction to a fewer number of equation and unknowns. This procedure leads to the definition of the displacement field, as long as displacements are the primary unknowns of the formulation and are known everywhere on the boundary.
In the following presentation of the problem the operator ∇^2 is used for the Laplacian operator, ∇ for the gradient operator, $\nabla\cdot$ indicates the divergence, λ and μ are the Lamè constants; the rest of the symbols have an obvious meaning and are no further discussed.
The governing equations of the linear elastic problem are:

- the equilibrium equations

$$\frac{\partial \sigma_{ij}}{\partial x_j} + f_i = 0 \tag{2.2}$$

  which are three equations containing six unknowns

- pointwise compatibility

$$\varepsilon_{ij} = \frac{1}{2}\left(\frac{\partial u_i}{\partial x_j} + \frac{\partial u_j}{\partial x_i}\right) \tag{2.3}$$

  which provides six equations in nine unknowns

- constitutive laws

$$\sigma_{ij} = C_{ijkl}\varepsilon_{kl} \tag{2.4}$$

  or, in case of linear isotropic elasticity

$$\sigma_{ij} = \lambda\varepsilon_{kk}\delta_{ij} + 2\mu\varepsilon_{ij} \tag{2.5}$$

  which complete the problem introducing six equations, but no other unknowns.

Eventually, the boundary conditions can be of two types, according to whether they are expressed in terms of displacement (*essential boundary conditions*) $\bar{\boldsymbol{u}}$ imposed on the portion of the surface of the body ∂B_u, i.e. $u_i = \bar{u}_i$, or in terms of traction (*natural boundary conditions*) $\bar{\boldsymbol{t}}$ imposed on the portion of the surface of the body ∂B_t, namely: $n_i\sigma_{ij} = t_j = \bar{t}_j$.
The necessary conditions for the existence and uniqueness of the solution have been intensely discussed and it is proven how they are related to the positive definiteness of the stiffness tensor. This translates into the positiveness of the bulk and shear moduli $K = \dfrac{E}{3(1-2\nu)} > 0$, $G = \dfrac{E}{2(1+\nu)} > 0$ and hence to a restriction on the Poisson modulus: $-1 < \nu < 0.5$.
To obtain the displacement field, stress and strain must be eliminated from the general problem, through a proper combination of the given equations. Indeed, by substituting firstly equation (2.4) into equation (2.2) and then (2.3) into (2.2) again, one achieves the so-called Navier equations:

$$\frac{\partial}{\partial x_j}\left(C_{ijkl}\frac{\partial u_k}{\partial x_l}\right) + f_i = 0 \tag{2.6}$$

When conditions of isotropic elasticity occur and applying the same procedure as for the general case, the stress becomes:

$$\sigma_{ij} = \lambda\varepsilon_{kk}\delta_{ij} + 2\mu\varepsilon_{ij} = \lambda\frac{\partial u_k}{\partial x_k}\delta_{ij} + \mu\left(\frac{\partial u_i}{\partial x_j} + \frac{\partial u_j}{\partial x_i}\right) \tag{2.7}$$

and the resulting equilibrium equation is:

$$0 = \frac{\partial\sigma_{ij}}{\partial x_j} + f_i = \lambda\frac{\partial^2 u_k}{\partial x_j\partial x_k}\delta_{ij} + \mu\left(\frac{\partial^2 u_i}{\partial x_j^2} + \frac{\partial^2 u_j}{\partial x_i\partial x_j}\right) + f_i = \lambda\frac{\partial^2 u_k}{\partial x_i\partial x_k} + \mu\left(\frac{\partial^2 u_i}{\partial x_j^2} + \frac{\partial^2 u_j}{\partial x_i\partial x_j}\right) + f_i \tag{2.8}$$

The expression of the field displacement for a three-dimensional, unbounded elastic medium can then be easily obtained in its component form:

$$(\lambda+\mu)\frac{\partial^2 u_j}{\partial x_i\partial x_j} + \mu\frac{\partial^2 u_i}{\partial x_j^2} + f_i = 0 \tag{2.9}$$

or in its vectorial counterpart:

$$(\lambda + \mu)\,\nabla\,(\nabla \cdot \boldsymbol{u}) + \mu\nabla^2\boldsymbol{u} + \boldsymbol{f} = \boldsymbol{0} \tag{2.10}$$

As final step, expliciting the Lame constants, as parametric functions of the Young's modulus E, i.e. $\lambda = \dfrac{\nu E}{(1+\nu)(1-2\nu)}$ and $\mu = \dfrac{E}{2(1+\nu)}$, the Navier's equations are:

$$\frac{E}{2(1+\nu)(1-2\nu)}\frac{\partial^2 u_j}{\partial x_i \partial x_j} + \frac{E}{2(1+\nu)}\frac{\partial^2 u_i}{\partial x_j^2} + f_i = 0 \tag{2.11}$$

$$\frac{E}{2(1+\nu)(1-2\nu)}\frac{\partial e}{\partial x_i} + \frac{E}{2(1+\nu)}\frac{\partial^2 u_i}{\partial x_j^2} + f_i = 0 \tag{2.12}$$

where $e = \varepsilon_{kk} = \dfrac{\partial u_k}{\partial x_k}$.
These equations, together with the inertia contribution, represent the conventional kernel of the equation of motion:

$$\rho\frac{\partial^2 u_i}{\partial t^2} - \frac{E}{2(1+\nu)(1-2\nu)}\frac{\partial^2 u_j}{\partial x_i \partial x_j} - \frac{E}{2(1+\nu)}\frac{\partial^2 u_i}{\partial x_j^2} - f_i = 0 \tag{2.13}$$

However, the contribution of long-range forces through the term $f_i = f_{iLR}$ alters the nature of the equation and, hence, of the dynamic of the system and new unconventional properties are unveiled. A general formulation of the equation of motion is in the form:

$$\rho\boldsymbol{u}_{tt} - \frac{E}{2(1+\nu)}\left[\frac{1}{(1-2\nu)}\nabla(\nabla\cdot\boldsymbol{u}) + \nabla^2\boldsymbol{u}\right] - \boldsymbol{f}_{LR} = 0 \tag{2.14}$$

where $\boldsymbol{u}_{tt}$ is the notation used for a second order time derivative.

2.2 Eringen theory of elasticity

The elasticity theory is based on two fundamental assumptions: i) the relationship between components of stress and strain is linear, and ii) only infinitesimal strains or "small" deformations (or strains) are considered. Even though this might be suitable for many engineering problems, for more accurate studies they represent a limitation.
In the nonlocal elasticity theory, the points undergo translational motion as in the classic case, but the stress at a point $\boldsymbol{x}$ depends on the strain field in a region near that point, or at every point $\boldsymbol{x}'$ [35, 36, 40, 41]. A physical interpretation sees long-range interactions intervening between points at far distance and they occur, for instance, between charged atoms or molecules in a solid.
The constitutive equation for stress is in terms of the position vector $\boldsymbol{x}$ of points in the solid, in which the Lamè coefficients for an isotropic material become spatial functions of the distance from the point under consideration in the material.
In many of his studies [40], Eringen demonstrates how the selection of an appropriate class of kernels does not need to be itad hoc, but it only needs to respect

mathematical conditions of admissibility and verifiability.
Firstly in [41], but also in [40], he presents the linearised nonlocal elasticity theory for homogeneous and isotropic elastic solids through the following set of equations:

$$t_{kl,k} + \rho\left(f_l - \ddot{u}_l\right) = 0 \tag{2.15}$$

$$t_{kl}(\boldsymbol{x}) = \int_V \alpha\left(\left|\boldsymbol{x}' - \boldsymbol{x}\right|, \tau\right) \sigma_{kl}\left(\boldsymbol{x}'\right) d\underline{V}(\boldsymbol{x}') \tag{2.16}$$

$$\sigma_{kl}\left(\boldsymbol{x}'\right) = \lambda e_{rr}\left(\boldsymbol{x}'\right)\delta_{kl} + 2\mu e_{kl}\left(\boldsymbol{x}'\right) \tag{2.17}$$

$$e_{kl}(\boldsymbol{x}') = \frac{1}{2}\left(\frac{\partial u_k(\boldsymbol{x}')}{\partial x_l'} + \frac{\partial u_l(\boldsymbol{x}')}{\partial x_k'}\right) \tag{2.18}$$

where t_{kl} is the stress tensor, ρ is the mass density, f_l is the body force density, u_l is the displacement vector, $\sigma_{kl}(\boldsymbol{x}')$ is the macroscopic stress tensor evaluated at $\boldsymbol{x}'$ and related to the linear strain tensor $e_{kl}(\boldsymbol{x}')$, μ and λ are the Lamè constants. The elastic strain is determined through a Fredholm integral equation in which the stress is defined by the convolution between the local response to an elastic strain and a smoothing kernel dependent on a nonlocal parameter.
This set of equations is not very different from the one adopted in the linear elasticity theory. The main distinctions lies in equation (2.16), which replaces Hooke's law.
It is interesting to notice that in [41] Eringen applies his theory to the case of plane waves. The experimental campaign on phonons propagating in aluminium successfully demonstrates the validity of his theory, thanks to the comparison between the dispersion relationship, given by:

$$k^2\left[1 + \sqrt{2\pi}\overline{\alpha}(k)\right] = \left(\omega / c_\infty\right)^2 \tag{2.19}$$

and the dispersion curve, obtained through the experimental campaign.
Even if Eringen does not solve analytically the dispersion relationship and no proper analysis on the characteristics of propagation is yielded, this result is still remarkable since not only it confirms the theoretical assumptions in a wide range of frequencies, but also because the obtained dispersion curve shows a trend that is unconventional with respect the one that would have been achieved through the classical linear theory of elasticity. Furthermore, it will be shown, in the following chapters, how the dispersion curve obtained by Eringen and the one associated to the case of a one-dimensional waveguide equipped with magnetic inclusions (the study case analysed in this thesis) are rather similar. This does not imply a similarity between the proposed case studies, but more the power of the nonlocal elasticity to investigate and bring to light shades that with the linear theory of elasticity would remain hidden and unnoticed.

2.3 Tarasov theory

As previously mentioned, among many authors tackling the subject of long-range interactions, Tarasov is the one who introduces the concept of long-range interactions through integral-differential equations that model the dynamic of the systems by the mean of fractional calculus [49–54, 99].

In [51], Tarasov considers discrete systems with long-range interactions and tries to define a continuous limit for the systems with long-range interactions, so to interpret continuous medium models as continuous limit of a discrete chain system. These long-range interactions of chain elements produce fractional equations for the medium model, mapped into the continuum equation with Riesz fractional derivative.
A wide class of long-range interactions that provides fractional medium equations in the continuous limit are considered, but the power-law interaction represents a special case, and its associated equation is:

$$\frac{\partial^s}{\partial t^s}u(x,t) - G_\alpha A_\alpha \frac{\partial^\alpha}{\partial |x|^\alpha}u(x,t) - F\left(u(x,t)\right) = 0 \tag{2.20}$$

with α non integer.
[54] is a rare example in which Tarasov investigates the dynamic response of the system:

$$\frac{\partial^2}{\partial t^2}\hat{u}(k,t) + J_0\hat{J}_\alpha(k)\hat{u}(k,t) - J_1\hat{u}(k,t) + J_2 F_\Delta\left\{sin\left(u_n(t)\right)\right\} = 0 \tag{2.21}$$

where $\hat{J}_\alpha(k) = 2\sum_{n=1}^{+\infty}\frac{\cos\left(kn\Delta x\right)}{n^{\alpha+1}}$ is the long-range kernel.
The main focus of his work is the definition of a transform operator able to translate the set of coupled individual oscillator equations into the continuous medium equation with the space derivative of order α, where $0 < \alpha < 2$, but $\alpha \neq 1$. However, the dynamic problem is solved only in the low frequency domain, the region for which $k \to 0$, hence in the infra-red limit, where the transformation, being an approximation, is valid, and no analysis of the dispersion relationship is presented.
The researches presented both by Eringen and Tarasov present common points: they both consider a wide class of kernels for the long-range interactions, even though major attention is preserved for power-law interactions, and they do not face, at least most of the times, the problem of the dynamic behaviour of a system; indeed, they are more focused on the static response of a structure and on a mathematical classification of the case studies.

2.4 Zingales approach

Zingales, on the other hand, investigates wave propagation in non-local elastic solids, applying Kröner–Eringen integral model of non-local elasticity in unbounded domains. He presents the problem through the Hamiltonian functional formulation, where a term additional to the elastic potential energy accounts for elastic long-range interactions [97]:

$$\rho(x)A(x)\frac{\partial^2 u(x,t)}{\partial t^2} - \frac{\partial}{\partial x}\left[E_{nl}(x)A(x)\frac{\partial u(x,t)}{\partial x}\right] + \int_a^b \bar{g}\left(x,\xi\right)\eta\left(x,\xi,t\right)d\xi = A(x)f(x,t) \tag{2.22}$$

where $E_{nl}(x)$ is the non-local elastic modulus and $\bar{g}(x,\xi)\,\eta(x,\xi,t)\,d\xi$ represents the contribution of the long-range interactions, proportional to the interacting volume. In the context of standing wave analysis, Zingales provides a weak formulation of the wave equation, able to produce only approximate analytical solutions to the governing equation. This is achievable if the long-range forces between different volume elements are modelled as central body forces applied to the interacting elements. In this way, the mechanical boundary conditions may easily be imposed because the applied pressure at the boundaries of the solid must be balanced by the Cauchy stress. Even though the results are in agreement with what predicted by the non-local integral theory of elasticity in unbounded domains, some differences arise in the case of bounded domains. Besides, the lack of closed form solutions prevents a thorough investigation of the propagation characteristics, limiting the analysis at the context of standing waves.

2.5 New open scenarios

The growing interest about metamaterials brought several research groups and universities to work on it. Different typologies of metamaterials are under investigation and they are mainly related to electro-magnetic, optical and acoustic metamaterials. This is the first time that elastic metamaterials are investigated, and for the first time the dynamic behaviour of a structure with long-range interactions, due to magnetic inclusions, is studied.
The topic of long-range interactions is not a new: mainly related to elastic connections and the concept of the energy sinks [30, 93, 94, 100], as shown in the first chapter, in recent times it has attracted the attention of other authors, as Tarasov and Zingales, taken as example as they face the problem with an approach not far with the one here used. However, none of them embrace the idea of metamaterials, and while Tarasov is only interested in long-range interactions and mainly on their effects over the static response of a structure, Zingales carries on a study in which the dynamic response is only numerically investigated.
The novelty introduced in this work is the chance to discuss the dynamic response through the analytical solutions of the obtained dispersion relationship. The proposed mathematical model is based on the nonlocal elasticity theory developed by Eringen, in which several types of long-range connections are investigated. However, even tough his study is complete from a mathematical point of view, the effect related to wave propagation are discussed only in [41]. The present work not only analyses a specific type of long-range interactions, associated to the effects of magnetic inclusions within the matrix of a conventional material, but also provides a thorough investigation of the arising propagation phenomena, suggesting a map of the possible scenarios according to the intrinsic physical properties of the system. A similar analysis was conducted by [101] and [102], but it is applied to micro and nano scales only.
This new type of interaction, together with the advantage of a detailed analysis, possible thanks to the achievement of closed form solutions, brings to light unconventional phenomena, as an infinite numerable values of the wavenumber associated to a single frequency, wave stopping and superluminal propagation that

will be discussed further on in this thesis.
However, long-range interactions are not only a mean to achieve uncommon propagating phenomena and special dynamic response. Indeed, they define a communication network. These interactions can connect elements and even separated structures, when no structural links are present or possible, as long as their mutual distance is smaller than the typical interaction length. In this scenario, the case of a twin system finds its place as extension of the single waveguide problem. The *twin-waves* is not only a theoretical dissertation; a natural application of the twin system concept are, indeed, the interface waves (propagation waves at the interface between different media), which should not be interpreted only as coupling between fields, but as long-range interacting waves. More than the novelty in itself, the communication aspect is even more interesting if one considers all its possible applications, which can spread from remote control, to control over the dynamics of populations or swarms.

2.6 Final remarks

This opening chapter introduces the fundamental basis of the proposed mathematical approach: the elasticity theory, as bequeathed by Navier and Cauchy, is further developed following the guidelines of Eringen's nonlocal theory. Furthermore, among many authors challenging the topic of long-range interactions, the works of Tarasov and Zingales are discussed as they exhibit common features with the here discussed problem. This overview has the ambition to enlighten the innovation nature of this work.

Chapter 3

A new approach to long-range metamaterials

The mathematical model presented in this work is framed in the general context of linear elasticity, introduced through Navier-Cauchy equation of motion, but further developed so to include the contribution of long-range forces. For this purpose, the nonlocal elasticity theory of Eringen is considered and, accordingly, a convolution term is introduced in the displacement field equation as interpretation of the new nonlocal properties of the system. The effect of this term is the addition of nonlinearities within the resulting integral-differential equations of motion.
The present chapter focuses on the long-range interactions, investigating their nature, beyond the concept of classical elasticity, and their effects on the equation of motion.

3.1 The nature of the force: beyond elasticity

Two main concepts are often involved when dealing with structural mechanics, namely elasticity and linearity, and when taking a closer look to relatively small problems, it sounds reasonable, in most cases, to reduce them to their simplest expression. However, linearity and perfect elasticity are approximations of the real world and many materials, defined elastic, remain purely elastic only under the specific hypothesis of small deformations.
We set the limits and the conditions under which a structure can be said linear; we manipulate reality so to be easier for us to be understood. Elasticity, even more than linearity, represents a clear example. It relies upon the idea that a body is able to resist to an external load and to recover its original shape when that force is removed. The existence of a "state of ease" of "perfect elasticity" in which "a body can be strained without taking any set" [103] implies a range delimited by the unstrained state on one side and the elastic limit on the other. Nevertheless, there are cases which bring to light the limitations of this assumption, as materials that, albeit showing a definite elastic limit, are subdued to applications causing deformations beyond that limit, or materials, as rubber, that after very large deformations, would only recover a part of it. These examples generate a new concept: the ground-position, defined as the position in which the deformation started and which differs from the

initial position. This induces a difference between deformation and strain, where the first is the global modification of the material and the latter is the recoverable part of it, when all the external forces have been removed. "The strain can differ from the deformation not only in magnitude, but also in the orientation of the principal axes" [104]. In this sense, the ground position corresponds to the unstressed state, but not to the undeformed one. A general theory of elasticity should relate the strain and both the stress by it produced and the external forces necessary to equilibrate the stress in the body, according to d'Alembert principle. The classical theory, instead, refers to the case where strain and deformation are identical and the stress-strain curve can be approximated as linear, neglecting higher order terms. This theory, that when applied to isotropic materials reduces to the well-known Hooke's law (*ut tensio, sic vis*), can be extended to fluids as well; indeed, in response to a small, rapidly applied and removed strain, non-Newtonian fluids may deform and then return to their original shape.
However, the forces that rules nature and that keep matter together overcome the limits of classical elasticity and their behaviour is strongly nonlinear. The four fundamental forces describe any physical phenomenon at any scale of distance and energy through nonlinear relations. It is fascinating to notice how the entire reality around us is pictured through a set of forces covering not only any scale, from subatomic, as the strong and weak nuclear bonding, to macroscopic scales, as the gravitational attraction and electromagnetism, but also any type of nonbonded interactions. Strong and weak interactions have a minuscule range of action, confined within the nuclear radius, whereas electromagnetism and gravitation even more are the greatest examples of long-range interactions carriers. The gravitational force runs infinitely unbounded and through gravitational waves we are able to listen to the far universe, for which light cannot be a proper messenger. Long-range interactions affect our life, generators of inextricable networks daily employed, from the social connections to the world wide web.
This is just a hint to understand that limiting the interconnections within matter to short-range interactions only is equivalent to be color blind, the boundaries would be undoubtedly defined, but all the possible shades would remain undiscovered and, even though reasonable in some cases, the overall view would still be missing. In this newly defined stage, the chance to introduce long-range forces and to go beyond the classical concept of elasticity opens new scenarios in the panorama of structural mechanics as well. The types of possible connections are wide and each one produces unique effects on wave propagation, vibration characteristics, damping and modal behaviour. Figure (3.1) presents a map, already shown in [86], of the possible topologies of connection that have in common the long-range feature and that enter the domain of the propagation in nonlocal elasticity.

- In the master-cluster scheme (3.1a), a single mass communicates with all the others and phenomenon of wave stopping arises; the energy transported along the ring, when exciting the connected mass, can stop and the excited mass does not receive any echo from the ring; irreversible energy transfer (the energy initially associated to the master particle is rapidly transferred to the cluster and an appropriate modulation of the intensity of the connections

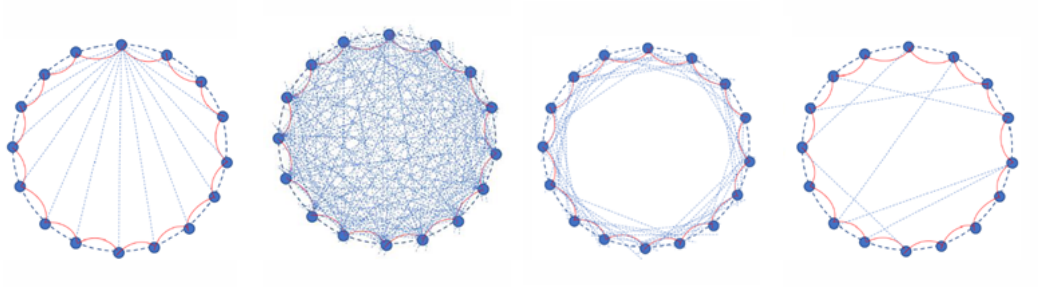

(a) master-cluster **(b)** all-to-all **(c)** reduced all-to-all **(d)** random sparse

Figure 3.1. Long-range interactionsConnection schemes

makes the process irreversible) occurs;

- The full-range scheme (3.1b) includes any connection between any arbitrary pair of particles and anomalous propagation phenomena appear, as wave stopping and superluminal propagation of waves;
- In the all-all limited range (3.1c), the same phenomena of (3.1b) appear;
- In the case of randomly sparse connections (3.1d), synchronization of the particle motion becomes relevant and no phase-delay is observed; besides, the disturbance propagates with very high speed, as consequence of the amplification of the group velocity.

The technological progress has finally reached a level that allows experimental campaigns that were just imagination until not long ago and with it the possibility to confirm a wide class of theories. 3D printers or micro-nano technologies can insert elements within conventional materials, so to produce long-range interactions, as the case here under investigation of magnetic or electric inclusions. The presence of magnetic and electrostatic interaction compels the communication between far particles and practically overcomes the limit of short-range connections of the local elasticity theory.
Perfect elastic body is an ideal concept only. The most elastic body in modern science found is quartz fibre, which is not even a perfect elastic body.
The aim of this work is to go beyond the fashion of conventional mechanics and classical elasticity. Of course there is no pretension to reconcile general relativity and quantum mechanics, but more the willingness to show how the combination of apparently different fields can yield to surprising phenomena and the greatest question about the nature of the universe might provide cues to face even common and simpler problems.

3.2 Elastic-electrical-magnetic interactions

The element that expresses the relation between the degrees of freedom of a structure and the topology of the force exchange is the connectivity matrix. The shape of the matrix depends on the nature of the force existing between particles. In discrete

dynamic systems of concentrated parameters, as masses, springs and dampers, one can reduce the connectivity matrix to a tridiagonal matrix (Figure (3.3)) with good approximation and the connectivity matrix exemplifies the stiffness matrix, since that is the one carrying the information about the connections among elements. It describes the conventional elastic interaction, modelled in Figure (3.2), and the conventional propagation in which elements out of the three main diagonals do not interfere.

When more than the classical elastic connections intervene, the connectivity matrix

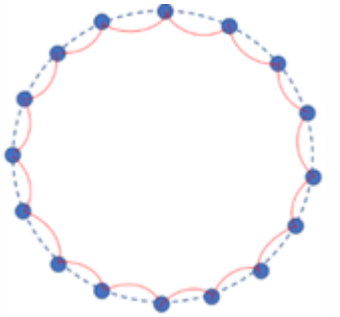

Figure 3.2. Elastic connections

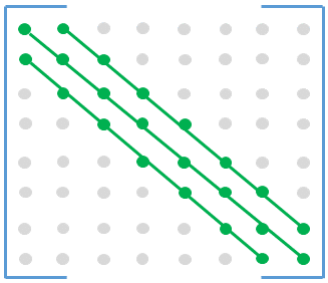

Figure 3.3. Conventional connectivity matrix

can assume a much more complex structure and, at most it could be a full matrix, if it is reasonable to assume that each element is linked with all the others. In real structures, the topology of connections is actually more sophisticated, due to the bonding among elementary particles, and the assumption of elastic connections is valid only within the hypothesis of small deformations, but this is still an approximation. Furthermore, if a structure is supplied with additional types of connection, it is apparent that the topological scheme should be carefully investigated. In this context, the attention is focused on a new type of *metamaterial*, in which the inclusion of magnetic or electric particles within the material matrix alters the nature of the structure itself, and this produces interesting effects, reason of the growing interest on this elastic *metamaterials*.

The expressions of the Coulomb forces and the dipole-dipole coupling are, respectively:

$$\boldsymbol{F}_{Coulomb} = kq_1q_2\frac{\boldsymbol{r}_1 - \boldsymbol{r}_2}{\|\boldsymbol{r}_1 - \boldsymbol{r}_2\|^3} \tag{3.1}$$

where k is the Coulomb's constant $k = \dfrac{1}{4\pi\varepsilon_0}$, ε_0 is the electric constant or absolute permittivity of free space, q_1 and q_2 are the magnitudes of the charges and $d = \|\boldsymbol{r}_1 - \boldsymbol{r}_2\|$ is the distance between the charges;

$$\boldsymbol{F} = \frac{3\mu_0}{4\pi} m_1 m_2 \frac{\boldsymbol{r}_1 - \boldsymbol{r}_2}{\|\boldsymbol{r}_1 - \boldsymbol{r}_2\|^5} \tag{3.2}$$

with μ_0 is the magnetic permeability of free space, m_1 and m_2 are the dipole momentum intensities and $d = \|\boldsymbol{r}_1 - \boldsymbol{r}_2\|$ is their mutual distance. It is clear that electric and magnetic forces spread the range of interaction, involving a larger number of elements than the elastic connections. This implies that the connectivity matrix would keep non-null elements out of the main tridiagonal band. However, even though wide, the range of interaction of these forces decays with the distance, as shown in Figure (3.4), and the coupling between particles becomes weak enough to be neglected. It is then reasonable not to include all the elements in the connectivity

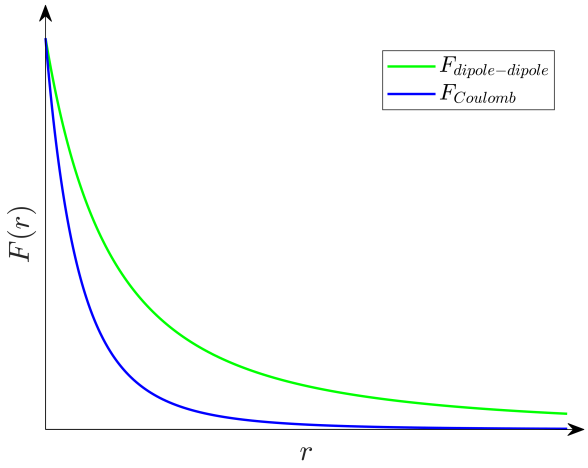

Figure 3.4. Trend of Coulomb force and dipole-dipole coupling

matrix, according to the realistic range of influence, as in Figure (3.5).
Long-range interactions are always engines of unconventional wave propagation

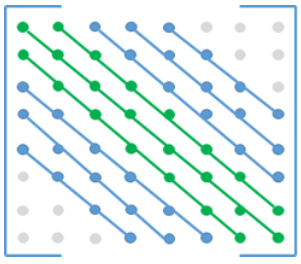

Figure 3.5. Connectivity matrix associated to electrical and magnetic interactions

phenomena, but when they are produced through elastic connections, as in the case of the *energy sinks* [30, 93, 94, 100], the posed problem is still linear. Equipping a

structure with electric or magnetic inclusions is synonym of introducing long-range interactions of a nonlinear nature, which influences the governing equation of motion. Besides, their contactless feature and hence, the lack of structural constrains, simplifies the practical generation of long-range forces. However, from a mathematical point of view, these force are rather complex to manipulate, due to the presence of a discontinuity in their domain, as it can be seen in Figure (3.4). Since these forces describe the link existing between two elements, equally whether they are charges or dipoles, the discontinuity represents the natural impossibility of the two elements to collide. This aspect justifies the choice of adopting other type of forces to characterize long-range interactions, physically analogous to Coulomb force and to the magnetic coupling, but mathematically more suitable. The family of power law forces is the one that better responds to these requirements, being a perfect compromise between the necessary physical equivalence and the mathematical application, and in this sense it does not sound unfamiliar, since also Tarasov in [51] and Eringen in [40] have underlined the remarkable properties of this type of forces.

3.3 Intrabody and interbody forces

Each type of interaction has its own region of applicability, defined by a typical interaction length and depending on the strength of the force; any object within that region is connected, whether it is matter of particles within the same body, in that case one could talk of *intra-body interactions*, or different bodies, named *inter-body interactions*, still they will communicate. The case of *inter-body interactions* can be particularly interesting if one considers that actions on one structure affects the others, generating wave propagation phenomena. This discloses the chance to realize an entire network of communicating systems and even of remote control. Practically, this can be realized by the mean of magnetic inclusions within the structure of an elastic support and the model is the one presented in Figure (3.6), analogous to those presented in Figure (3.1).

The presence of long-range interactions, additional to the conventional elastic ones,

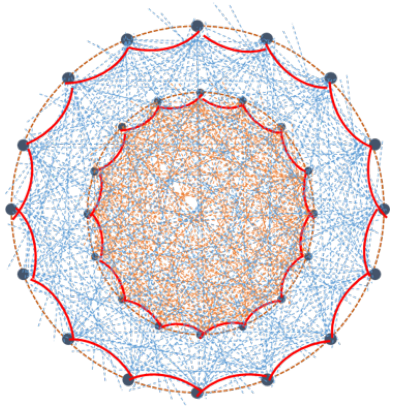

Figure 3.6. Interbody long-range interactions

produces a modification of the topology of a structure and hence, of its dynamic behaviour, defining a new paradigm in structural mechanics, traditionally associated

to conventional and short-range interactions.

Let us consider two nonadjacent particles interacting with each other, not necessarily belonging to the same medium, but surely at a distance smaller than the long-range force characteristic length. The initial configuration, assumed as reference, is such that the first particle is placed at x and the second at ξ. The mutual force is expressed by:

$$F\left(x+u(x,t),\xi+u(\xi,t)\right)=-f(|r|)r \tag{3.3}$$

where $r=x-\xi+u(x,t)-u(\xi,t)$ is the distance between the two particles and $u(x,t)$ is the displacement in the elastic medium, as shown in Figure (3.7).

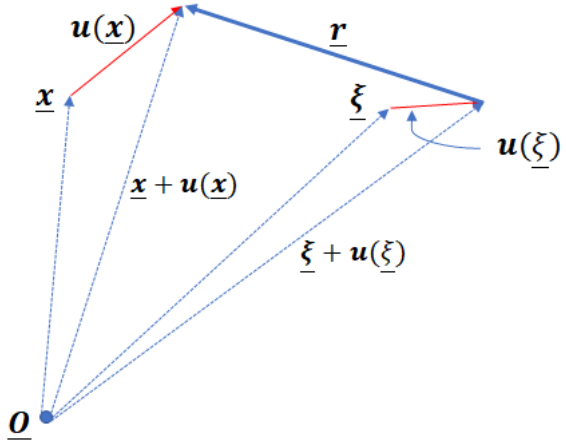

Figure 3.7. Definition of the vector r

The shape of the long-range forces must guarantee the legitimacy of the action-reaction principle, i.e. $F(r)=-F(-r)$. Moreover, they are modelled so to decay with the distance, $\lim_{|r|\to\infty} f(|r|)r=0$, as typical of several existing forces, namely magneto-static, Coulomb, gravitational and molecular bond.
When the long-range interaction involves more than two points, becoming a master-cluster or an all-to-all interaction, the contribution of the long-range forces is a summation extended to all the interacting couples, as shown in Figure 3.8. and the

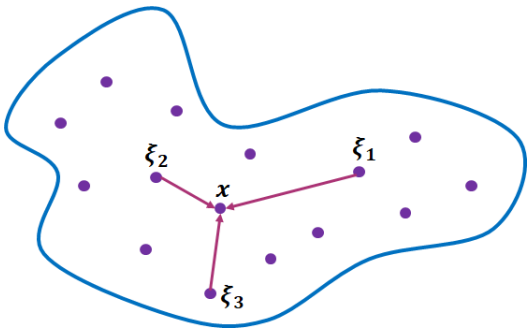

Figure 3.8. Discrete contribution of long-range forces

force assumes the form:

$$\boldsymbol{F}(\boldsymbol{x}) = f(|\boldsymbol{r}_{11}|)\boldsymbol{r}_{11} + f(|\boldsymbol{r}_{12}|)\boldsymbol{r}_{12} + f(|\boldsymbol{r}_{13}|)\boldsymbol{r}_{13} + \dots \tag{3.4}$$

where $\boldsymbol{r}_{ij}$ is the distance between the particle set at $\boldsymbol{x}$ and the particle set at $\boldsymbol{\xi}_j$. If the particle density within the medium is assumed semi-infinite, as shown in Figure 3.9, then the contribution of these forces turns into an integral term $\int_{\xi\in\mathbb{R}^3} f(|\boldsymbol{r}|)\boldsymbol{r}dV$. The integral represents the summation of the long-range interaction forces, exerted on the particle originally at $\boldsymbol{x}$, due to all the particles in the space, varying with $\boldsymbol{\xi}$ and overcomes the ordinary concept of the short-range interactions.
If long-range forces do not involve only points within the same medium, but are

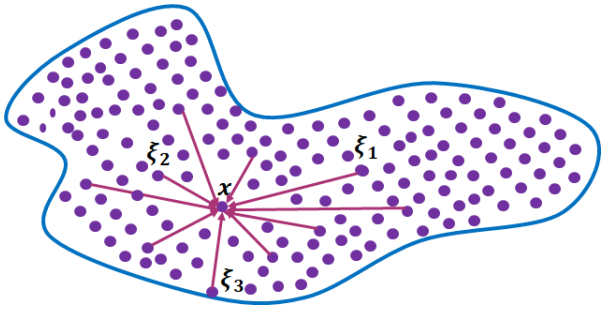

Figure 3.9. Integral contribution of long-range forces

powerful enough to extend the connection to multiple bodies, then the equation of motion would be completed with additional integral contributions, accounting both for *intra-body* and *inter-body* interactions. In that case, the equation of motion, generally expressed by equation (2.14), becomes:

$$\rho\, \boldsymbol{u}_{tt}(\boldsymbol{x},t) - \frac{E}{2(1+\nu)}\left[\nabla^2\boldsymbol{u}(\boldsymbol{x},t) + \frac{1}{1-2\nu}\nabla\left(\nabla\cdot\boldsymbol{u}(\boldsymbol{x},t)\right)\right] + \int_{\xi\in\mathbb{R}^3} f(|\boldsymbol{r}|)\boldsymbol{r}\, dV + \\ + \int_{\eta\in\mathbb{R}^3} f(|\boldsymbol{r}|)\boldsymbol{r}\, dV = 0 \tag{3.5}$$

where ξ is the coordinate associated to the *intra-body* forces, η is the coordinate associated to the *inter-body* forces, $\rho(x)$ is the mass density, $E(x)$ the Young's modulus, $\nu(x)$ the Poisson modulus and ∇ the nabla operator. From a mathematical point of view, these long-range forces introduce a nonlinear feature into the equation of motion, related to their integral nature.
The convention used for $f(|\boldsymbol{r}|)$ is such that $f(|\boldsymbol{r}|)$ is negative for repulsive forces and positive for attractive ones. To better understand this convention, let rewrite equation (3.3) as:

$$\boldsymbol{F}(\boldsymbol{r}) = -\boldsymbol{r}\,\mathrm{sign}\, f(|\boldsymbol{r}|) \tag{3.6}$$

Since the equation of motion is written considering the forces exerted on the particle at $\boldsymbol{x}$ due to the particle at $\boldsymbol{\xi}$, according to Figure (3.7), a repulsive force $\boldsymbol{F}(\boldsymbol{r})$ implies $f(|r|)$ to be opposite with respect to the vector $\boldsymbol{r}$, and vice versa for the attractive one.

For acoustic media with long-range interactions (the case of electrostatic approximation of low frequency plasma [105]), and considering only *intra-body* forces, the equation of motion can be simplified as $\square u(\boldsymbol{x},t) + \int_{\boldsymbol{\xi}\in\mathbb{R}^3} f(|\boldsymbol{r}|)\mathbf{r}\, dV = 0$. In general, analytic solutions are not possible. However, the linearization of the force $f(|\boldsymbol{r}|)\boldsymbol{r}$, with respect to $\boldsymbol{\varepsilon} = \boldsymbol{u}(\boldsymbol{x},t) - \boldsymbol{u}(\boldsymbol{\xi},t)$ and for small deformation, permits, together with some additional hypotheses introduced later, to investigate closed form solutions, providing important insights into the wave propagation properties.

3.4 A linearised model

The complexity of the posed problem requires some simplifications to ensure the achievement of analytical solutions, which are in general not possible. This section is focused on the linearization of the long-range force $\boldsymbol{F}(\boldsymbol{r})$ with respect to $\boldsymbol{\varepsilon} = \boldsymbol{u}(\boldsymbol{x},t) - \boldsymbol{u}(\boldsymbol{\xi},t)$ and for small deformations, with direct advantages regarding the investigation of the equation of motion.
The final expression of the considered force is derived, starting from its Taylor expansion up to the first order in terms of $\boldsymbol{\varepsilon}$. The force is presented in the form:

$$\boldsymbol{F}(\boldsymbol{r}) = f(|\boldsymbol{r}|)\boldsymbol{r} \tag{3.7}$$

where

$$\boldsymbol{r} = \boldsymbol{x} - \boldsymbol{\xi} + \boldsymbol{\varepsilon}$$

or for components:

$$f(|\boldsymbol{r}|)r_k$$

with

$$r_k = x_k - \xi_k + \varepsilon_k$$

The Taylor expansion of the force around ε_s leads to:

$$f(|\boldsymbol{r}|)\boldsymbol{r} = f(|\boldsymbol{x}-\boldsymbol{\xi}|)\,(\boldsymbol{x}-\boldsymbol{\xi}) + \frac{\partial}{\partial\boldsymbol{\varepsilon}}\left[f(|\boldsymbol{r}|)\boldsymbol{r}\right]\big|_{\boldsymbol{\varepsilon}=\mathbf{0}}\boldsymbol{\varepsilon} \tag{3.8}$$

namely:

$$f(|\boldsymbol{r}|)r_k = f(|\boldsymbol{x}-\boldsymbol{\xi}|)\,(x_k-\xi_k) + \sum_s \frac{\partial}{\partial\varepsilon_s}\left[f(|\boldsymbol{r}|)r_k\right]\big|_{\varepsilon=0}\varepsilon_s \tag{3.9}$$

$$f(|\boldsymbol{r}|)r_k = f(|\boldsymbol{x}-\boldsymbol{\xi}|)\,(x_k-\xi_k) + \sum_s \left[\left.\frac{\partial f}{\partial\varepsilon_s}\right|_{\varepsilon=0}(x_k-\xi_k)\,\varepsilon_s + f|_{\varepsilon=0}\left.\frac{\partial r_k}{\partial\varepsilon_s}\right|_{\varepsilon=0}\varepsilon_s\right] \tag{3.10}$$

$$f(|\boldsymbol{r}|)r_k = f(|\boldsymbol{x}-\boldsymbol{\xi}|)\,(x_k-\xi_k) + \sum_s \left[\left.\frac{\partial f}{\partial|\boldsymbol{r}|}\right|_{\varepsilon=0}\left.\frac{\partial|\boldsymbol{r}|}{\partial\varepsilon_s}\right|_{\varepsilon=0}(x_k-\xi_k)\,\varepsilon_s + f|_{\varepsilon=0}\left.\frac{\partial r_k}{\partial\varepsilon_s}\right|_{\varepsilon=0}\varepsilon_s\right] \tag{3.11}$$

Examining the terms in the square brackets aside, one obtains:

$$\left.\frac{\partial|\boldsymbol{r}|}{\partial\varepsilon_s}\right|_{\varepsilon=0} = \left.\frac{\partial}{\partial\varepsilon_s}\left[\sum_i (x_i-\xi_i+\varepsilon_i)^2\right]^{\frac{1}{2}}\right|_{\varepsilon=0} = \left.\frac{1}{2}\frac{2\,(x_s-\xi_s+\varepsilon_s)}{|\boldsymbol{x}-\boldsymbol{\xi}+\boldsymbol{\varepsilon}|}\right|_{\varepsilon=0} = \frac{x_s-\xi_s}{|\boldsymbol{x}-\boldsymbol{\xi}|} \tag{3.12}$$

$$\left.\frac{\partial r_k}{\partial \varepsilon_s}\right|_{\varepsilon=0} = \left.\frac{\partial}{\partial \varepsilon_s}\left(x_k - \xi_k + \varepsilon_k\right)\right|_{\varepsilon=0} = \delta_{sk} \tag{3.13}$$

Thus, equation (3.11) becomes:

$$f(|\boldsymbol{r}|)r_k = f(|\boldsymbol{x}-\boldsymbol{\xi}|)\left(x_k - \xi_k\right) + \sum_s \left[\left.\frac{\partial f}{\partial |\boldsymbol{r}|}\right|_{\varepsilon=0} \frac{(x_s - \xi_s)}{|\boldsymbol{x}-\boldsymbol{\xi}|}\left(x_k - \xi_k\right)\varepsilon_s + f|_{\varepsilon=0}\,\delta_{sk}\varepsilon_s\right] \tag{3.14}$$

$$f(|\boldsymbol{r}|)r_k = f(|\boldsymbol{x}-\boldsymbol{\xi}|)\left(x_k - \xi_k\right) + \sum_s \left[\left.\frac{\partial f}{\partial |\boldsymbol{r}|}\right|_{\varepsilon=0} \frac{(x_s - \xi_s)\varepsilon_s}{|\boldsymbol{x}-\boldsymbol{\xi}|}\left(x_k - \xi_k\right) + f|_{\varepsilon=0}\,\varepsilon_k\right] \tag{3.15}$$

or in vectorial form:

$$f(|\boldsymbol{r}|)\boldsymbol{r} = f(|\boldsymbol{x}-\boldsymbol{\xi}|)\left(\boldsymbol{x}-\boldsymbol{\xi}\right) + \left[\left.\frac{\partial f}{\partial |\boldsymbol{r}|}\right|_{\boldsymbol{\varepsilon}=\boldsymbol{0}} \frac{(\boldsymbol{x}-\boldsymbol{\xi})\cdot\boldsymbol{\varepsilon}}{|\boldsymbol{x}-\boldsymbol{\xi}|}\left(\boldsymbol{x}-\boldsymbol{\xi}\right) + f|_{\boldsymbol{\varepsilon}=\boldsymbol{0}}\,\boldsymbol{\varepsilon}\right] \tag{3.16}$$

$$f(|\boldsymbol{r}|)\boldsymbol{r} \sim \left[f(|\boldsymbol{x}-\boldsymbol{\xi}|) + \left.\frac{\partial f}{\partial |\boldsymbol{r}|}\right|_{\boldsymbol{\varepsilon}=\boldsymbol{0}} \frac{(\boldsymbol{x}-\boldsymbol{\xi})\cdot\boldsymbol{\varepsilon}}{|\boldsymbol{x}-\boldsymbol{\xi}|}\right]\left(\boldsymbol{x}-\boldsymbol{\xi}\right) + f_0\boldsymbol{\varepsilon} \tag{3.17}$$

Hence,

$$f(|\boldsymbol{r}|)\boldsymbol{r} \sim \left[f_0 + \left.\frac{\partial f}{\partial |\boldsymbol{r}|}\right|_{\boldsymbol{\varepsilon}=\boldsymbol{0}} \frac{(\boldsymbol{x}-\boldsymbol{\xi})\cdot\boldsymbol{\varepsilon}}{|\boldsymbol{x}-\boldsymbol{\xi}|}\right]\left(\boldsymbol{x}-\boldsymbol{\xi}\right) + f_0\boldsymbol{\varepsilon} \tag{3.18}$$

The introduction of an appropriate choice of a second order tensor $\boldsymbol{h}_0$ allows the second and the third term to be rewritten as follows:

$$\left.\frac{\partial f}{\partial |\boldsymbol{r}|}\right|_{\boldsymbol{\varepsilon}=\boldsymbol{0}} \frac{(\boldsymbol{x}-\boldsymbol{\xi})\cdot\boldsymbol{\varepsilon}}{|\boldsymbol{x}-\boldsymbol{\xi}|}\left(\boldsymbol{x}-\boldsymbol{\xi}\right) + f_0\boldsymbol{\varepsilon} = \boldsymbol{h}_0\boldsymbol{\varepsilon} + f_0\boldsymbol{\varepsilon} \tag{3.19}$$

The component form of the first term is:

$$\sum_k \left.\frac{\partial f}{\partial |\boldsymbol{r}|}\right|_{\boldsymbol{\varepsilon}=\boldsymbol{0}} \frac{(x_k - \xi_k)\varepsilon_k}{|\boldsymbol{x}-\boldsymbol{\xi}|}\left(x_s - \xi_s\right) \tag{3.20}$$

therefore,

$$\sum_k \left.\frac{\partial f}{\partial |\boldsymbol{r}|}\right|_{\boldsymbol{\varepsilon}=\boldsymbol{0}} \frac{\left(x_k - \xi_k\right)\left(x_s - \xi_s\right)}{|\boldsymbol{x}-\boldsymbol{\xi}|}\varepsilon_k \tag{3.21}$$

The second order tensor $\boldsymbol{h}_0$ is, then, given by:

$$h_{sk}\left(\boldsymbol{x}-\boldsymbol{\xi}\right) = \left.\frac{\partial f}{\partial |\boldsymbol{r}|}\right|_{\boldsymbol{\varepsilon}=\boldsymbol{0}} \frac{\left(x_k - \xi_k\right)\left(x_s - \xi_s\right)}{|\boldsymbol{x}-\boldsymbol{\xi}|} \tag{3.22}$$

or in tensorial form:

$$\boldsymbol{h}_0 = \left.\frac{\partial f}{\partial |\boldsymbol{r}|}\right|_{\boldsymbol{\varepsilon}=\boldsymbol{0}} \frac{(\boldsymbol{x}-\boldsymbol{\xi})\otimes(\boldsymbol{x}-\boldsymbol{\xi})}{|\boldsymbol{x}-\boldsymbol{\xi}|} \tag{3.23}$$

where the symbol $\otimes$ represents the tensor product operator.
Eventually, equation (3.17) can be written as:

$$f(|\boldsymbol{r}|)\boldsymbol{r} \sim \left(\boldsymbol{x}-\boldsymbol{\xi}\right) f_0 + \boldsymbol{h}_0\boldsymbol{\varepsilon} + f_0\boldsymbol{\varepsilon} \tag{3.24}$$

in which the subscript indicates quantities evaluated at $\boldsymbol{\varepsilon} = \boldsymbol{0}$. The force is composed by three terms: the first is a static force, the other two are instead dynamic forces,

displacement dependent. Namely, the second order tensor $\boldsymbol{h}_0$ depends on the gradient of the force with respect to the distance, while the third is due to the static pre-stress.
The linearised integral term of the equation of motion (3.5) is:

$$\int_{\boldsymbol{\xi}\in\mathbb{R}^3} \left[(\boldsymbol{x}-\boldsymbol{\xi})\, f_0 + \boldsymbol{h}_0\boldsymbol{\varepsilon} + f_0\boldsymbol{\varepsilon}\right] dV \tag{3.25}$$

and the final version of Navier-Cauchy integral-differential equation for a three dimensional, continuous, unbounded media becomes:

$$\rho\boldsymbol{w}_{tt} - \frac{E}{2(1+\nu)}\left[\nabla^2\boldsymbol{w} + \frac{1}{1-2\nu}\nabla\left(\nabla\cdot\boldsymbol{w}\right)\right] + \bar{\boldsymbol{h}_0}\cdot\boldsymbol{w} - [\boldsymbol{h}_0 * \boldsymbol{w}] + \bar{f_0}\boldsymbol{w} - [f_0 * \boldsymbol{w}] = 0 \tag{3.26}$$

This is a linear integral-differential equation with space-dependent coefficients which, based on the Eringen nonlocal elasticity theory, includes at this stage only the *intra-body* contribution (a more complete treating, which includes *inter-body* forces as well, is presented in chapter 5, regarding the *twin system*). Equation (3.26), in which $*$ indicates the convolution operation and the symbol $\bar{\cdot}$ average over $\mathbb{R}^3$, is written for the dynamic component $\boldsymbol{w}(\boldsymbol{x},t)$ of the displacement only. In general, one should consider the whole displacement $\boldsymbol{u}(\boldsymbol{x},t) = \boldsymbol{v}(\boldsymbol{x}) + \boldsymbol{w}(\boldsymbol{x},t)$, without separating the two components. However, in a context in which the focus is the wave propagation, the discussion is not about $\boldsymbol{v}(\boldsymbol{x})$. Moreover, $\boldsymbol{v}(\boldsymbol{x})$ vanishes for those forces that respect:

$$\int_{\boldsymbol{\xi}\in\mathbb{R}^3} (\boldsymbol{x}-\boldsymbol{\xi}) f_0\, dV = 0$$

and only $\boldsymbol{w}(\boldsymbol{x},t)$ remains.
The presented linearization is valid only under specific conditions and, in particular, for a one-dimensional system the appropriate version of the equation of motion (3.5) is admissible as long as $|\varepsilon| \ll |x-\xi|$. This means $\dfrac{|\varepsilon|}{|x-\xi|} = \dfrac{|w(x,t)-w(\xi,t)|}{|x-\xi|} \ll 1$, which implies that the strain must be small, at least of order 10^{-1}. To express this condition in terms of characteristic interaction length, let assume the displacement of a travelling wave perturbation as $w(x,t) = w_0 e^{j(kx-\omega t)}$. The strain is given by $\dfrac{\partial w}{\partial x} = jkw_0 e^{j(kx-\omega t)}$, and, for the linearization to be valid, it must be in modulus much smaller than unity, thus $|w_0 k| \ll 1$. Finally, for $K = \beta k$ the nondimensional wavenumber, where β is the typical long-range interaction length, the last relation becomes $\left|\dfrac{w_0 K}{\beta}\right| \ll 1$ and $K \ll \dfrac{\beta}{w_0}$.
This means that, once the region of investigation is chosen in terms of K, the amplitude of vibration w_0 must be compared with the typical interaction length β for the linearization to be guaranteed.
As final consideration, it must be noticed that equation (3.26) can provide analytical solutions for particular choices of the function $f(|\boldsymbol{r}|)$.

3.5 Final remarks

Long-range interactions crash the concept of conventional dynamics and go beyond a local, short range connectivity, where the communication pattern exists only among close neighbour particles. Regardless their nature, long-range connections introduce nonlinear properties in the system, whose dynamics is unavoidably influenced. It is shown how the presence of a convolution term in the displacement field equation, according to Eringen's theory, is representative of their integral nature and the mathematical model is hence ruled by integral-differential equations. The present chapter reports a wide spectrum analysis of the long-range interactions in terms of their nature, of their physical interpretation, of their range of applicability and of the complexity they inevitably introduce both in the mathematical model and in the dynamic response.

Chapter 4

Analytical solutions for the 1D linear problem

The introduced mathematical model is based on Navier-Cauchy equations, characterised by integral-differential terms and nonlinear properties. To better inspect the effects of the new long-range interactions on the propagation behaviour, the simpler one-dimensional case will be examined.
In the following section, remarkable kernels for the long-range interactions, i.e. single contribution of long-range forces and a Gaussian-like and Laplace-like forces, are examined, since they disclose analytical solutions to the equation (3.26).

4.1 Linearised integral-differential equation for long-range metamaterials

Equation (3.26) defines the dynamic behaviour of an elastic metamaterials in which long-range interactions change the topology of the connections and, hence, the dynamic response of the system. However, given the complexity of the problem, the investigation of the propagating properties requires some simplifications. For this reason, the one-dimensional version of equation (3.26) is here considered.
The aim is to obtain a shape of the equation (3.26) consistent with Eringen formulation for nonlocal elasticity in 1D [41], even though Eringen assumption is based on the constitutive laws and what it is sought here is a relation with the interaction forces instead:

$$\rho\frac{\partial^2 w}{\partial t^2} - E\frac{\partial^2 w}{\partial x^2} - F(x) * \varepsilon_x = 0 \tag{4.1}$$

where ε_x is the strain along the x axis. This can be achieved through special kernels of the function $F(x)$, such that:

$$F(x) * \varepsilon_x = F(x) * \frac{\partial w(x)}{\partial x} = F(x) * w'_x = F'(x) * w_x = \frac{\partial F(x)}{\partial x} * w_x = g(x) * w(x) \tag{4.2}$$

through which the equation of motion takes the form:

$$\rho\frac{\partial^2 w}{\partial t^2} - E\frac{\partial^2 w}{\partial x^2} - g(x) * w(x) = 0 \tag{4.3}$$

The advantage of such formulation stands in the associated dispersion relationship. Indeed, assuming

$$w(x,t) = \iint_{-\infty}^{+\infty} W(k,\omega) e^{j(kx-\omega t)} dk\, d\omega \tag{4.4}$$

or taking the Fourier transform $\mathcal{F}\{\cdot\}$ of (4.3) with respect to x and t, the resulting dispersion relationship is:

$$\rho\omega^2 - Ek^2 + G(k) = 0 \tag{4.5}$$

where $G(k) = \mathcal{F}\{g(x)\}$. It is apparent that the analysis of the propagating characteristics depends on the shape of the function $G(k)$ and an appropriate choice of the function $F(x)$ would unveils analytical solutions.
The one-dimensional version of the Navier-Cauchy equation of motion (3.26) is:

$$\rho\frac{\partial^2 w}{\partial t^2} - E\frac{\partial^2 w}{\partial x^2} + \int_{-\infty}^{+\infty} F\left[x, \xi, w\left(x,t\right), w\left(\xi,t\right)\right] d\xi = 0 \tag{4.6}$$

or in convolution terms:

$$\rho\frac{\partial^2 w}{\partial t^2} - E\frac{\partial^2 w}{\partial x^2} + (h_0 * 1)\cdot w - [h_0 * (w)] + (f_0 * 1)w - [f_0 * (w)] = 0 \tag{4.7}$$

Since the terms $h_0 * 1$ and $f_0 * 1$ can be interpreted as averages of the quantities h_0 and f_0 over $\mathbb{R}^3$, i.e. $\bar{h}_0$ and $\bar{f}_0$, respectively, equation (4.7) can be rewritten as:

$$\rho\frac{\partial^2 w}{\partial t^2} - E\frac{\partial^2 w}{\partial x^2} + \bar{h}_0 \cdot w - h_0 * (w) + \bar{f}_0 w - f_0 * (w) = 0 \tag{4.8}$$

The presented equation does not produce analytical solutions. For this reason, some peculiar cases of long-range interactions are analysed and a more thorough investigation is carried on for Gauss-like and Laplace-like forces, eventually chosen to model the long-range interactions for their several advantages.

4.2 Special kernel for the long-range interactions

For special choices of the function $f(|\boldsymbol{r}|)\boldsymbol{r}$, equation (3.26) can exhibit analytical solutions. The advantage of a type of interaction able to provide analytical solutions of the equation of motion lies in the chance of a thorough investigation of the propagating behaviour, disclosing the main properties responsible of the modifications in the dynamic response.
In this section it is shown the existence of different families of long-range interactions for which closed form analytical solutions are possible. The long-range *prototypes* here discussed can be divided mainly in two groups:

- single distribution of long-range interactions: springs connecting two material points;
- continuous long-range interactions: the remarkable case of a Guass-like and Laplace-like forces and their variants.

4.2.1 Single distribution of long-range interactions

Discrete long-range interactions are probably elemental examples, but they are a useful tool to examine common properties of long-range interactions. Here, two cases are examined: the case of a single spring connecting two material elements and the case of two symmetric springs.
Let us analyse a single spring first, shown in Figure 4.1.
The equation of motion related to this system is:

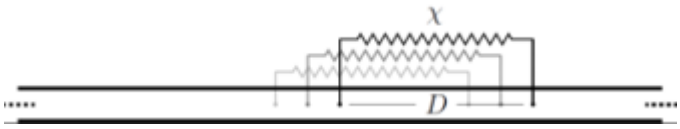

Figure 4.1. Long-range as a single spring

$$EA\frac{\partial^2 w(x,t)}{\partial x^2} - \rho A\frac{\partial^2 w(x,t)}{\partial t^2} + \chi\left[w(x) - w(x-D)\right] = 0 \tag{4.9}$$

Neglecting the effect of short-range interactions, if the displacement is assumed to be in the form $w(x,t) = w_0 e^{j(kx-\omega t)}$, for a complex wavenumber such that $k = k_R + jk_I$, then (see Appendix A for the complete calculations) the resulting dispersion relationship is:

$$\rho A\omega^2 - \chi + \chi\left[\cos k_R D - j\sin k_R D\right] e^{k_I D} = 0 \tag{4.10}$$

Dividing real and imaginary part of the equation, the following system is obtained:

$$\begin{cases} \rho A\omega^2 - \chi + \chi\cos k_R D e^{k_I D} = 0 \\ -\chi j \sin k_R D e^{k_I D} = 0 \end{cases} \tag{4.11}$$

This implies the conditions on the wavenumbers are:

$$\begin{cases} k_R^{(n)} = \dfrac{\pi n}{D} \\ k_I^{(n)} = \dfrac{1}{D}\ln\dfrac{1-\frac{\omega^2}{\omega_n^2}}{(-1)^n} \end{cases} \tag{4.12}$$

where $\omega_n^2 = \dfrac{\rho A}{D}$ is the natural frequency of the single oscillator. Analysing the solution as $k = k(\omega)$, the conditions on the wavenumber unveil the existence of an infinite set of wavenumbers for any given value of the frequency ω.
The case of a double spring, reported in Figure 4.2, can be straightforwardly obtained by following the same approach as for the single spring.
For such a system, the equation of motion is:

$$EA\frac{\partial^2 w(x,t)}{\partial x^2} - \rho A\frac{\partial^2 w(x,t)}{\partial t^2} + \chi\left[w(x) - w(x-D)\right] + \chi\left[w(x+D) - w(x)\right] = 0 \tag{4.13}$$

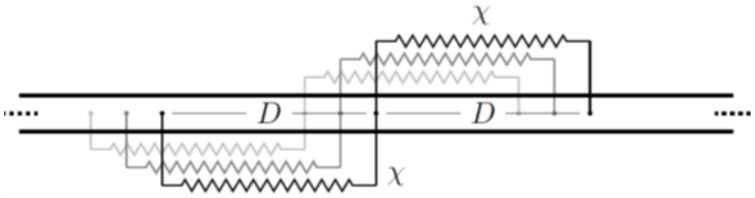

Figure 4.2. Long-range as a double spring

Applying the same procedure, hence neglecting the short-range effect, assuming the displacement once again of the form $w(x,t) = w_0 e^{j(kx-\omega t)}$ and for complex wavenumber $k = k_R + jk_I$, the dispersion relationship becomes:

$$\rho A\omega^2 + \chi\left[-2\cos k_R D \sinh k_I D + j2\sin k_R D \cosh k_I D\right] = 0 \tag{4.14}$$

Separation of real and imaginary part of the dispersion relationship leads to:

$$\begin{cases} \rho A\omega^2 - 2\chi \cos k_R D \sinh k_I D = 0 \\ \sin k_R D \cosh k_I D = 0 \end{cases} \tag{4.15}$$

The conditions on the wavenumber, trivial to find, are:

$$\begin{cases} k_R^{(n)} = \dfrac{\pi n}{D} \\ k_I^{(n)} = \dfrac{1}{D}\,\text{arcsinh}\,\dfrac{\rho A\omega^2}{2\chi}\dfrac{1}{(-1)^n} \end{cases} \tag{4.16}$$

As for the single spring, even in this case the existence of an infinite number of values of the wavenumber for any single frequency is demonstrated.

4.2.2 Continuous long-range interactions

To better understand the physics of waves behind (4.8), a Gaussian-like force and a Laplace-like force are considered, as they unveil some important propagation characteristics related to long-range interaction. These forces present three advantages: (i) they guarantee the action-reaction principle holds, given their antisymmetric behaviour with respect to their dependence on the distance r, (ii) they vanish for large x, a typical property of some long-range forces met in physics and (iii) they admit an analytical known Fourier transform $G(k)$. Besides, for power-like forces the average terms $\bar{h}_0$ and $\bar{f}_0$ vanish when integrated over the domain $\mathbb{R}^3$. This implies a strong simplification of the equation of motion, which becomes suitable for an analytical investigation.

4.2.2.1 Gauss-like force

The considered Gaussian-like form is:

$$F(r) = \mu r e^{-\left(\frac{r}{\beta}\right)^2} \tag{4.17}$$

where μ controls the intensity of the force, β is the characteristic interaction length and $r = x - \xi + w(x,t) - w(\xi,t)$. While β is always positive, the sign of μ rules the attractive and repulsive property of the force, and according to the convention stipulated in section 3.3, positive μ represents attractive forces and negative μ indicates repulsive ones. This force, whose shape is according to equation (3.7), satisfies two physical requirements: $F(r) = -F(-r)$ and $\lim_{r\to\infty} F(r) = 0$. The trend of the Gauss-like force is shown in Figure 4.3.

To proceed with the analytical study of the dispersion relationship, it is necessary

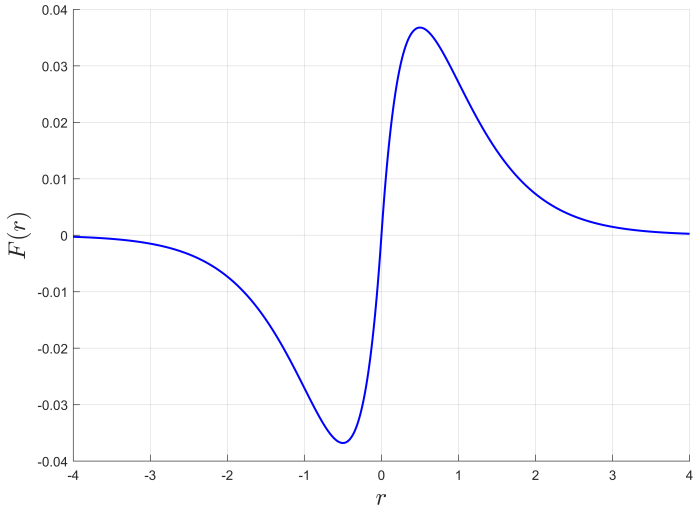

Figure 4.3. Gauss-like force

to linearise the force about $\varepsilon = w(x) - w(\xi) = 0$, as it has been done for the general case:

$$\begin{aligned} F(x,\xi) \approx \mu(x-\xi)e^{-\left(\frac{x-\xi}{\beta}\right)^2} + \mu\left[1-2\left(\frac{x-\xi}{\beta}\right)^2\right]e^{-\left(\frac{x-\xi}{\beta}\right)^2} w(x) \\ - \mu\left[1-2\left(\frac{x-\xi}{\beta}\right)^2\right]e^{-\left(\frac{x-\xi}{\beta}\right)^2} w(\xi) \end{aligned} \tag{4.18}$$

The first two terms of (4.18), shown in Figure 4.4, vanish when integrated. The third one, according to the used formulation, can be rewritten as:

$$-\mu\left[1-2\left(\frac{x-\xi}{\beta}\right)^2\right]e^{-\left(\frac{x-\xi}{\beta}\right)^2} w(\xi) = [f_0 + h_0](x-\xi)\,w(\xi) = g(x-\xi)\,w(\xi) \tag{4.19}$$

in this way, equation (4.6) becomes:

$$\rho\frac{\partial^2 w}{\partial t^2} - E\frac{\partial^2 w}{\partial x^2} - \mu\int_{-\infty}^{+\infty}\left(1-\frac{2}{\beta^2}\xi^2\right)e^{-\left(\frac{\xi}{\beta}\right)^2} w(x-\xi)d\xi = 0 \tag{4.20}$$

or in convolution notation:

$$\rho\frac{\partial^2 w}{\partial t^2} - E\frac{\partial^2 w}{\partial x^2} - g(x) * w(x) = 0 \tag{4.21}$$

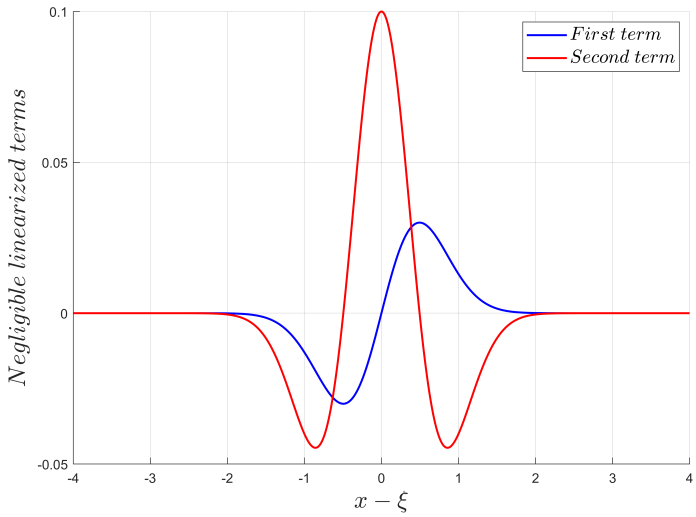

Figure 4.4. Vanishing terms of the approximated linear force

where $g(x) = \left.\dfrac{\partial F(r)}{\partial r}\right|_{r=x}$.

4.2.2.2 Laplace-like force

In this case, F is based on the Laplace distribution:

$$F(r) = \mu r e^{-\frac{|r|}{\beta}} \tag{4.22}$$

shown in Figure 4.5.
For this force, as for the Gauss-like distribution, $F(r) = -F(-r)$ and $\lim_{r\to\infty} F(r) = 0$ hold.
The linearised force is:

$$\begin{aligned} F(x,\xi) \approx \mu(x-\xi)e^{-\frac{|x-\xi|}{\beta}} &+ \mu\left[1 - \frac{|x-\xi|}{\beta}\right] e^{-\frac{|x-\xi|}{\beta}} w(x) \\ &- \mu\left[1 - \frac{|x-\xi|}{\beta}\right] e^{-\frac{|x-\xi|}{\beta}} w(\xi) \end{aligned} \tag{4.23}$$

Figure 4.6 shows as, also in this case, the first two terms of the linearization vanish when integrated over the domain.
The equation of motion becomes:

$$\rho\frac{\partial^2 w}{\partial t^2} - E\frac{\partial^2 w}{\partial x^2} - \mu\int_{-\infty}^{+\infty}\left(1 - \frac{|\xi|}{\beta}\right) e^{-\frac{|\xi|}{\beta}} w(x-\xi)d\xi = 0 \tag{4.24}$$

which can be written in a convolution form analogue to equation (4.21).

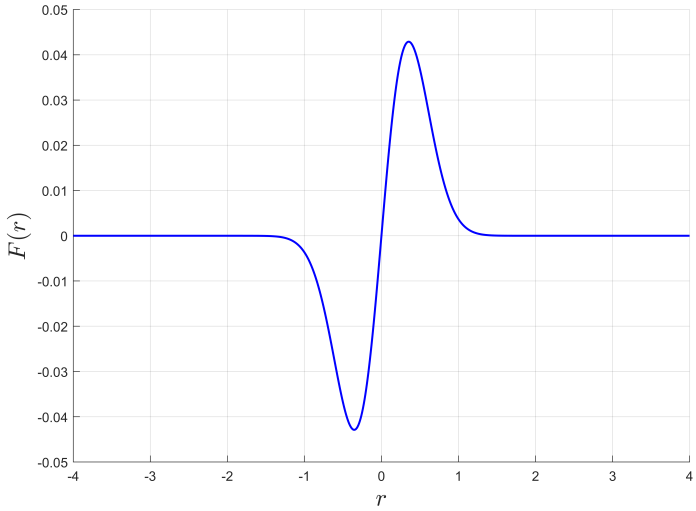

Figure 4.5. Laplace-like force

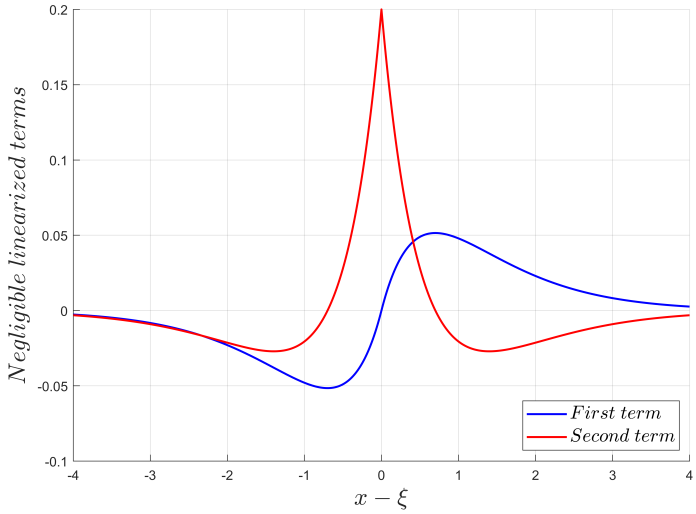

Figure 4.6. Vanishing terms of the approximated linear force

4.2.2.3 Variants of power-like forces

Since the problem is treated as linear, it is clear that also appropriate variants of the mentioned power-like forces might produce the same relevant results. As "appropriate variants" one could refer to multiple peaks power-like forces, as shown in Figure 4.7, which provides an example for a double-peak Gauss-like force, but analogous considerations hold for the Laplace distribution as well.

A continuous equation of motion implies that the relation imposed by it is valid at any instant for any portion of the structure. Considering for instance the Gauss-like force, it means that any particle is source of this interaction. Therefore, the physical

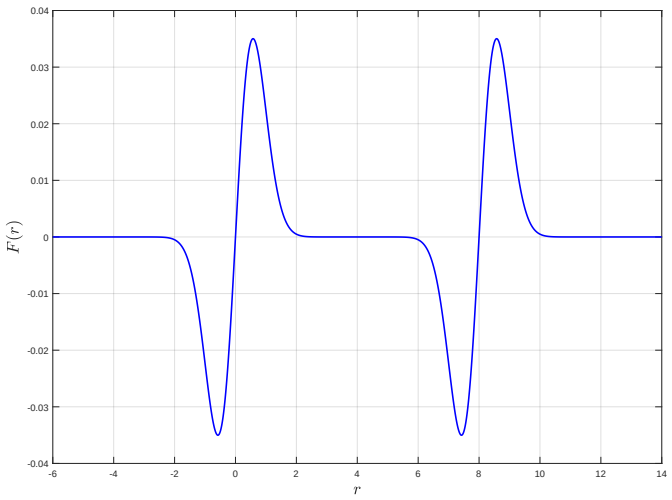

Figure 4.7. Double peak Gauss-like force

meaning of multiple-peak type of force should not be confused, in the sense that each peak is not associated to each particle, but it is only a way to further extend the range of interaction; each multiple peak is originated by any elementary component of the structure.
The expression of the double-peak Gauss-like force is:

$$F(r) = \mu r e^{-\left(\frac{r}{\beta}\right)^2} + \mu\,(r-a)\,e^{-\left(\frac{(r-a)}{\beta}\right)^2} \tag{4.25}$$

It is trivial to obtain the equation of motion, which takes the form:

$$\begin{aligned}\rho\frac{\partial^2 w}{\partial t^2} - E\frac{\partial^2 w}{\partial x^2} - \mu\int_{-\infty}^{+\infty}\left(1-\frac{2}{\beta^2}\xi^2\right)e^{-\left(\frac{\xi}{\beta}\right)^2} w(x-\xi)d\xi - \\ \mu\int_{-\infty}^{+\infty}\left(1-\frac{2}{\beta^2}(\xi-a)^2\right)e^{-\left(\frac{\xi-a}{\beta}\right)^2} w(x-\xi)d\xi = 0\end{aligned} \tag{4.26}$$

and eventually becomes:

$$\rho\frac{\partial^2 w}{\partial t^2} - E\frac{\partial^2 w}{\partial x^2} - g(x) * w(x) - g(x-a) * w(x) = 0 \tag{4.27}$$

where the second convolution term has the function to empower the contribution of the long-range interactions. The linearity of the problem allows to extend the number of terms till the limit of an infinite series, with no consequences on the resolution of the problem, which remains totally analogous to the simpler case of a single peak force. Moreover, it should be noticed that the shape of the function, through the parameters β and μ, not necessarily has to be identical between the two convolution terms, but it can be adequately adjusted.
This completes the analysis of the families of kernels suitable for the present investigation.

4.3 Dispersion equations and wave propagation problem

Once the equation of motion is obtained (equation (4.21)), through the Fourier Transform or imposing a specific shape of the displacement (equation (4.4)), the dispersion relationship is trivial to calculate for a given $G(k)$ and it is presented in a form as in equation (4.5). A dispersion relationship, by definition, is a law that links frequencies and wavenumbers, and it can be analysed both considering the wavenumber k as a function of the frequency ω or vice versa as $\omega = \omega(k)$.
For the Gauss-like force, $G(k)$ assumes the form:

$$G(k) = \frac{\mu\beta^3}{2\sqrt{2}} k^2 e^{-\frac{\beta^2 k^2}{4}} \tag{4.28}$$

and its associated relationship is (see Appendix B for the mathematical procedure):

$$\Omega^2 + K^2 \left(\chi e^{-\frac{K^2}{4}} - 1 \right) = 0 \tag{4.29}$$

where $\Omega = \sqrt{\frac{\rho}{E}}\beta\omega$, $K = \beta k$ and $\chi = \frac{\mu\beta^3}{2\sqrt{2}E}$ are nondimensional parameters. χ can be rewritten as $\chi = \frac{E^*}{E}$ and hence interpreted as ratio between the elastic modulus provided by the long-range forces and the conventional Young's modulus and, in these terms, it provides a measure of the intensity of the long-range interactions. Moreover, χ has the same role of μ, since whether the force is attractive or repulsive is ruled by the sign of χ; indeed, attraction occurs for $\chi > 0$ and repulsion $\chi < 0$.
In the same way, for the Laplace-like force

$$G(k) = \frac{2\sqrt{\frac{2}{\pi}}\beta^3 k^2 \mu}{\left(1 + \beta^2 k^2\right)^2} \tag{4.30}$$

and the associated dispersion relationship is:

$$\Omega^2 + K^2 \left(\frac{8\chi}{\sqrt{\pi}\left(K^2 + 1\right)^2} - 1 \right) = 0 \tag{4.31}$$

The analysis of the wavenumer as function of the frequency $k = k(\omega)$ returns all its possible values, in general complex and the equation admits a set of numerable solutions, which can be finite or infinite, depending on the nature of $G(k)$.
Due to the trascendent form of the dispersion relationships (equations (4.12), (4.16), (4.29) and (4.31)), to each value of the frequency, the associated wavenumber assumes an infinite set of numerable wavenumbers. If one interprets the roots as a wave (propagating or evanescent), this implies that, for each excitation frequency, the disperison relationship predicts a waveguide response composed by the superposition of a set of infinite wavenumbers. Hence, even a single excitation frequency produces a complex wave train that is dispersive. In other words, while in a standard waveguide (closest neighbour interaction) we expect a sine-shaped waveform translating towards the x axis, when a single-frequency is acting, in the present

long-range system, we expect to see that a single-frequency excitation generates a superposition of different sine-shaped waveforms, translating at different phase speeds. In this way, each wavenumber defines a *propagating shape*, physically different with respect to the classical modes arising in finite size systems. Therefore, a long-range system produces, at each single-frequency, a response that is the superposition of an infinite number of *propagation shapes*.
This is unusual for standard one-dimensional propagating phenomena, where for partial differential equations, in general, one obtains a polynomial form of the dispersion relationship, which admits at most a number of different roots equal to the degree of the polynomial; in particular, the higher the derivation order, the larger is the set of numerable values the wavenumber can assume for each frequency. Moreover, the case of an infinite set of wavenumbers commonly refers to finite-size systems, since complex wavenumers are connected to localized and vanishing phenomena and to the boundary conditions.
The outlined physical phenomenon is new and it has an analogy only in two- or three-dimensional systems, which are associated to higher-order derivatives, but not yet found in structures modelled by one-dimensional equations. A system has a dimension which can assume a different meaning whether it is discussed by a mathematical or a physical point of view. A mathematically multi-dimensional system is a system that, even tough physically one-dimensional, has multi-variable equations of motion. An example is the case of strip-like structures that are properly two-dimensional systems, with a finite length along one axis and an infinite length along the other. Precisely, along the finite size axis, transverse modes take place, while along the infinite size direction, a *propagating shape* travels, related to the excited transverse steady mode. Examples of this behaviour are met in optical/electromagnetic waveguides and are known as TE, TM and TEM (transverse electromagnetic modes, or purely electric or magnetic modes [106]), or in mechanical strip-like bending plates [107–109], or in laser theory, but needing 2D or 3D systems . A further example is the Timoshenko beam theory [110], which is physically one-dimensional, but mathematically multi-dimensional, since wave propagation involves not only the longitudinal direction. This aspect emerges from the equation of motion for a linear, elastic, isotropic, homogeneous beam with a constant cross-section:

$$EI\frac{\partial^4 w(x,t)}{\partial x^4} + m\frac{\partial^2 w(x,t)}{\partial t^2} - \left(J + \frac{EIm}{kAG}\right)\frac{\partial^4 w(x,t)}{\partial x^2 \partial t^2} + \frac{mJ}{kAG}\frac{\partial^4 w(x,t)}{\partial t^4} = q(x,t) + \frac{J}{kAG}\frac{\partial^2 q(x,t)}{\partial t^2} - \frac{EI}{kAG}\frac{\partial^2 q(x,t)}{\partial x^2} \quad (4.32)$$

where A is the cross-section area, G is the shear modulus, I is the second moment of area, k is the Timoshenko shear coefficient, q is the external load, $J = \rho I$, $m = \rho A$. The associated dispersion relationship is given by:

$$c_L^2 c_S^2 k_G \left(1 - j\omega\mu\right)^2 k^4 - \left(c_L + k_G c_S^2\right)\left(1 - j\omega\mu\right) k^2\omega^2 - \omega^2 \frac{\left(k_G c_S^2\right)}{r_G}\left(1 - j\omega\mu\right) + \omega^4 = 0 \quad (4.33)$$

where c_L is the longitudinal wave velocity, c_S the shear wave velocity, r_G is the radius of gyration $r_G = \sqrt{\frac{I}{A}}$, k_G the Timoshenko shear coefficient. This formulation

is based on two independent parameters: $\Omega = \dfrac{\omega r_G}{c_S}$ and $R = \dfrac{G}{E} = \dfrac{c_S^2}{c_L^2}$.
A last representative example is the double curvature shells, mathematically and physically multi-dimensional. The equation of equilibrium for a shell element is provided by [111]:

$$K\nabla^4 w = p_z + E\delta\left[k_x\frac{\partial u}{\partial x} + k_{xy}\left(\frac{\partial u}{\partial y} + \frac{\partial u}{\partial y}\right) + k_y\frac{\partial v}{\partial y}\right] - E\delta\left(k_x^2 + 2k_{xy} + k_y^2\right)w \tag{4.34}$$

where $\nabla^2 = \dfrac{\partial^2}{\partial x^2} + \dfrac{\partial^2}{\partial y^2}$, p_z is the load per unit area of the middle surface in the direction of the normal deformation load, δ is the shell thickness, $K = \dfrac{E\delta^3}{12(1-\nu^2)}$ is flexural rigidity of the shell, ν Poisson's ratio, E elastic modulus, $k_x = \dfrac{1}{r_x} = \dfrac{\partial^2 z}{\partial x^2}$, $k_y = \dfrac{1}{r_y} = \dfrac{\partial^2 z}{\partial y^2}$ and $k_{xy} = \dfrac{1}{r_{xy}} = \dfrac{\partial^2 z}{\partial x \partial y}$ are the curvatures of the middle surface in the directions x and y, respectively.
The expression for the displacement associated to each *propagating shape* of wavenumber $k_i(\omega)$ is:

$$w_i(x,t) = \varphi_i(x)e^{-J\omega t} = \int_{-\infty}^{+\infty}\Phi(k_i)e^{J(k_i x - \omega t)}dk_i = \int_{-\infty}^{+\infty}\Phi(k_i(\omega))e^{J(k_i(\omega)x - \omega t)}dk_i(\omega) \tag{4.35}$$

where $\Phi(k_i) = \mathcal{F}\left(\varphi_i(x)\right)$ and the integral form assumes the meaning of the limit for derivation order $n \to \infty$.
The upper plot of Figure 4.8 shows the real part of the first twenty wavenumbers re-

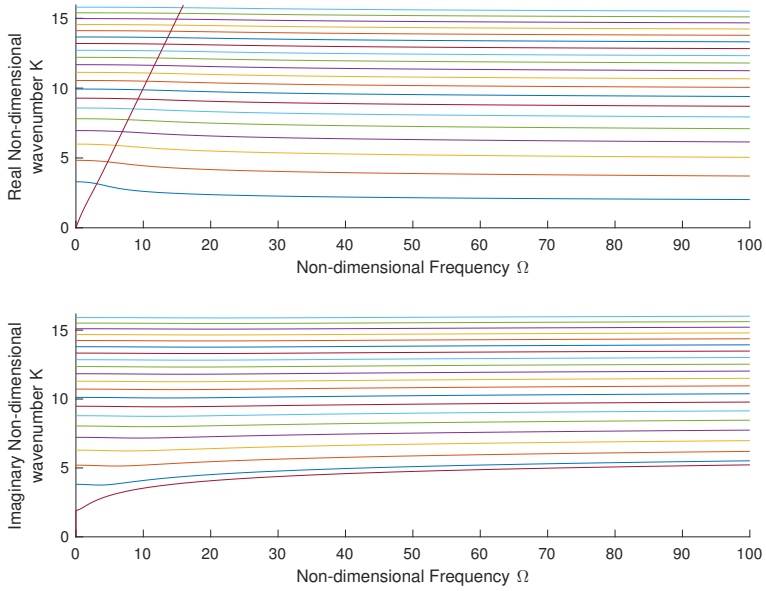

Figure 4.8. Propagation modes wavenumbers for the Gaussian-like force.

lated to the propagation modes, together with the purely real standard propagation

wavenumber, related to the standard wave (sloping curve). The lower plot displays imaginary parts and the lowest curve represents a purely imaginary wavenumber. Therefore, the general solution to the equation of motion is:

$$w(x,t) = \sum_{i=1}^{+\infty} \int_{-\infty}^{+\infty} \Phi(k_i) e^{J(k_i x - \omega t)} dk_i = \sum_{i=1}^{+\infty} \int_{-\infty}^{+\infty} \left[\Phi_+(k_i) e^{J(k_i x - \omega t)} + \Phi_-(k_i) e^{J(k_i x - \omega t)} \right] d\omega \tag{4.36}$$

This expression matches the double nature of the solution, as a mixing of propagation and mode response, through the presence of an integral (normally related to the response representation for infinite-size systems) and summation (normally related to the modal response in finite-size systems).
The arising of 1D *propagating shape* is a remarkable feature of the long-range structure here investigated and this property represents an additional common point with Tarasov theory [54], even though it does not analyse the dynamic behaviour of the investigated systems. Indeed, considering equation (2.21) only the terms comparable with the equation of motion (3.5), for clarity here reported again

$$\rho\, \boldsymbol{u}_{tt}(\boldsymbol{x},t) + \frac{E}{2(1+\nu)} \left[\nabla^2 \boldsymbol{u}(\boldsymbol{x},t) - \frac{1}{1-2\nu} \nabla \left(\nabla \cdot \boldsymbol{u}(\boldsymbol{x},t) \right) \right] + \int_{\boldsymbol{\xi} \in \mathbb{R}^3} f(|\boldsymbol{r}|) \boldsymbol{r}\, dV = 0$$

the trascendent characteristic of the associated dispersion relationship emerges:

$$\omega^2 - 2 \sum_{n=1}^{+\infty} \frac{\cos(kn\Delta x)}{n^{1+\alpha}} = 0 \tag{4.37}$$

This implies that, even in this case, a set of infinite numerable values of the wavenumber is associated to any single value of the frequency.
However, even though interesting, the present work investigates infinite-size systems, in which only the propagating component of a wave deserves attention. For this reason, it makes more sense to reinterprete the dispersion relationship in terms of $\omega(k)$ imposing the constrain of real wavenumber and then evaluating the frequency. The revisited forms of the dispersion relationship are:

$$\Omega = \pm K \sqrt{1 - \chi e^{-\frac{K^2}{4}}} \tag{4.38}$$

for the Gauss-like force, and

$$\Omega = \pm K \sqrt{1 - \frac{8\chi}{\sqrt{\pi}(K^2+1)^2}} \tag{4.39}$$

for the Laplace-like.
Equations (4.38) and (4.39) can exhibit imaginary values for specific regions of wavenumbers and values of χ. This means that the waveguide might become unstable with unbounded amplitudes, when long-range forces present a negative stiffness larger than the classical elastic one.
The arising propagating phenomena are discussed in the next section, but for the Gauss-like force only, since the Laplace distribution produces very comparable results.

4.4 Propagation characteristics

The inquiry of the propagation characteristics can be reduced to the analysis of dispersion curve, group and phase velocity in terms of the parameter χ only, since it is the only one affecting the dispersion relationship, as in equation (4.38). For this reason, dispersion relationship, phase and group velocities are discussed for different ranges of χ, namely i) $\chi \ll -1$, ii) $-1 < \chi < 1$ and iii) $\chi \gg 1$.
For the Gauss-like interaction, the expressions of phase and group velocity are:

$$C_\varphi = \frac{1}{c}\frac{\omega}{k} = \frac{\Omega}{K} = \sqrt{1 - \chi e^{-\frac{K^2}{4}}} \tag{4.40}$$

and

$$C_g = \frac{1}{c}\frac{\partial \omega}{\partial k} = \frac{d\Omega}{dK} = \frac{1 + \chi e^{-\frac{K^2}{4}}\left(\frac{K^2}{4} - 1\right)}{\sqrt{1 - \chi e^{-\frac{K^2}{4}}}} \tag{4.41}$$

respectively, where $c = \sqrt{\frac{E}{\rho}}$ is the speed of sound.
Figure 4.9 shows the trend of the nondimensional dispersion relationship for different values of χ smaller than -1, compared to the d'Alembert case, represented by the red dotted line. For $\chi \ll -1$, the already mentioned "surprising" effects start to

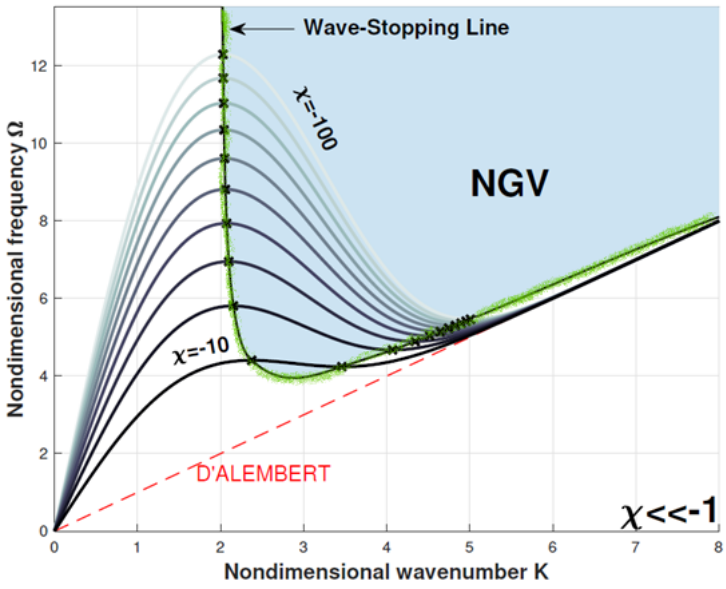

Figure 4.9. Dispersion relationships for different $\chi \ll -1$

occur. The group velocity, as derivative of the dispersion relationship, can be easily deduced by Figure 4.9. Indeed, the shape of the dispersion curve, unconventional by itself, displays the existence of two regions: a branch with a positive slope, which means positive group velocity, and a branch characterised by a negative slope, hence negative group velocity. While the positive group velocity promotes a standard wave propagation within the system, the negative group velocity is

rather uncommon and this is a first meaningful effect introduced by the long-range interactions. For higher values of the nondimensional wavenumber, all curves converge towards the conventional d'Alembert case. This variation in the trend of curves implies the existence of two points for each curve in which the tangent is horizontal: a maximum and a minimum at which the group velocity vanishes. This aspect discloses the existence of conditions for which wave-stopping occurs. Wave-stopping is a phenomenon proper of wave envelopes, being associated to the group velocity. This means that propagation is prevented to the envelope, which stands still, while the single wave components continue to travel along the waveguide. The region defined by the pairs of these points is the one characterised by the negative group velocity and is delimited on one side by the so-called wave stopping line, geometric locus of points corresponding to null group velocity.
It is interesting to notice that the trend of the dispersion curve recalls the one experimentally obtained by Eringen [41], when investigating the motion of phonons within aluminum, and depicted in Figure 4.10. As previously mentioned, the similarity cannot be associated to a closeness of the proposed models, but it underlines the key role played by nonlocalities when dealing with wave propagation phenomenon.
To better inspect these aspects the plots of the group velocity and phase velocity

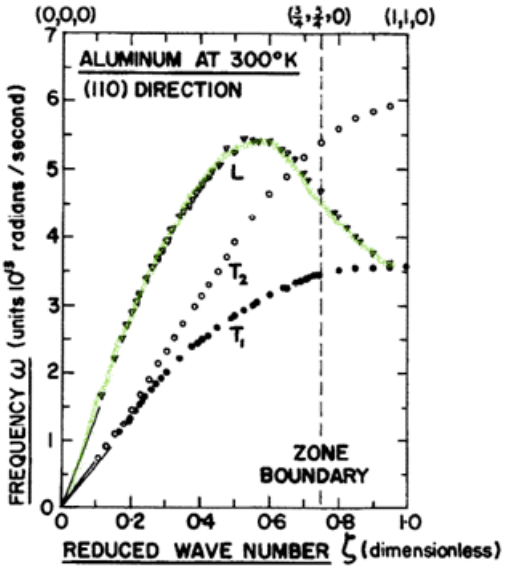

Figure 4.10. Experimental dispersion curve

are reported in Figure 4.11 and Figure 4.12, respectively.
In Figure 4.11, where the group velocity is plotted versus the wavenumber, one can recognise the same effects discussed in the dispersion curve analysis: the existence of wavenumbers pair for which the group velocity vanishes and the presence of a bandwidth of negative values of the group velocity. Moreover, the higher is the values of χ, the larger is the wavenumber bandwidth in which the system performs negative group velocity propagation.
Compared to the conventional waveguide, the phase velocity at low frequencies

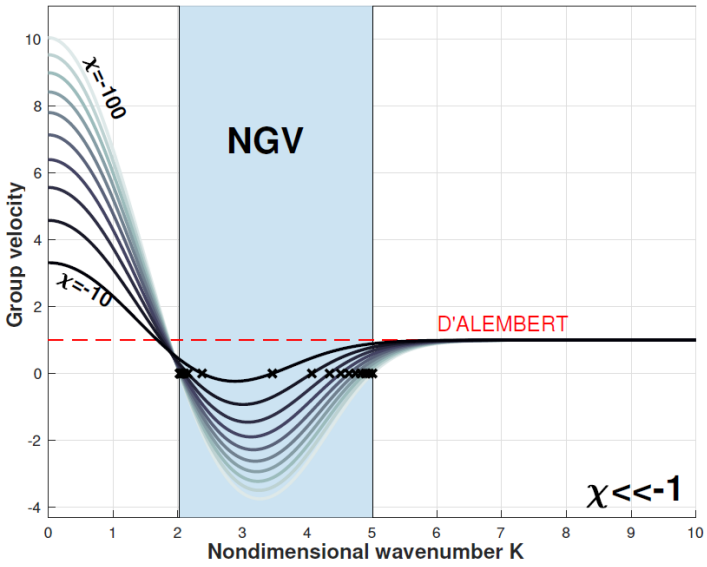

Figure 4.11. Group velocity for different values of $\chi \ll -1$

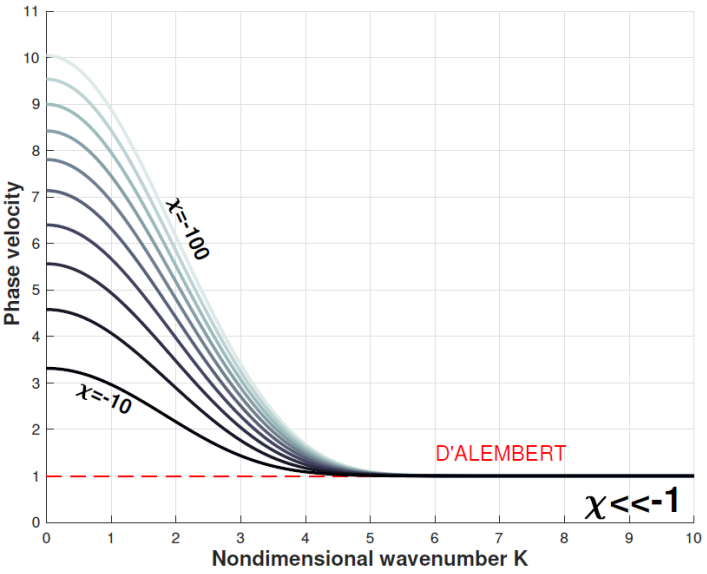

Figure 4.12. Phase velocity for different values of $\chi \ll -1$

assumes values considerably higher, but it is a trend that disappears for increasing values of the frequency, when it tends to the d'Alembert case, as it has happened for both dispersion curve and group velocity.

Since χ provides a measure of the strength of the long-range interactions compared to the classical elastic ones, a range of χ between -1 and 1 is associated to long-range forces of the same order of the short-ranges. If the long-range effect becomes less predominant, one can expect a global behaviour to be much akin to the standard d'Alembert waveguide and converging to it the more χ tends to zero, as one can infer from Figure 4.13.

Wave-stopping effects do not occur, and the group velocity is always positive, as

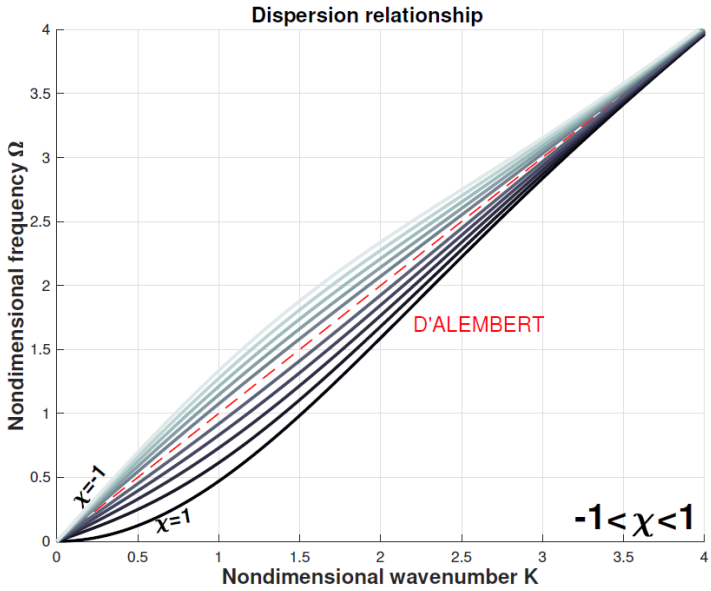

Figure 4.13. Dispersion relationships for different $-1 < \chi < 1$

confirmed by Figure 4.13.

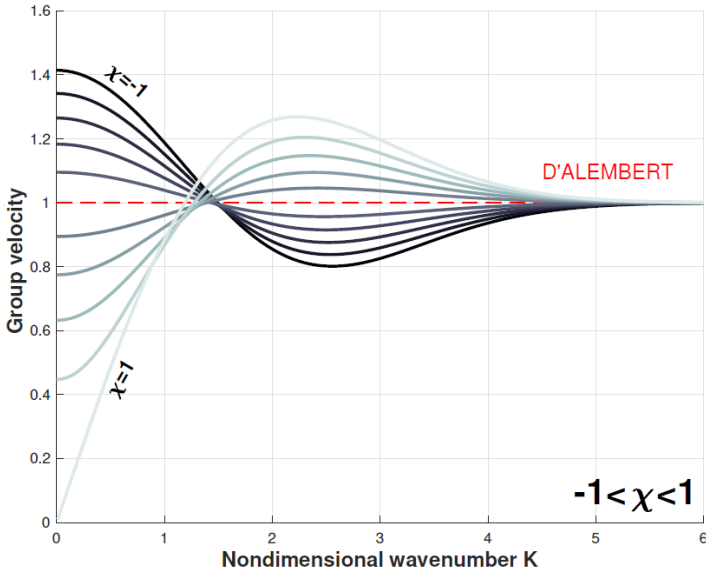

Figure 4.14. Group velocity for different values of $-1 < \chi < 1$

Eventually, the range of $\chi \gg 1$ is considered. For low values of the wavenumber, the dispersion relationship produces purely imaginary solutions only. This implies the amplitude of waves becomes unbounded and propagation is prevented. In a finite size system, imaginary (or in general complex) solutions are usually related to local effects and produce near field waves, appearing either at the boundaries of the

system, when obstacles occur, or where punctual external forces are applied. This type of waves exponentially vanishes within a narrow region around their source. In an infinite size system, since no boundary conditions would be meaningful and given the fact that no external forces are here considered, this type of waves is surely vanishing in one direction, but no reason of confinement occurs in the opposite one, leading to unbounded amplitudes and hence instability. The unstable region appears for the dispersion curves (Figure 4.15), but also for group (Figure 4.16) and phase (Figure 4.17) velocities, and it can be noticed how the higher is the value of the parameter χ, the larger is the unstable region.

Outside the unstable region, solutions turn to real values and propagation occurs.

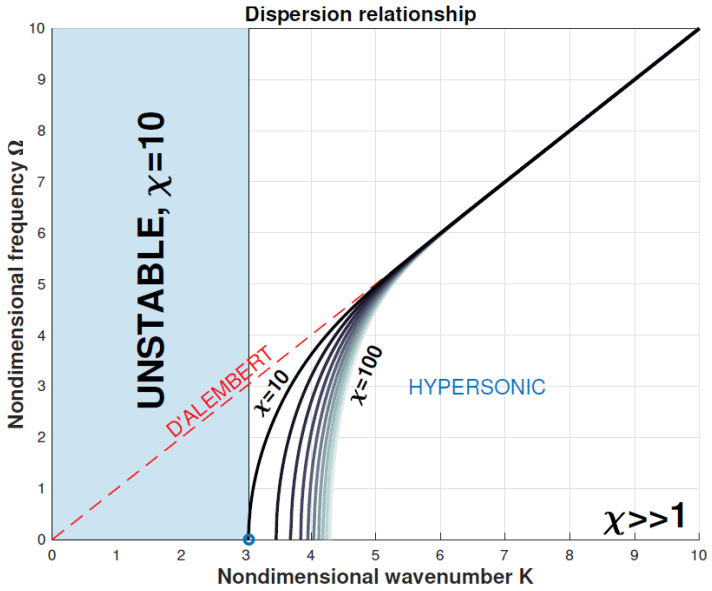

Figure 4.15. Dispersion relationships for different $\chi \gg 1$

In a very narrow wavenumber bandwidth, all the curves pass from a very high slope to converge rapidly to the D'Alembert curve, so to a standard propagation regime. In this badnwidth both group and phase velocities are much larger than the wave speed associated to the conventional propagation. Especially the group velocity tends to infinite, meaning the birth of hypersonic/superluminal propagation. Even tough an infinite velocity might sound impossible, due to the the theory of relativity, it has to be remembered that the group velocity is the velocity neither of a particle nor of an information. The speed of light in vacuum is an insuperable limit for a signal or a particle speed: this implies that what just found does not object Einstein's theory, which only imposes an upper bound to the speed of any moving object.
The concept of superluminal propagation, even if it could sound as a pure theoretical digression, it has already been investigated. In [112], Sommerfeld and Brillouin discuss how a wave envelope propagating with a group velocity larger than the speed of light can occur in dissipative media and absorptive materials. While investigating anomalous dispersion for mechanical oscillators, they theoretically show that inside an absorption band, the dispersion is anomalous, and the result is a group velocity that can become faster than c, the vacuum speed of light, or

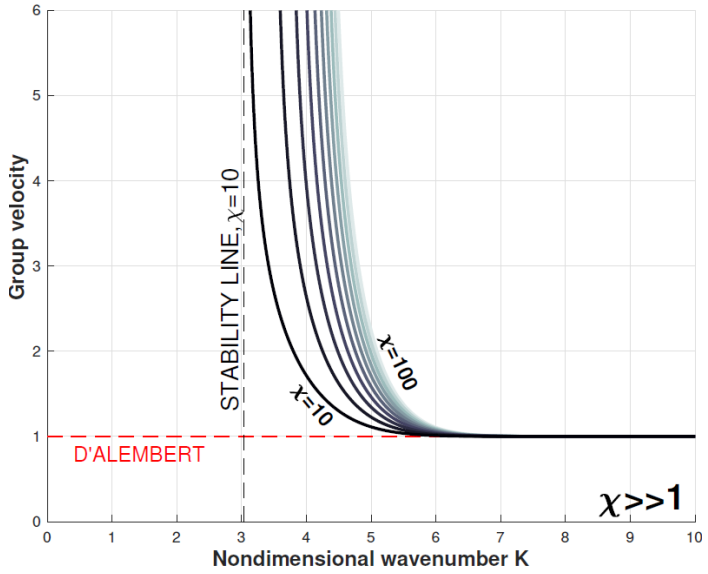

Figure 4.16. Group velocity for different values of $\chi \gg 1$

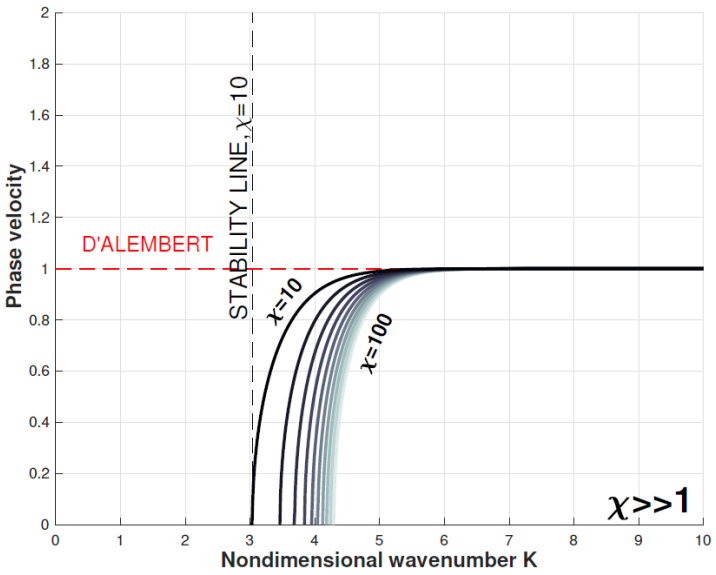

Figure 4.17. Phase velocity for different values of $\chi \gg 1$

even negative. The contradiction between the limitation from relativity and a superluminal group velocity is solved, as casuality only requires the speed of a signal carried by light to be limited by c, while the light pulse can travel at the group velocity. However, in our case, the long-range interactions are modelled as elastic connections and the system is thus conservative: superluminality is only related to the elastic topology. In [113–115], the authors experimentally demonstrate that the group velocity exceeding the speed of light is possible and in some cases might also become negative for free-loss systems: "*We suggest here an operational definition of the signal velocity and apply it to the recently observed superluminal propagation of a*

light pulse in a gain medium. This experiment showed not only that a superluminal group velocity is possible without any significant pulse distortion, but also demonstrated that this can occur with no appreciable absorption or amplification." [115]. Kuzmich et Al. analyse a gain-assisted linear anomalous dispersion to experimentally demonstrate that light propagation in atomic caesium gas can achieve superluminal regimes. Measuring the group velocity they find out that "*a light pulse propagating through the atomic vapour cell appears at the exit side so much earlier than if it had propagated the same distance in a vacuum that the peak of the pulse appears to leave the cell before entering it. The observed superluminal light pulse propagation is not at odds with causality, being a direct consequence of classical interference between its different frequency components in an anomalous dispersion region.* [113].
However, in order to complete the investigation including the dissipation effect, a viscous contribution is introduced in the equation of motion 4.21.

$$\rho\frac{\partial^2 w}{\partial t^2}+\gamma\frac{\partial w}{\partial t}-E\frac{\partial^2 w}{\partial x^2}-g(x)*w(x)=0 \tag{4.42}$$

The approach is the same: given the dispersion relationship, the results are discussed in terms of group velocity.
The nondimensional relationship is (see Appendix C for the mathematical procedure):

$$\Omega=-\jmath\frac{\Gamma}{2}\pm\sqrt{Q^2-\left(\frac{\Gamma}{2}\right)^2} \tag{4.43}$$

where $\Gamma=\dfrac{\gamma\beta}{\sqrt{\rho E}}$, $Q^2=K^2[1-\chi\phi(K)]$ and $\phi(K)=e^{-\frac{K^2}{4}}$ for the Gaussian case.
The group velocity is in general complex:

$$C_g=\frac{\partial\Omega}{\partial K}=\pm\frac{1}{\sqrt{1-\left(\frac{\Gamma}{2Q}\right)^2}}\frac{\partial Q}{\partial K}=\pm\frac{1}{\sqrt{1-\left(\frac{\Gamma}{2Q}\right)^2}}C_{g_{\Gamma=0}} \tag{4.44}$$

where $C_{g_{\Gamma=0}}$ is the group velocity considered in the previous sections, i.e. in the absence of dissipation and in the presence of long-range interactions. It is interesting to notice that the expression of the group velocity appears in a factorised form and the contribution of long-range and dissipation are distinct and non combined.
Let us analyse the two extreme cases. In the absence of dissipation , $\Gamma=0$, and $C_g=C_{g\Gamma=0}$ is the group velocity analysed in this section. In the absence of long-range interactions, $Q=K$, and $\dfrac{\partial Q}{\partial K}=1$. The group velocity keeps only the dissipative contribution: $C_g=\pm\dfrac{1}{\sqrt{1-\left(\frac{\Gamma}{2Q}\right)^2}}$ and a discussion of that Γ can state the presence of superluminal effects, i.e. $C_g>1$ (as in [112]), which happens for $\sqrt{1-\left(\dfrac{\Gamma}{2Q}\right)^2}<1$ and. $\sqrt{1-\left(\dfrac{\Gamma}{2Q}\right)^2}$ real.
The merging of both effects, if they are simultaneously present, must be discussed in terms of both the parameters χ and Γ, since the amplitude of the real part of

C_g and whether it is smaller or larger than 1 depends on the choices of the ruling parameters.
In a nutshell, one can assure the rising of superluminal propagation when both long-range and dissipation occur; however, these two effects, depending on their intensity and on the frequency range, can be productively combined or they can interfere with each other.

A last consideration concerns the linearization procedure. In section 3.4, it has been underlined how the linearization holds under specific conditions: "*once the region of investigation is chosen in terms of K, the amplitude of vibration w_0 must be compared with the typical interaction length β for the linearization to be guaranteed.*". In this section, it has been shown that the most remarkable phenomena related to wave propagation, as wave-stopping and superluminality, emerge for K of order ~ 1, whilst for $K \to \infty$, the propagation characteristic collapses into the standard D'Alembert equation. This evidences that all these effects are valid and the linearisation approximation holds as long as the vibration amplitude is much smaller than the characteristic long-interaction length β: $w_0 \ll \beta$.

4.4.1 Notes on the modal density

The modal density is defined as the number of natural frequencies, hence of modes, within a defined frequency bandwidth $\rho_n(\omega) = \dfrac{N\left(\omega_f\right) - N\left(\omega_i\right)}{\left(\omega_f - N\omega_i\right)}$. Classically the modal density is a function that, being a "counter" of modes, is intrinsically related to finite-size systems. For homogeneous, simple systems there are expressions that provide the modal density in terms of the system parameters. For instance, the case of a longitudinal beam, simply supported, whose modes are equally distributed over the frequency domain, has a constant modal density distribution. Its expression, depending on the specific boundary conditions, is: $\rho_n = \dfrac{n\pi}{L}\sqrt{\dfrac{E}{\rho}}$, where n is a positive integer $n = 1, 2, 3, ...$, L is the length of the beam, $c = \sqrt{\frac{E}{\rho}}$ is the speed of sound, E is the Young's modulus and ρ is the density. However, this case, together with the cases of a bending beam, bending plate, are ideal representation of real structures as no dissipation is considered. The effect of dissipation induces, towards higher frequency ranges, a thickening of the mode distribution and a flattening of the modal density. This is particularly relevant for waves travelling at high frequencies: while a perturbation travelling at low frequency can be strong enough to reach the boundaries and being reflected, so to induce the inception of a mode shape, at high frequencies the damping considerably reduces the strength of a perturbation, which might vanish before reaching the edges of the system. In other word, at high frequencies, the dynamic behaviour of a finite beam can be considered as the one of an infinite beam, for which modes and natural frequencies loose their meaning, given the actual lack of wave reflections. It is exactly in this limit condition, for the length $L \to \infty$, that the concept of modal density might still be used to disclose other aspects of the dynamic response of a structure. The modal density, indeed,

can be obtained from the equation of motion, even when no boundary conditions can be defined. The result is a function that depends upon the frequency only.
The duality between finite and infinite systems, thus between discrete and continuous formulations, is a long-standing discussion, which involves the modal density as well.
From a physical point of view, there are many cases in which the modal density is implied for non-finite structures or when the boundary conditions are not relevant. Statistical Energy Analysis (SEA) is an example of how the concept of modal density is not necessarily addressed to strict boundary conditions, which are the mean to define a finite structure. Indeed, SEA replaces the real boundary conditions with special ones, usually easier to handle and for which the shape of the modes is known. This is allowed because, while at low frequencies the modes present a sensibly different shape, at high frequencies they become similar, and the small difference occurring at the boundaries is negligible; the real conditions are less influential and the constraints loose their particular meaning.
In finite structures, wavenumbers are distinct, and so are the modes. The wave forms are associated to the set of numerable wavenumbers $k_n = \frac{n\pi}{L}$ and expressed by:

$$\phi_n = \sin \frac{n\pi x}{L} \tag{4.45}$$

where n is a positive integer. If $L \to \infty$, the distribution of wavenumbers, discrete at first, becomes continuous, n is not integer any longer and k_n becomes a real number. However, the definition of a set of modes is still possible. Indeed, for a chosen frequency band $\Delta\omega$, there always exists an associated wavenumber band Δk, as shown in Figure 4.18, since Δn can be translated in $\Delta k = \Delta k(n)$. Thus, the relation between the frequency bandwidth and the wavenumber bandwidth defines the modal density. For $L \to \infty$, $\Delta k \to 0$, but also, and even better, Δk tends to its

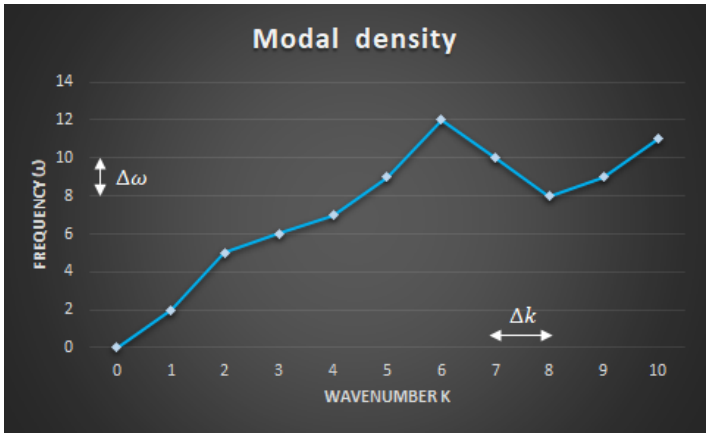

Figure 4.18. Modal density function

infinitesimal value dk. The curve representing the modal density in Figure 4.18, polygonal chain for a discrete set of pairs (ω_i, k_i), becomes a continuous curve related to infinite size systems. In both cases, $\frac{\Delta\omega}{\Delta k} = \rho_n \neq \rho_n(L)$ remains. The modal density is an invariant function with respect to the dimension L (unless a

mode normalization is applied) and, for $L \to \infty$, it tends to infinite, but globally, not punctually. This means that it keeps its shape and, in this small difference, the modal density can still be meaningful, also for unbounded media.
A certain correlation between the discrete and the continuous formulation can be demonstrated also from a mathematical point of view. Omitting the details, a structural displacement can be expressed in modal form:

$$\phi = \sin \frac{k\pi n}{L} \sin \omega_n t \tag{4.46}$$

or in wave form:

$$\sin (k_n x - \omega_n t) \tag{4.47}$$

The presence of a sinusoidal term in the wave form guarantees the existence of modes, if one accepts to interpret them as a $\sin k_n x$ form.

An aspect relevant for the present analysis stands in the fact that $\frac{dN}{d\Omega} \propto \frac{1}{C_g}$, which implies that the results obtained for the group velocity can be discussed also in terms of modal density. This relation can be proven comparing the expressions of the group velocity and of the modal density. The group velocity is rather straightforward, since it is defined based on the envelope speed: $C_g = \frac{dK}{d\Omega}$. Regarding the modal density, it has been already mentioned how it can be defined also in terms of wavenumber. If the modes are harmonic or complex exponential, which is in general true far from the boundaries, then the resulting wave behaves as sinusoidal wave form, hence $k_n = \frac{n\pi}{L}$ or simply $k_n \propto n$. This means that Δk can be expressed as $k_{n+1} - k_n = \frac{\pi}{L}$. If for a pair of consecutive wavenumber $\Delta k \propto n$, for a larger band, $k_{n+p} - k_n \propto p$, where p is the number of modes included in the interval $\left[\omega_n; \omega_{n+p}\right]$. As result, for the modal density the relation $\rho_n = \frac{\Delta n}{\Delta \omega} \propto \frac{\Delta k}{\Delta \omega}$ holds. Eventually, considering nondimensional parameters, the limit to infinite lengths leads to $\rho_n \propto \frac{dK}{d\Omega} \propto \frac{1}{C_g}$.

The modal density has been analysed for the same χ ranges, previously investigated, and displayed vs wavenumber. For $\chi \ll -1$, the trend of the modal density is presented by Figure 4.19.
The plot confirms what discussed for dispersion curve, group and phase velocity within the same χ range. The modal density exhibits two peaks; given the high values of the modal density at these points, corresponding to vanishing group velocity, the singularities imply an energy storage effect in the waveguide; indeed, if the energy is trapped within a very narrow bandwidth, propagation is prevented and wave-stopping takes place.

The range of χ delimited by -1 and 1, which did not unveil special effects for dispersion curve and group velocity, becomes very interesting when dealing with the modal density, shown in Figure 4.20. For any value of the parameter χ, the curve presents two regions: a positive region, on the left hand side with respect

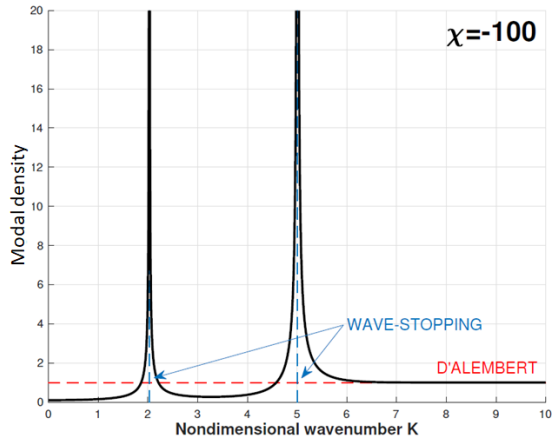

Figure 4.19. Modal density for different values of $\chi \ll -1$

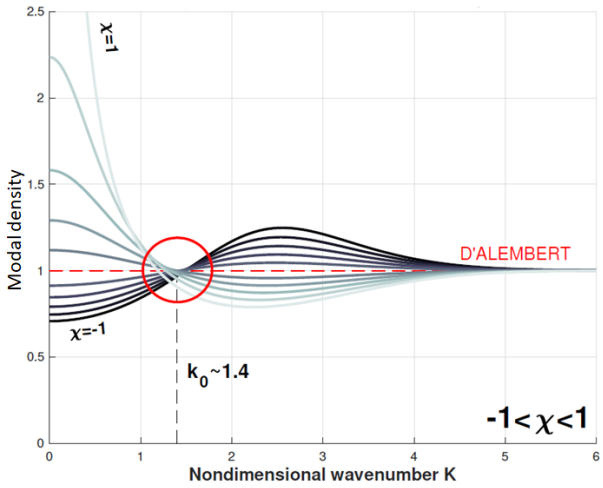

Figure 4.20. Modal density for $-1 < \chi < 1$

to the intersection with the D'Alembert curve, and a negative region on the right hand side. This implies that in the region before the intersection, which has a higher modal density compared to the standard waveguide, there is a gain in terms of number of modes, as well as there is a reduction in the region after k_0. Furthermore, the evaluation of the modal density, with respect to the frequency, within the two regions, as shown in Figure 4.21, reveals the two areas to be equal: $\int_0^{\Omega(k_0)} \left(\frac{dN}{d\Omega} - 1\right) d\Omega = \int_{\Omega(k_0)}^{+\infty} \left(1 - \frac{dN}{d\Omega}\right) d\Omega$, where $\frac{dN}{d\Omega}(k_0) = 1$. This means that the number of modes gained by the waveguide in the interval $[0, \Omega(k_0)]$ matches the number of modes lost in the interval $[\Omega(k_0), +\infty]$. This phenomenon can be interpreted as a *mode-migration* from high to low frequencies, around the wavenumber k_0, defined as *folding wavenumber*. The curves for all values of χ fold in a very narrow region abound the value $k = 1.4$. This has reflections on the group velocity; when the values of the modal density are high, the energy is trapped and its propagation is slowed down, consequently also the group velocity suffers a reduction, as in Figure 4.14.

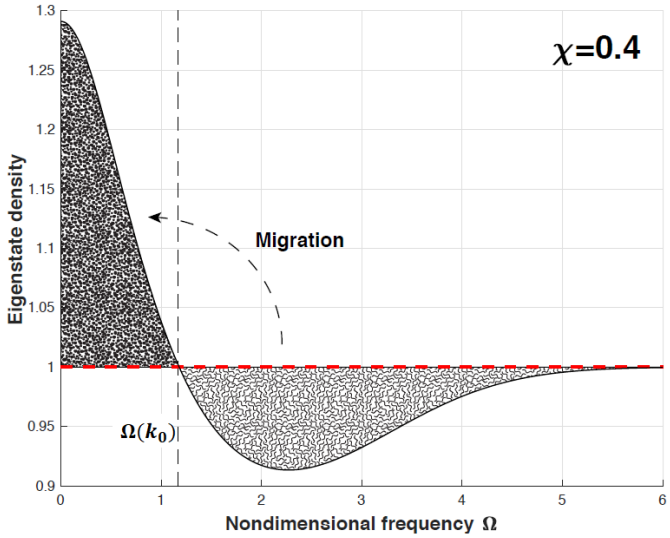

Figure 4.21. Modal density vs frequency for $\chi = 0.4$

Eventually, for $\chi \gg 1$ the modal density, shown in Figure 4.22, mirrors the effects already discussed for dispersion curve and the group velocity, in relation to the superluminal propagation and to the following convergence to the D'Alembert behaviour.

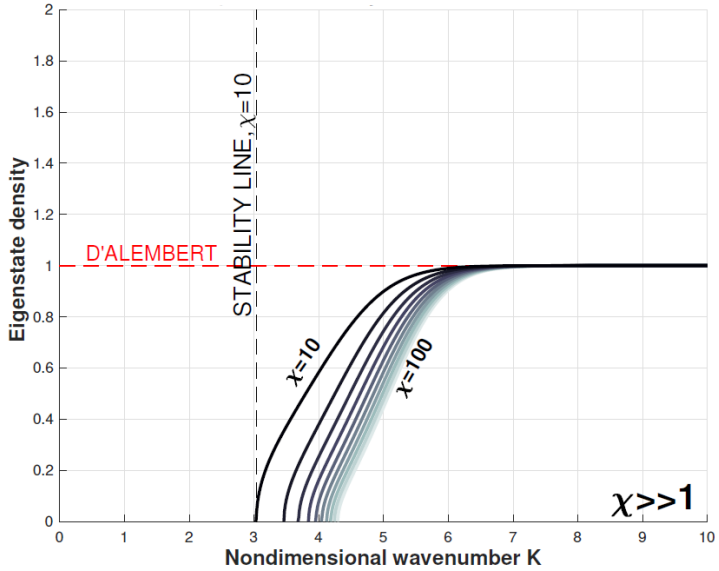

Figure 4.22. Modal density for different values of $\chi \gg 1$

Note that the comments regarding the correlation between modal density and energy of the system are not immediate and mathematically justified; however, they are based on the energy equipartition principle that, applied over the modes, states the amount of energy received and absorbed by each mode to be the same. This

means that a region with a higher modal density is able to absorb a larger amount of energy, with consequences over the velocity of waves and wave envelope, as a region with lower modal density, thus with a lower number of modes, has a limit on the energy storage capacity. A clear example is represented by the wave-stopping effect. This phenomenon is firstly demonstrated by the group velocity trend, but it is also confirmed by the modal density behaviour. Corresponding to the singularities, the modal density has a considerably high value, which means that in a narrow bandwidth there is a high number of modes, hence a trapping of the energy, and the envelope hardly propagates.

Finally, Figure 4.23 represents a map of the possible propagating scenarios, when a Gauss-like type of long-range interaction is introduced within the structure: the negative group velocity region (NGV) is delimited by the wave-stopping curve, the unstable region is confined within superluminal curves and all the lines are isofrequency contours. Since the characteristics of the Gauss-like force are rather general, and mainly related to the decaying with the distance feature, this map provides a universal description of the propagating regimes existing in an elastic metamaterial supplied with long-range interactions.

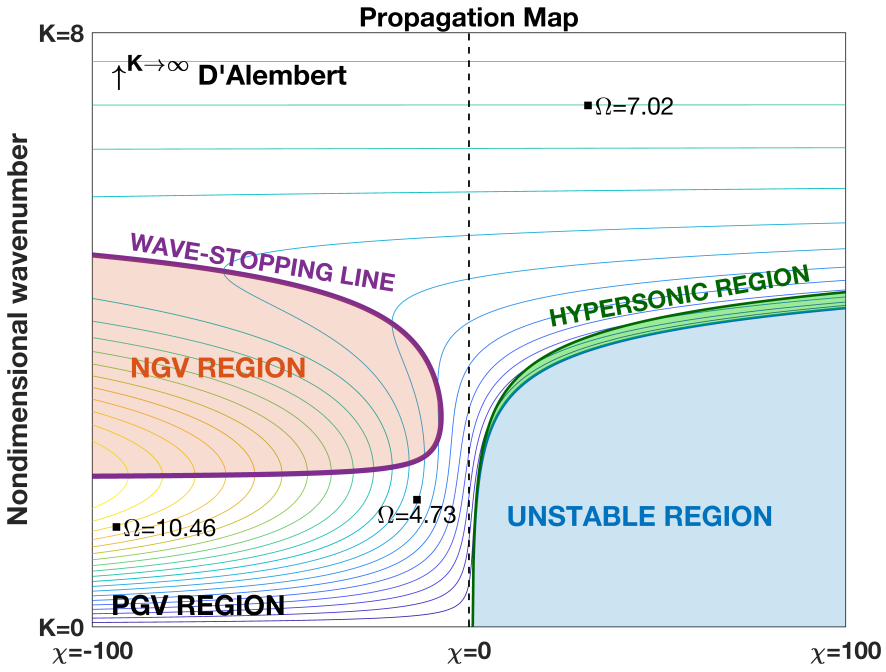

Figure 4.23. Propagation Map for instant long-range interaction

4.4.2 Space-Time visualisation

To complete the investigation space-time visualizations are presented. They have the great advantage to be direct solutions of the equation of motion and there is

no need consider the discrete counterpart of the problem, which is a mandatory step to perform numerical simulations. Numerical simulations, indeed, should be used with carefulness when dealing with phenomena of propagation. There are two main problems:

- discretization procedure and mesh distort the propagation phenomenon, also in simple cases. Numerical simulations are based on the comparison between the solution of a differential equation, related to the continuous model, and the one of the finite difference equation, related to the discrete model. Theoretical investigations have shown that the first solution is of an exponential type e^t, the second one is z^k, with k integer and z complex. For a discretization step dt that tends to zero, the two solutions coincide, but for larger dt they are different, until the limit at which, while e^t is an oscillating harmonic solution, z^k does not oscillate any more and it monotonically decreases or increases. Finding the condition between an acceptable comparison and a large distortion is not always an easy task (an example is provided by Lax equation [116]). It can be shown that even for a problem not badly conditioned, the solution of the finite difference equation results distorted when compared with the continuous one;
- a second issue is related to the boundary conditions. To solve numerically discretized equations, the boundary conditions must be specified. In the case of integral-differential equation, the boundary conditions are of the same nature, hence complex to define.

To perform space-time visualization, the shape of the propagating signal is imposed in the form:

$$w(x,t) = \sum_{i}^{N} \left[W_i^{(1)} \sin\left(k_i x - \omega(k_i)t\right) + W_i^{(2)} \cos\left(k_i x - \omega(k_i)t\right) \right] \tag{4.48}$$

where $W_i^{(1)}$ and $W_i^{(2)}$ are coefficients depending on initial conditions, and $\omega(k_i)$ is specified by the dispersion relationships (4.38) and (4.39). The displacement is expressed as a Fourier series, i.e. a discrete approximation of a continuous shape. The analysis of the space-time development of the displacement has been carried on according to the range of $\chi \ll -1$ and $\chi \gg 1$ previously introduced, except for the case of $-1 < \chi < 1$ as no special effects have been observed for group and phase velocity. In particular, sections at different times of the surface $w(x,t)$ are shown, where the red dot indicates the phase velocity, the green square the group velocity and dotted lines highlight these points moving in space and time.

In the range of $\chi \ll -1$, two separate phenomena appear: negative group velocity and wave stopping. To better visualise them and according to the dispersion curve shape, the travelling wave packet is shown for $\chi = -100$ and in three different conditions, shown in Figure 4.24: i) $\Omega = 10$ and $K = 1.4$, condition along the positive slope of the dispersion curve (arch around A), where both group and phase velocities are positive, ii) $\Omega = 10$ and $K = 3$ on the negative branch (arch around B), where negative group velocity is displayed, iii) $\Omega = 12$ and $K = 2$ about the

maximum peak of the curve (point C), where wave-stopping takes place.
Figure 4.25, corresponding to condition i) and ii), shows on the left hand side the

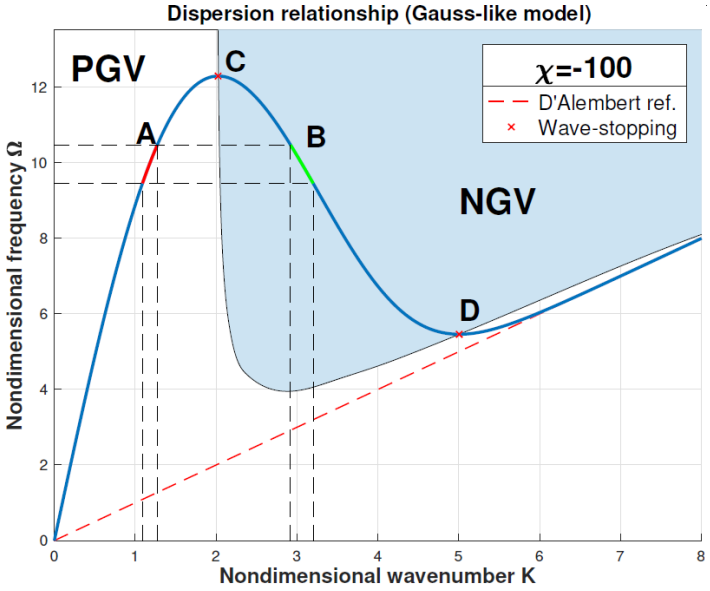

Figure 4.24. Dispersion curve

trend of phase and group velocity at low wavenumbers, while on the right hand side the range of high wavenumbers is considered and the result confirms what in the previous section observed. While in the figure corresponding to the positive group velocity region, both the single wave and the envelope proceed forward and phase and group velocity are consistent with each other, in the negative group velocity region to a forward travelling wave corresponds an envelope that propagates backward, and negative group velocity is assumed by the wave packet.
Figure 4.26, corresponding to condition iii), compares the propagation within the standard D'Alembert waveguide on the left hand side with the propagation occurring within a long-range waveguide, on the right hand side. The wave-stopping phenomenon is apparent since the single wave travels in time, following the phase velocity line, while the envelope stands still and its shape is frozen.

For $\chi \gg 1$ the arising phenomenon was the superluminal propagation. Figure 4.27 compares the propagation of a standard waveguide and, once again, the behaviour of the long-range waveguide. For high values of the parameter χ the long-range waveguide, on the right side, shows an incredibly fast propagation, compared to the conventional one on the left side, which almost remains still. Phase velocity instead, according to Figure 4.17, rapidly vanishes.

4.5 Final remarks

Long-range interactions might produce extremely complex systems, depending on their nature and on how entangled is the network of elementary particles. In this context, the intention is to define the general propagation properties related to the

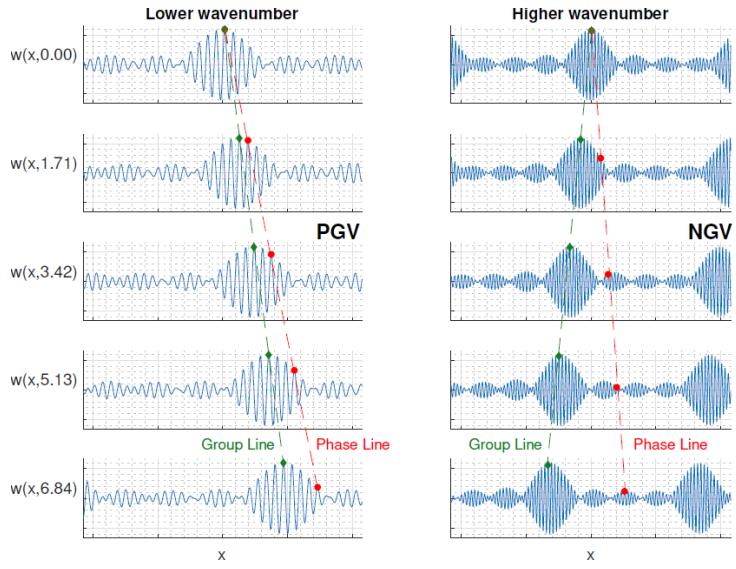

Figure 4.25. Left: positive group velocity, Right: negative group velocity

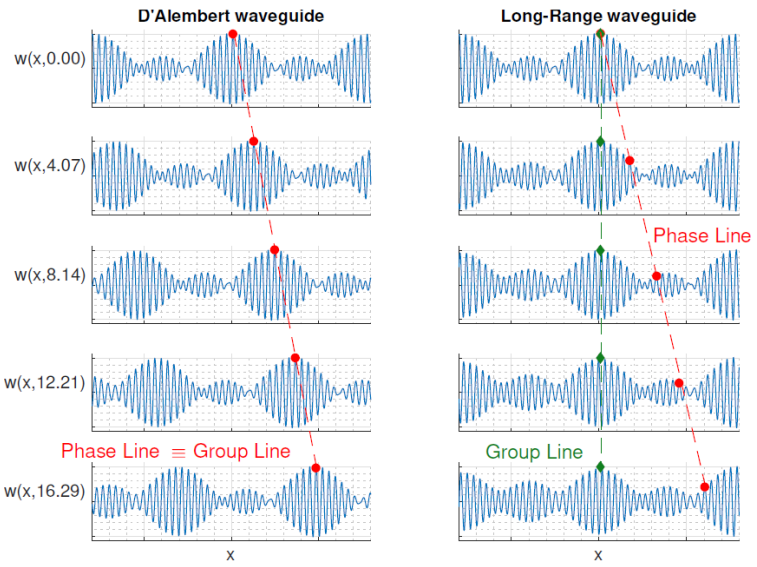

Figure 4.26. Left: D'Alembert waveguide Right: Long-Range waveguide

long-range interactions. For this purpose, special kernels are chosen to model the long-range connections, applied to the case of a simple one-dimensional waveguide; these kernels have the remarkable property to produce analytical solutions to the equation of motion, so to reduce the difficulties arising from the nonlocal properties. This chapter illustrates the formulations used to model the long-range interactions, and eventually the Gauss-like force is selected to develop a proper wave propagation analysis. This model, as well as the Laplace-like force, has a shape that well mimics the magnetic coupling and, in general, natural long-distance decaying forces. Besides, the known analytical form of its Fourier Transform ensures the achievement of closed form analytical solutions. The analysis of the propagation

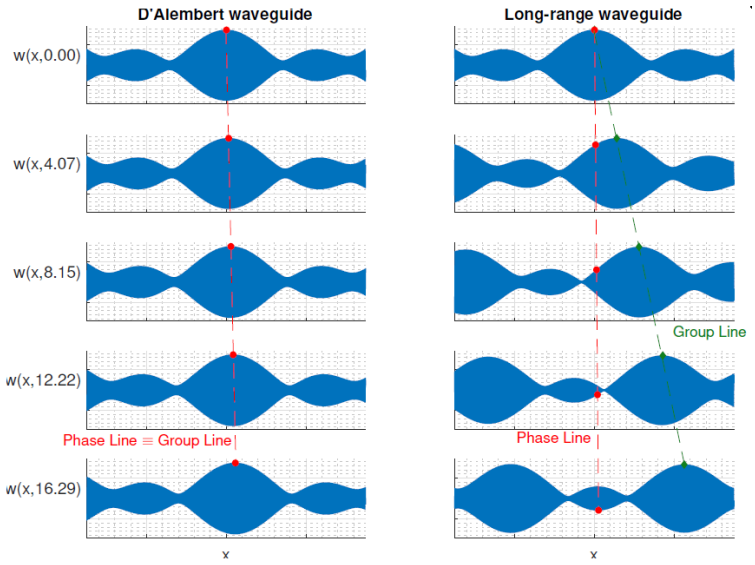

Figure 4.27. Left: D'Alembert waveguide, Right: Long-Range waveguide

properties is thoroughly developed and it is discussed in terms of propagation velocity, modal density, and the extraordinary emerging phenomena are in detail described.

Chapter 5

Coupled waveguides and twin waves: theory, simulations and experiments

To complete the description of the long-range interaction family, within the elastic metamaterial panorama, the case of a coupled system is considered as a natural extension of the single waveguide example. These long-range interactions have a radius of influence and, since the interaction with matter does not intensively affect them, they can condition distinct objects, when no structural connections are present, and even a group of them. Although many author have examined long-range interactions, literature does not provide many examples of dynamic behaviour of a system coupled because of the long-range interaction. In this context, the investigation of the *twin system* is an absolute novelty.
The straightforward approach showed in [43] has been applied to the topic investigated in [83]. The analysed system is composed by two identical, continuous, unbounded waveguides (*twin system*), in which long-range interactions act in addition to the conventional elastic connections. A Gauss-like type of force is used to model these long-range interactions, and it mimics magnetic coupling. The advantages related to the application of this type of forces was already demonstrated: they accurately model natural forces and lead to analytical solution of the equation of motion, since their Fourier Transform has an analytical expression. A long-range interaction exists within the single waveguides, but also in the case of the *twin system*. Indeed, with no external connection involved, it can be seen how the two rod-like structures are coupled with each other, thanks to the magnetic interaction only. The mathematical analysis anticipates the existence of unconventional propagating phenomena, which are confirmed by numerical simulations. Finite elements analysis and an experimental campaign complete the investigation.

5.1 Model for interacting waveguides

In this context, we are not interested in the discussion of the results obtained for a single waveguide, already exhaustively presented. However, the same approach

and its related analysis are applied for a more sophisticated system that involves the coupling between two structures at first, but that could be further extended to multiple components.
The remarkable aspect stands in the capability of structures equipped with long-range interactions to communicate, even when set apart with no structural connection in between. Different types of coupling can be realised and consequently different propagating scenarios can be performed, making long-range interactions a powerful way to achieve unusual dynamic response, remote control and multiple systems intelligence.
The equation of motion, as presented in (3.5), must be considered in its overall formulation so to consider the cross-correlation action, expressed by the second integral:

$$\rho\, \boldsymbol{u}_{tt}(\boldsymbol{x},t) - \frac{E}{2(1+\nu)}\left[\nabla^2\boldsymbol{u}(\boldsymbol{x},t) + \frac{1}{1-2\nu}\nabla\left(\nabla\cdot\boldsymbol{u}(\boldsymbol{x},t)\right)\right] + \\ + \int_{\boldsymbol{\xi}\in\mathbb{R}^3} f(|\boldsymbol{r_s}|)\boldsymbol{r_s}\, dV + \int_{\boldsymbol{\eta}\in\mathbb{R}^3} f(|\boldsymbol{r_{cr}}|)\boldsymbol{r_{cr}}\, dV = 0 \quad (5.1)$$

In this section, the equations of motion of a coupled system are derived in a form according to equation (4.21), for the system shown in Figure 5.1 and named *twin system*. The system is composed by two identical, rod-like structures, set at a distance smaller than the typical long-range interaction length. In these conditions, the inter-body forces are not negligible with respect to the intra-body ones and the overall dynamic behaviour is profoundly affected. Indeed, each point of the waveguides is subdued to forces, modelled as Gauss-law, generated by each point of both its own waveguide and the other one.
The problem so presented is two-dimensional; however, it is reasonable to neglect

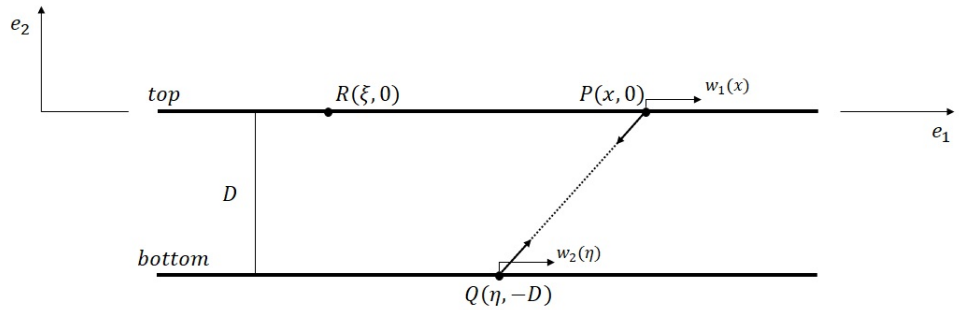

Figure 5.1. Twin waves model

the displacement along the z-axis and consider the longitudinal displacement only, thus only the x-axis component of the long-range force remains. Moreover, inter-body and intra-body forces are assumed to be only dependent on the distances $\overline{\boldsymbol{PQ}}$ and $\overline{\boldsymbol{PR}}$, respectively. In particular, $\overline{\boldsymbol{PQ}} = |\boldsymbol{r_{cr}}| = \left[(x-\eta+\varepsilon_{cr1})^2 + D^2\right]^{\frac{1}{2}}$, where $\varepsilon_{cr1} = w_1(x) - w_2(\eta)$ is the cross-distance, and $\overline{\boldsymbol{PR}} = |\boldsymbol{r_s}| = x - \xi + \varepsilon_{s1}$, with $\varepsilon_{s1} = w_1(x) - w_1(\xi)$ the intra-distance.
The linearised expression of the long-range forces, as mention in section 3.4, is

applied to both inter- and intra-body interaction.

$$\boldsymbol{F}\left(\boldsymbol{r_{cr}}\right) = f\left(|\boldsymbol{r_{cr}}|\right)\boldsymbol{r_{cr}} = f_0 \cdot (\boldsymbol{x} - \boldsymbol{\eta}) + \boldsymbol{h_0}\boldsymbol{\varepsilon_{cr}} + f_0\boldsymbol{\varepsilon_{cr}} \tag{5.2}$$

$$\boldsymbol{F}\left(\boldsymbol{r_s}\right) = f\left(|\boldsymbol{r_s}|\right)\boldsymbol{r_s} = f_0 \cdot (\boldsymbol{x} - \boldsymbol{\xi}) + \boldsymbol{h_0}\boldsymbol{\varepsilon_s} + f_0\boldsymbol{\varepsilon_s} \tag{5.3}$$

The subscript *cr* denotes the cross-correlation term, and the subscript *s* the contributions within the single waveguide. Focusing on the cross-interactions only, and analysing the effect exerted by the bottom waveguide to the top one, the force in equation (5.2) becomes:

$$\boldsymbol{F}\left(\boldsymbol{r_{cr}}\right) = \mu e^{-\frac{|\boldsymbol{r_0}|^2}{\beta^2}} \begin{bmatrix} (x-\eta) - 2\frac{(x-\eta)^2}{\beta^2}\left[w_1(x) - w_2(\eta)\right] + \left[w_1(x) - w_2(\eta)\right] \\ D - 2D\frac{(x-\eta)}{\beta} \end{bmatrix} \tag{5.4}$$

where the first row is the force along the x-axis, and the second is along the z-axis. As previously stated, only the former is considered and the associated force is:

$$F_x(x,\eta) = \mu e^{-\frac{1}{\beta^2}\left[(x-\eta)^2+D^2\right]}(x-\eta) - \mu e^{-\frac{1}{\beta^2}\left[(x-\eta)^2+D^2\right]}\left[1 - 2\frac{(x-\eta)^2}{\beta^2}\right]\left[w_1(x) - w_2(\eta)\right] \tag{5.5}$$

Among all the terms, when integrated over the entire domain, only the third one provides a non-zero contribution. The resulting action of the cross long-range forces, generated by the bottom waveguide affecting the top one, is:

$$\int_{\eta\in\mathbb{R}} \mu e^{-\frac{D^2}{\beta^2}} e^{-\frac{(x-\eta)^2}{\beta^2}}\left[1 - 2\frac{(x-\eta)^2}{\beta^2}\right] w_2(\eta)\, d\eta = -l(x) * w_2(x) \tag{5.6}$$

The equation of motion for the top waveguide is finally derived through the combination of equations (4.21) and (5.6):

$$\rho\frac{\partial^2 w_1(x,t)}{\partial t^2} - E\frac{\partial^2 w_1(x,t)}{\partial x^2} - g(x) * w_1(x) - l(x) * w_2(x) = 0 \tag{5.7}$$

With analogous procedure, the equation of motion of the bottom waveguide is:

$$\rho\frac{\partial^2 w_2(x,t)}{\partial t^2} - E\frac{\partial^2 w_2(x,t)}{\partial x^2} - g(x) * w_2(x) - l(x) * w_1(x) = 0 \tag{5.8}$$

Note the term $l(x)$ contains the properties of the interacting structures and is the same for equations (5.7) and (5.8), since the two waveguides are identical, in this example. However, the chance of achieving complex coupled systems, with a possibly high number of components interacting with each other, lies in $l(x)$. Indeed, designing appropriately the shape of $l(x)$ means designing a specific long-range scheme, which changes accordingly. The long-range scheme affects the topology of the system and, consequently, it dominates the communication pattern.

5.2 Insights into the dispersion relationship

In this section, the analytical form of the dispersion relationships is determined on the base of the displacement, as expressed in equation (4.4). In particular, for

$w_1(x,t) = \varphi_1(x)e^{-j\omega t}$ and $w_2(x,t) = \varphi_2(x)e^{-j\omega t}$, the coupled equations are:

$$\begin{cases} -\rho_1\omega^2\Phi_1 + E_1k^2\Phi_1 - G_1\Phi_1 - L\Phi_2 = 0 \\ -\rho_2\omega^2\Phi_2 + E_2k^2\Phi_2 - G_2\Phi_2 - L\Phi_1 = 0 \end{cases} \tag{5.9}$$

What is observed is that this new type of coupling introduces an additional convolution term in the dispersion relationship, which is of the same nature of the contribution of the local interactions. Even this case discloses the chance to obtain an analytical solution. In fact, if G_1, G_2 and L are known Fourier transforms, the previous equation exhibits an analytical dependence between the frequency ω and the wavenumber k. The general result confirms the chance of an infinite number of propagating modes, since the nature of the dispersion relationship can admit infinite numerable solutions. The global dispersion relationship can be obtained by isolating Φ_2 from the second equation of (5.9):

$$\Phi_2 = \frac{L}{-\rho_2\omega^2 + E_2k^2 - G_2}\Phi_1 \tag{5.10}$$

that substituted into the first, provides:

$$\left(-\rho_1\omega^2 + E_1k^2 - G_1\right)\Phi_1 - \frac{L^2}{-\rho_2\omega^2 + E_2k^2 - G_2}\Phi_1 = 0 \tag{5.11}$$

The resulting dispersion relationship is:

$$\left(-\rho_1\omega^2 + E_1k^2 - G_1\right)\left(-\rho_2\omega^2 + E_2k^2 - G_2\right) - L^2 = 0 \tag{5.12}$$

Selecting once again the particular case of a Gauss-like interaction $f(r) = \mu r e^{-\left(\frac{r}{\beta}\right)^2}$ and assuming the two waveguides are twins, the dispersion relationship becomes:

$$\left(-\rho\omega^2 + E\,k^2 - G\right)^2 - L^2 = 0 \tag{5.13}$$

As for the single waveguide system, nondimensional parameters are introduced to more conveniently discuss the problem: $\Omega = \sqrt{\frac{\rho}{E}}\beta\omega$, $K = \beta k$, $\Delta = \frac{D}{\beta}$ and $\chi = \frac{\mu\beta^3}{2\sqrt{2}E}$, which represents a measure of the intensity of those forces expressed in terms of elastic modulus. As previously stated, being E^* either positive or negative, χ as well can perform both signs, meaning an attractive action when positive ($\chi > 0$) and repulsive when negative ($\chi < 0$). In this way, the effects produced by the long-range forces can be discussed in terms of the parameter χ only. The displacement of the two waveguides is assumed to be function of the same wavenumber, since they are identical with each other. This allows to obtain a system of equations analogous to (5.9):

$$\begin{cases} \Omega_1 = \pm\sqrt{K^2 - \chi K^2 e^{-\Delta^2 - \frac{K^2}{4}} - \chi K^2 e^{-\frac{K^2}{4}}} \\ \Omega_2 = \pm\sqrt{K^2 - \chi K^2 e^{-\Delta^2 - \frac{K^2}{4}} + \chi K^2 e^{-\frac{K^2}{4}}} \end{cases} \tag{5.14}$$

As for the single waveguide, the dispersion relationship is examined as varying with respect to the parameter χ.
Figure 5.2 and 5.3 show the trend of the nondimensional dispersion relationship for $\chi = -50$ and $\chi = 50$, respectively, with respect to the conventional D'Alembert waveguide. A unique curve, one for each solution of Ω, describes the behaviour of the entire system, since the two rods are identical and a single equation contains both the intra-body and the inter-body long-range interaction contributions. The mutual distance between the waveguides is set to $\Delta = 0.1$ and both the positive solutions of Ω are displayed.
For both values of χ, one solution, namely Ω_1, produces interesting effects. When

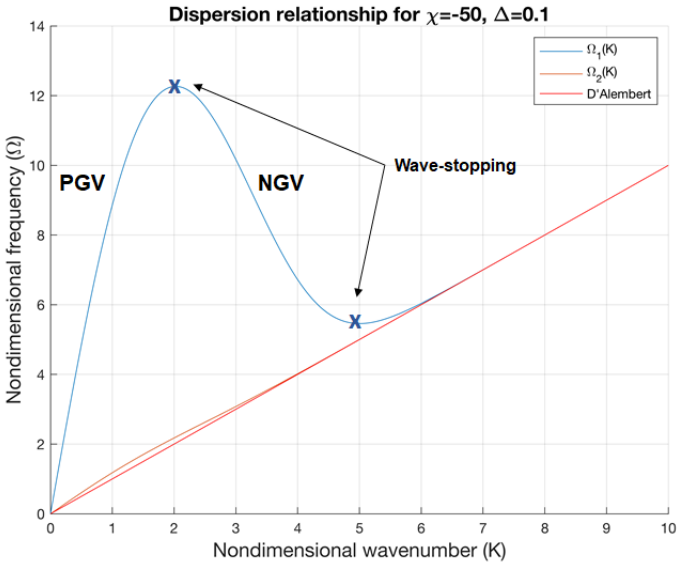

Figure 5.2. Dispersion curve for negative χ

the parameter χ is positive, a region of no propagation appears for low values of the nondimensional wavenumber K. Indeed, for such values of K, only complex values of Ω_1 are obtained. With no chance to damp the divergent contribution of the solution, the system is subdued to instability. A steep slope closes the unstable band and unveils a narrow wavenumber region in which the group velocity tends to infinite and superluminal propagation arises, before the system converges to the D'Alembert model. For negative values of χ, the curve has both a maximum and a minimum, at which the group velocity vanishes. This means that for positive χ the existence of a wave-stopping region is proved. Furthermore, while the positive slope implies conventional propagation, the negative slope reveals negative group velocity. On the other hand, the solution related to Ω_2 does not show remarkable effects. This is due to the destructive combination in the solution between the two long-range contributions, the one related to the intra-body interactions and the one provided by the magnetic coupling, which causes the annihilation of the long-range effect.

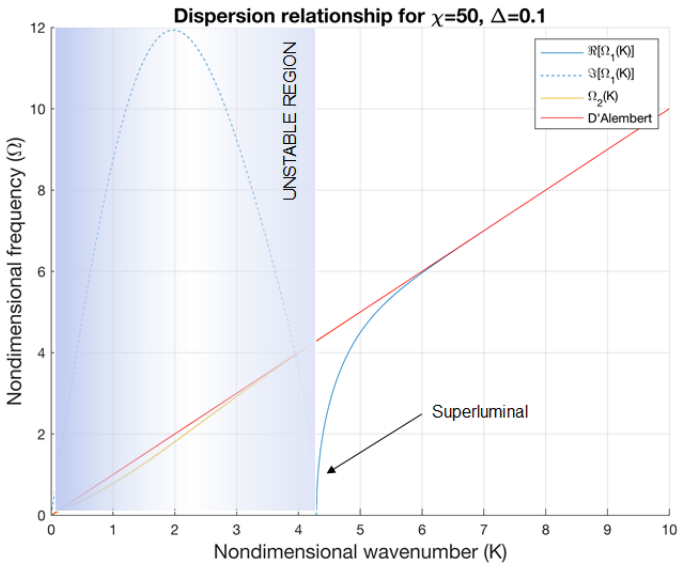

Figure 5.3. Dispersion curve for positive χ

5.3 Numerical simulations and remarkable properties of the twin-waves

The *twin-system* is investigated as extension of the single waveguide problem with the idea to extract how the intrinsic properties of the long-range interactions enable the communication between far systems and modify the overall dynamic response. The results are performed in two separate ways: the first provides numerical simulations of the discrete counterpart of the twin-system, the second one are visualizations of the wave propagation in space and time.
The behaviour of the twin waveguides has been numerically analysed by considering their discrete counterpart. With 200 degrees of freedom, the system consists of a set of two discrete subsystems of uniform masses, each one connected with springs to its first neighbours. The long-range interaction not only links masses of the same waveguide, but also the two waveguides together. The distance D between the waveguides is considered in terms of the typical long-range interaction length $\delta_0 = \beta$. Numerical simulations are performed for a distance of the same order of δ_0, $D \sim \delta_0$.

To perform numerical simulations, an initial non-zero displacement has been applied only to the top waveguide (*waveguide 1*), leaving at rest the second (*waveguide 2*). The main noticeable effect is an induced wave propagation in the bottom waveguide, clearly only due to the propagation on the top one. This confirms what analytically observed: the pair of waveguides is intrinsically coupled, and propagating phenomena occurring in one of them will be transmitted to the other by the mean of long-range forces. A second remarkable effect is the richer wavenumber content of the twin waveguides compared with the purely elastic one. Some dispersion is observed even when the initial wave train packet travels along the classical waveguide. Since the theoretical system represented by the standard waveguide

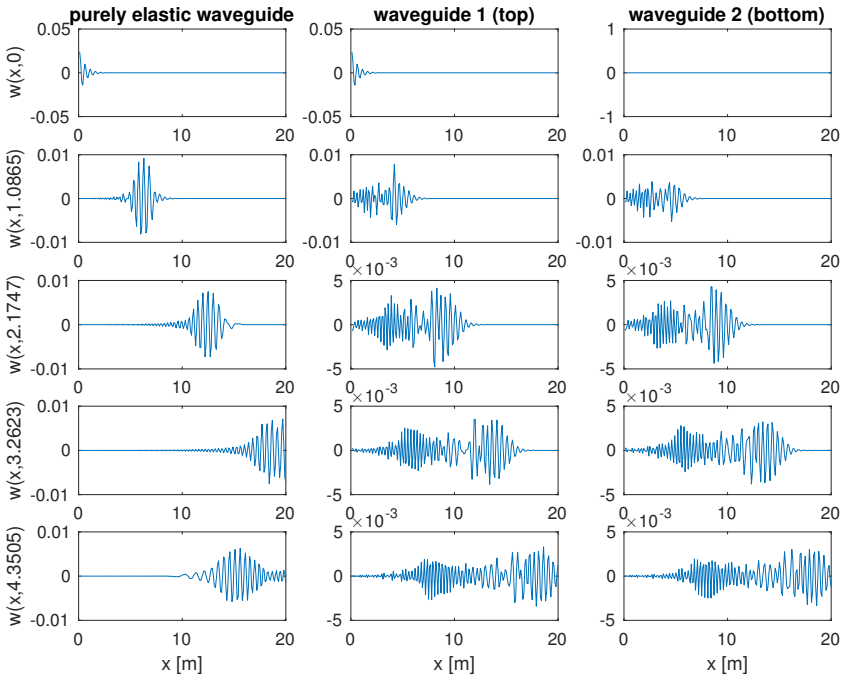

Figure 5.4. Twin waves vs purely elastical simulations

$E\dfrac{\partial^2 w}{\partial x^2} - \rho\dfrac{\partial^2 w}{\partial t^2} = 0$ is non-dispersive, the weak dispersion documented in Figure 5.4 (left column) is due to the numerical discretization (a finite difference scheme is used) as it is known from the theory of finite difference equations. In fact, the dispersion relationship is in this case nonlinear, but represented by a branch of sine, implying higher frequencies propagate slightly slower. The wavenumber content of the twin waveguides is clearly richer with respect to the classical waveguide, and the initial wave packet spreads over the waveguide length. This effect is explained by equation (4.36), as a consequence of the infinite solutions of the dispersion relationship 4.29, or equivalently 5.13, predicting the appearance of a superposition of propagation modes, the evidence of which is in the second and third column of Figure 5.4. Moreover, it appears a slow down of the wavefront speed in the presence of long-range interaction.

To perform space-time visualization, the discrete counterpart of the displacement (4.4) is considered:

$$w(x,t) = \sum_{i}^{N} \left[W_i^{(1)} \sin\left(k_i x - \omega\left(k_i\right) t\right) + W_i^{(2)} \cos\left(k_i x - \omega\left(k_i\right) t\right) \right] \tag{5.15}$$

where $W_i^{(1)}$ and $W_i^{(2)}$ are coefficients depending on the initial conditions, and $\omega\left(k_i\right)$ is defined by the considered dispersion relationship, whether it is related to a Gauss-like or Laplace-like force, as done for the single waveguide.
The results are shown in terms of χ, as already presented in section 4.4. The analysis of phase and group velocity unveils new propagating phenomena that are defined as *hypersonic propagation*, *wave-stopping* and *negative group velocity propagation*.

To conclude the investigation, space-time visualization are presented in Figure 5.5, in which the history line of the displacement in both waveguides is displayed.

According to Figure 5.2, at low wavenumbers (see Figure 5.5), both phase and

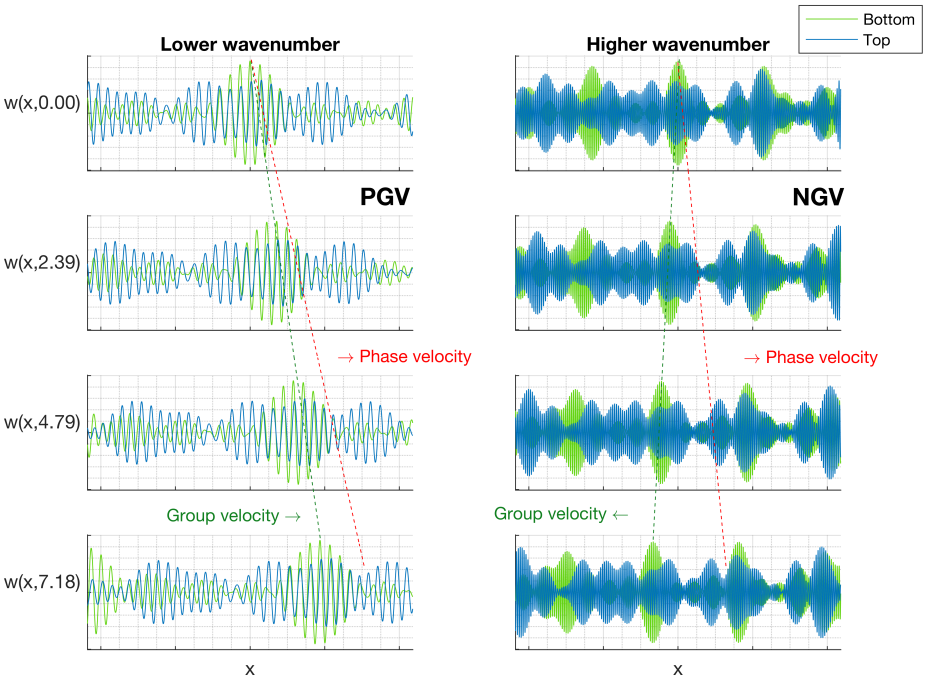

Figure 5.5. Space-time visualization

group velocity are positive. However, the increase of the wavenumber induces a changing in the group velocity, which becomes negative and discordant with respect to the phase velocity.

Finally, a propagation map is presented in Figure 5.6. It shows different propagating scenarios, occurring at the varying of the parameter χ, according with the effects discussed for the dispersion curves. Because of the previously explained reasons, the map is given for Ω_1 only. Each line is an isofrequency contour. The instability region is surrounded by the superluminal propagation region; the negative group velocity is delimited by the conventional propagation regimes.

5.4 3D model

The experimental campaign has been carried out at Technion, Israel Institute of Technology and has its core in the analysis of the twin-system, composed by two identical rod-like structures. Each waveguide has magnetic dipoles embedded within, which are responsible of the cross interaction (*inter-body interactions*), since no structural connection is included between the waveguides.

The aim of any experimental campaign is to validate the presented theoretical model or a proper general theory. In this second part of the chapter, it is presented what

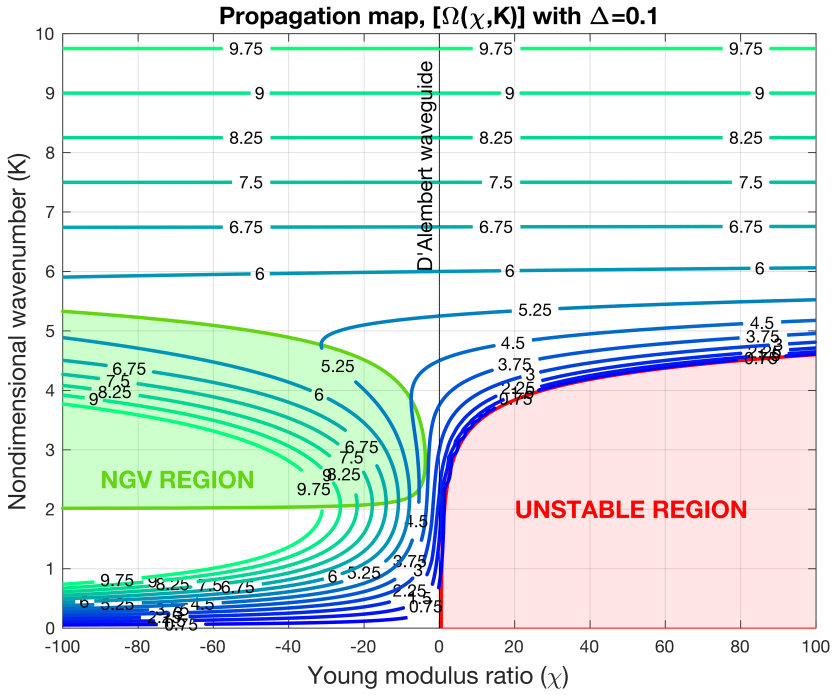

Figure 5.6. Propagation map

could be defined as an initial experiment. The presented theory has a very general feature; however, the fact that results are presented in a nondimensional form implies the lack of references for the physical properties of the system. Thus, the aim of this first-stage experiment is to obtain a measure, an estimation of the physical parameters able to perform, not only strong enough long-range interactions, but also the propagation phenomena previously described. The number of variables and unknowns of the system, which interprets the discrete counterpart of the twin-wave system, is undoubtedly large: minimum number of degrees of freedom, value of the mass, type of connection between masses, number of magnets, source of long-range interaction, type and strength of the magnets. The complexity of the problem stands not only in the fact that the model is applied on infinite waveguides, which is a condition that must be reproduced, but also because the long-range interactions spread within the single waveguide, and further connected the two waveguides. This implies that each mass is affected by a complex network of connections if the magnets are powerful enough. For these reasons the experimental campaign has been carried out on the twin-system, but the arrangement of magnets is such that only inter-body interactions have a major contribution, so to slightly reduce the order of complexity of the problem and thus, of the unknowns. Moreover, the choice to perform the experimental campaign on the twin system stands in the fact that, even though useful from a mathematical point of view, the nondimensional characteristics of the obtained results are a limitation when an experimental set-up must be organised. The twin-system responds to the need of coupling as many degrees of freedom as possible: the coupling power of the magnets is an unknown;

this implies that also the number of coupled degrees of freedom for each magnet is unknown; working with coupled waveguides means taking advantage of the range of action in an additional dimension, transverse with respect to the longitudinal motion. Coupling in this direction is clearly unavoidable, but the FEM analysis explains whether the motion in the two directions is actually coupled or not and if there are range of frequencies for which it is admissible to consider the motions fundamentally uncoupled.
For sake of simplicity, the experimental model is composed by a set of degrees of freedom, arranged so to recreate two discrete waveguides, where the main one is the one the force is applied to. Magnets have been selected to produce the long-range interactions and for this reason each mass is designed so to host a magnet. The idea is to generate a lumped element model, as shown in Figure 5.7, in which each element is representative of a single physical property.
Each mass is connected with each other through elastic springs and further con-

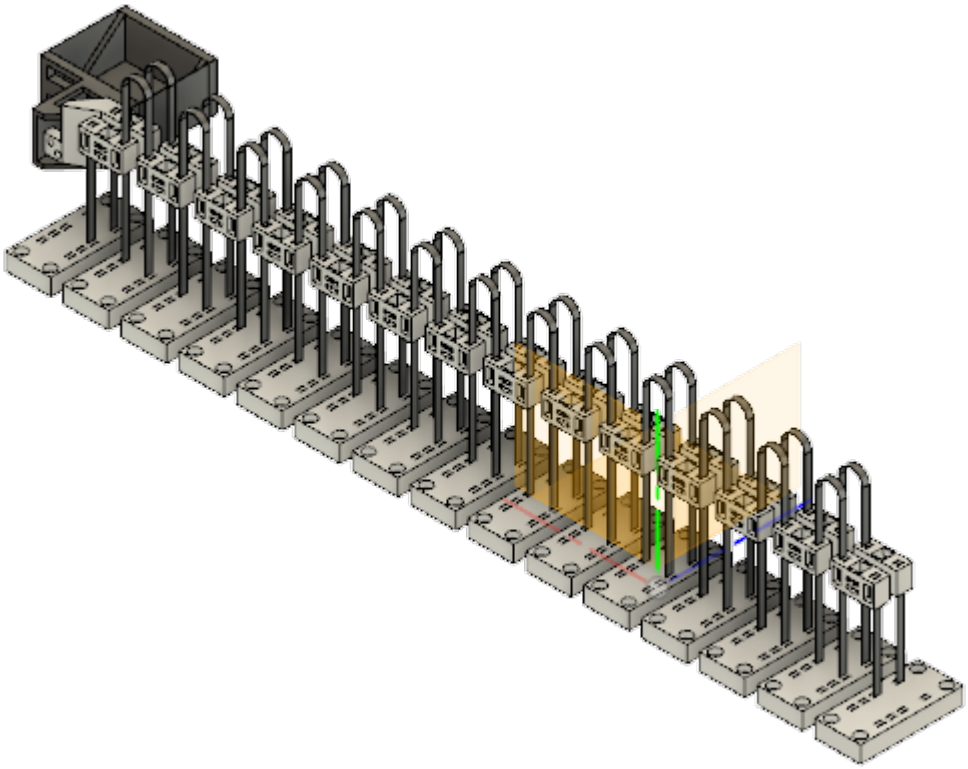

Figure 5.7. 3D model

nected to the basement, through ground-hook springs. The length of the springs is designed in order to be much stiffer in the transverse motion than in the longitudinal one, so to endorse the propagation of longitudinal waves, according to the presented mathematical model. In addition to the magnet holders and the springs, the system includes also a set of basis, bolted to the optical table, which have the function to connect the masses to the optical table and to adjust the distance of the second waveguide with respect to the main one at three possible locations, i.e. a

face-to-face distance of 10 mm, 20 mm or 30 mm. From an executive point of view, the springs are thought as a unique piece: a pre-stress is imposed so to force the wanted radius of curvature, then the free ends of the strips pass through the holes in the magnet holder and then they are glued in the base holes, corresponding to the chosen distance between the waveguides. The holes of the magnet holder have an inner profile designed so to compress the spring and to prevent the sliding of the magnet holder along the strip. The dimensions and the number of the masses are the result of the set-up constraints and the maximum allowed displacement. Indeed, to guarantee a longitudinal overall displacement of the masses of 6 mm ($\pm$3 mm), the mutual distance between the masses is set at 12,6 mm. The length of the optical table (about 910 mm) and the willingness to include as many degrees of freedom as possible, considering also the dimensions of the excitation system, set the maximum number of masses at fourteen per waveguide. Figure 5.8 shows the global arrangement.

The components have been designed with Autodesk Fusion 360 software and

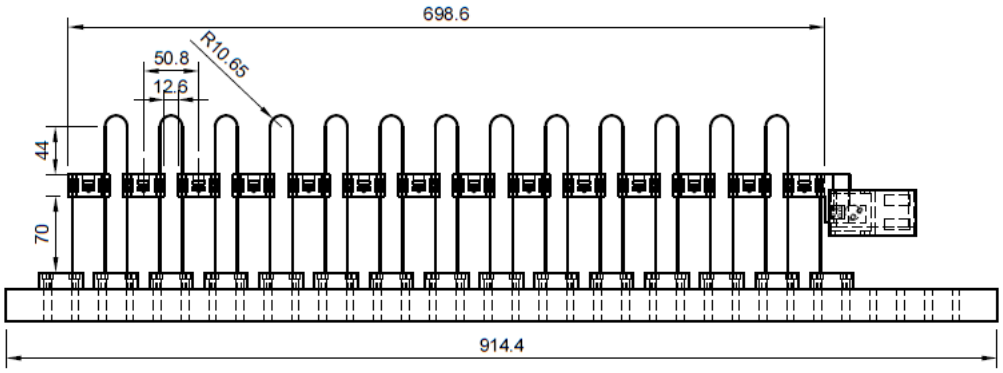

Figure 5.8. Global drawing

realized with a 3D printer. Figure 5.9 and Figure 5.10 show for the magnet holder and the base, both the 3D model and the drawing, in which the dimensions are in mm, respectively.

5.5 Finite element analysis

To carry out a FEM analysis, the three-dimensional model has been imported in Ansys Workbench software.

Even though the complexity of the system is not extreme, the geometry has been simplified, deleting the objects that would impose a fine mesh, causing a high computational cost, with no advantage in the preciseness of the results since these details hardly affect the dynamics: the holes in the basis and in the magnet holders have thus been deleted. Carefulness should be used for the strips: first of all in the original model they pass through the magnet holders and are inserted in the

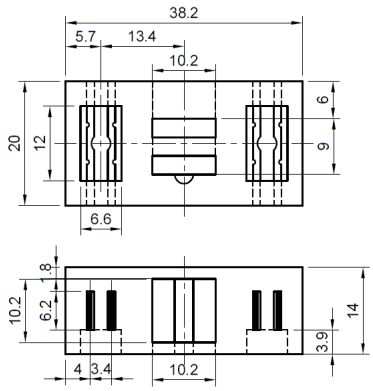

(a) Drawing

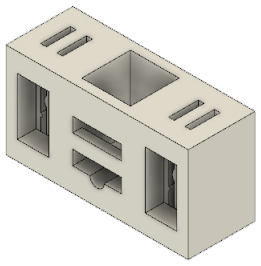

(b) 3D model

Figure 5.9. Magnet holder

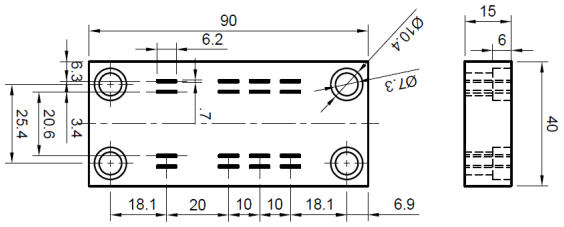

(a) Drawing

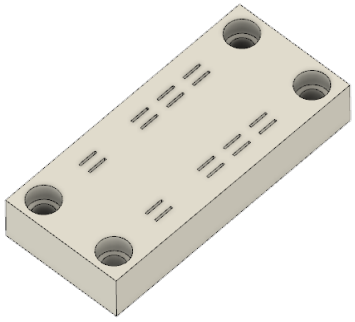

(b) 3D model

Figure 5.10. Base

basis, which implies that, after deleting the holes, to avoid interference the strips must be cut; besides, any thin object is better modelled as a surface element, by replacing the object itself with its own middle surface; the real thickness of 0.5 mm is automatically recognised. Eventually the strips would not appear in the model as solid basis any longer, but as surfaces. Since the entity body does not exist any more, it is necessary to recreate the connections between the strips and the magnet holders on one side and the basis on the other. The type of connection uses a Multiple Point

Table 5.1. Material properties

	Structural Steel	PLA
Elastic modulus E	210 GPa	3.5 GPa
Density ρ	7980 $\frac{kg}{m^3}$	1234 $\frac{kg}{m^3}$
Poisson modulus ν	0.3	0.36

Constraint (MPC) formulation, which lock the rotation of the strip, enabling the deformation of the strip itself. Other types of formulation would instead allow a free body motion; this means that the strip would not deform, but simply rotate around its longitudinal axis.
The used materials are structural steel for the springs and PLA, used by the 3D printer, for the basis and the magnet holders. Table 5.1 reports the material properties. Literature usually provides a value of PLA density around $1240\frac{kg}{m^3}$. However, the components are not fully printed; indeed, a section of each component would unveil a netting pattern with a thread thickness of $0.15mm$. To obtain an accurate estimation, the density has been measured as the ratio between the measured masses, of the magnet holder and the base, and their volumes, provided by Ansys. Hence, the density if the magnet holder is $\rho_{PLA} = \frac{8.5}{9447.5}\frac{gr}{mm^3} = 899.71\frac{kg}{m^3}$, while the base has $\rho_{PLA} = \frac{28.92}{54000}\frac{gr}{mm^3} = 552.2\frac{kg}{m^3}$.
To obtain an appropriate fine mesh, as shown in Figure 5.11, hex dominant elements have been selected for the solid bodies, as magnet holders and basis, and square plane elements, quadrilateral dominants, for the strips. A size mesh of $2mm$ is applied.
Once the mesh is generated, to obtained the harmonic response, more than the

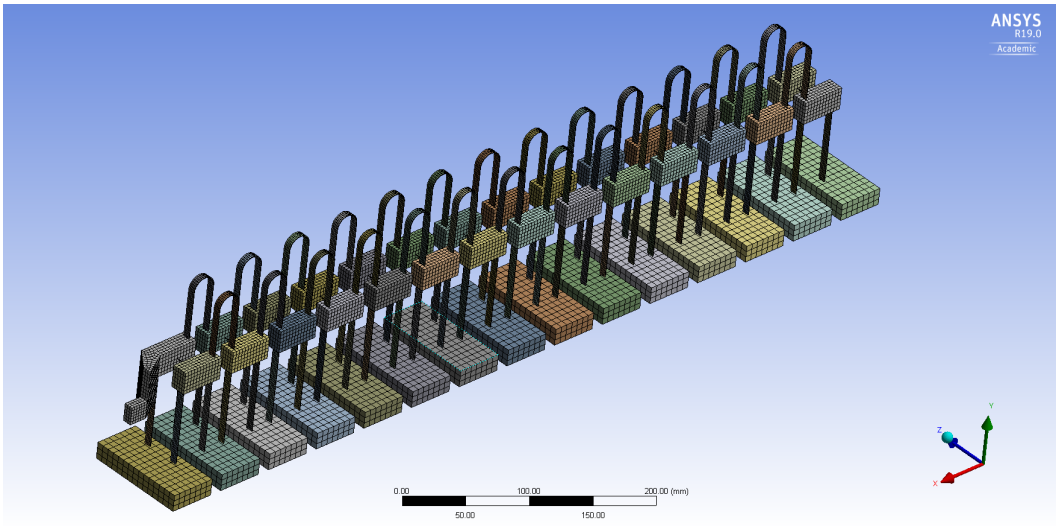

Figure 5.11. Model mesh

modal analysis, fix boundary conditions have been applied on the lower face of

the basis, corresponding to the connection to the optical table, and a punctual longitudinal force is applied to the first degree of freedom, simulating the voice coil excitation.
To model the magnetic interaction, physical elements can be added between the two waveguides. As previously mentioned, the long-range interaction occurs only between the waveguides, and the effect within the single one can be neglected. As first stage, beam elements have been added only between pairs of masses, arranged one in front of the other, avoiding the extension of the connection to the second order, as shown in Figure 5.2 in which the beam elements are encircled in green.
Beams are preferred to springs as the latter take into account only the longitudinal

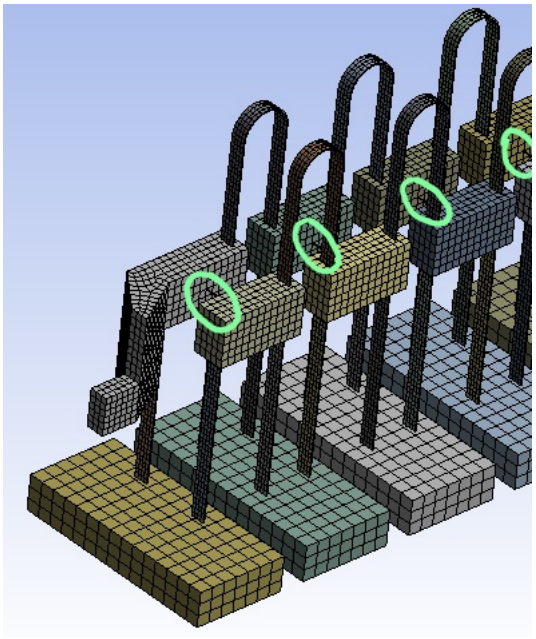

Figure 5.12. Detail of the beam element

motion and are reliable only under the assumption of small displacements. Beams provide also the advantage to access the cross-section geometry, which can be adjusted so to recover the magnetic equivalent stiffness.
In order to add the beam elements, the geometry must be modified in the pace Claim environment. Rectangular profile is chosen for the cross-section. Through the values of b and h of the cross-section, it is possible to reproduce the values of the magnetic stiffness k_x and k_y in the two on-plane directions, x and y, respectively. Since k_x and k_y are coupled with each other through b and h, the system that correlates b, h, k_x and k_y does not necessarily have a solution. Indeed, $k_x = \frac{EI}{L^3}$, $k_y = \frac{EA}{L^3}$, where $A = bh$, $I = \frac{bh^3}{12}$ and L is the face-to-face distance. However, given the fact that the longitudinal motion is the favoured one, the choice of b and h is such that priority would be given to the value of k_x; k_y is evaluated consequently. The values of the effective stiffness k_x and k_y are calculated considering the linearised expression of the magnetic force, which has been measured through the calibration

Table 5.2. Modes

1	28.771 Hz	2	36.606 Hz	3	36.765 Hz	4	37.247 Hz
5	37.74Hz	6	38.514 Hz	7	39.48 Hz	8	40.409 Hz
9	41.826 Hz	10	42.806 Hz	11	44.588 Hz	12	45.546 Hz
13	47.583 Hz	14	48.466 Hz	15	50.645 Hz	16	51.416 Hz
17	53.628 Hz	18	54.262 Hz	19	56.399 Hz	20	56.885 Hz
21	58.841 Hz	22	59.182 Hz	23	60.854 Hz	24	61.066 Hz
25	62.35 Hz	26	62.469 Hz	27	63.264 Hz	28	63.343 Hz
29	127.98 Hz	30	152.37 Hz				

procedure of the magnets.
The magnetic force, experimentally evaluated by measuring the strength occurring between two magnets at different distances, is:

$$F_M = C_1 + C_2 \frac{1}{x^4} \tag{5.16}$$

with $C_1 = 7.45[N]$ and $C_2 = 1.2610^5[N * m^4]$. To obtain the values of the stiffness, the magnetic force must be linearised according to equation (3.24). The resulting values (see Appendix E) are $k_x = 4.92 \frac{N}{m}$ and $k_y = 16.9 \frac{N}{m}$. From the value of k_x, $b = 0.05\,mm$ and $h = 0.47\,mm$ are extrapolated. They lead to a larger value of k_y, but it is still reasonable, as it implies the system is stiffer in the transverse motion; in fact, the transverse motion appears at higher frequencies.
Eventually, a number of thirty modes is analysed over a range of frequency from 0 Hz up to 200 Hz, and the frequencies at which they occur is reported in Table 5.2. The range of frequency must be decided accurately, because to evaluate the harmonic response of a system, the contributions of all modes must be taken into account. A good estimation for the frequency range is 1.5 times higher than the natural frequency of the last considered mode.
The results show two specific frequency bandwidths in which several modes are gathered together. Besides, to notice is the fact that modes appear coupled: at very close frequencies, it emerges first the mode of the second waveguide and straight after the mode of the main waveguide. An example is provided by Figure 5.13 and Figure 5.14, which show the second mode.
A first group of modes occur between 28 Hz and 60 Hz. These modes refer all to the longitudinal motion of the system, with negligible displacements on the other directions. The following figures, which exhibit the non-real scale deformation of the system, reveal the most representative modes that refer to 38.514 Hz (Figure 5.15), 48.466 Hz (Figure 5.16) and 51.416 Hz (Figure 5.17). A more complete list of them is provided in Appendix F.
A second bandwidth appears approximately between 125 Hz and 155 Hz. Figure 5.18 shows the mode corresponding to 152.37 Hz, presenting both the isometric and the top view, which represents an example of the transverse modes occurring in this frequency bandwidth.
This is sufficient to assume that the longitudinal and the transverse motions are substantially uncoupled and thus to focus on the lower frequency bandwidth during

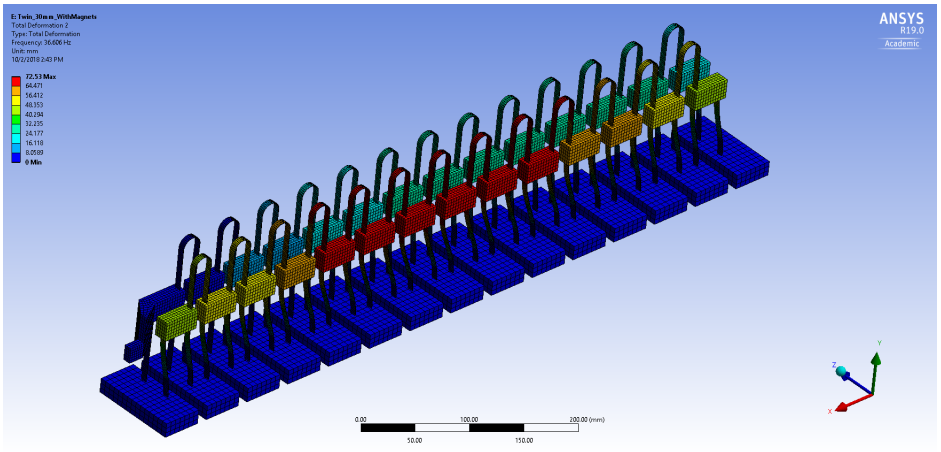

Figure 5.13. 36.606 Hz

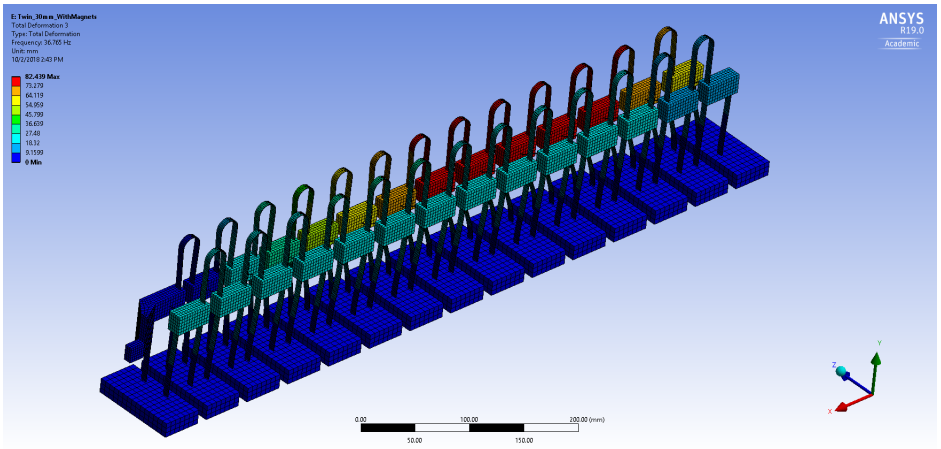

Figure 5.14. 36.765 Hz

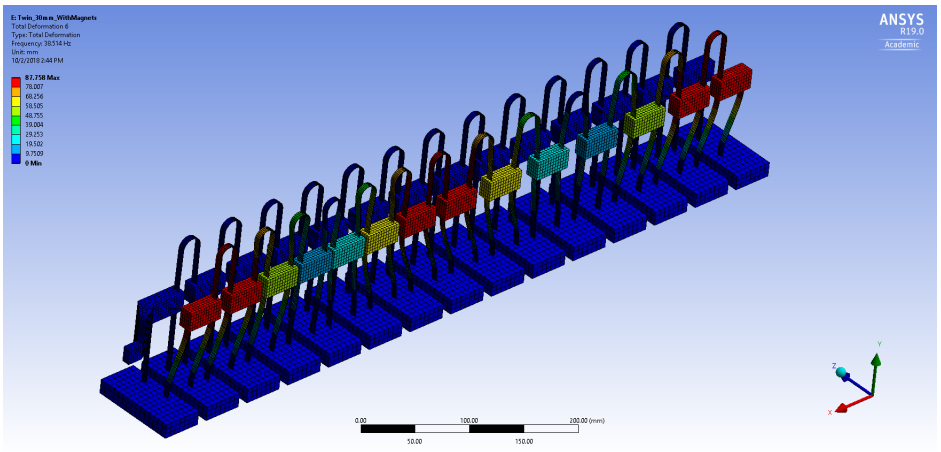

Figure 5.15. 38.514 Hz

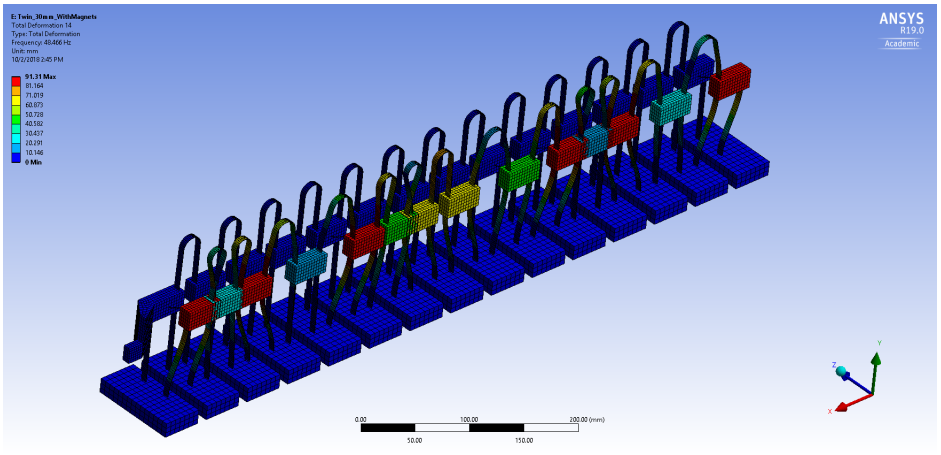

Figure 5.16. 48.466 Hz

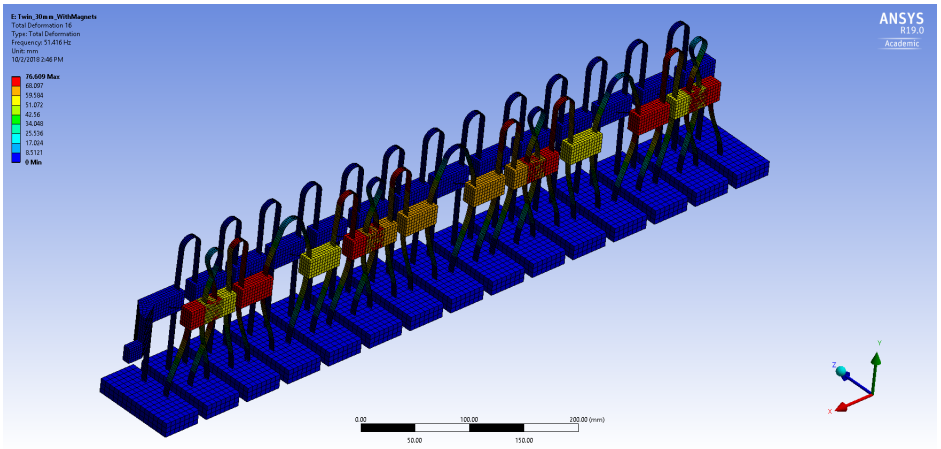

Figure 5.17. 51.416 Hz

the experimental campaign.

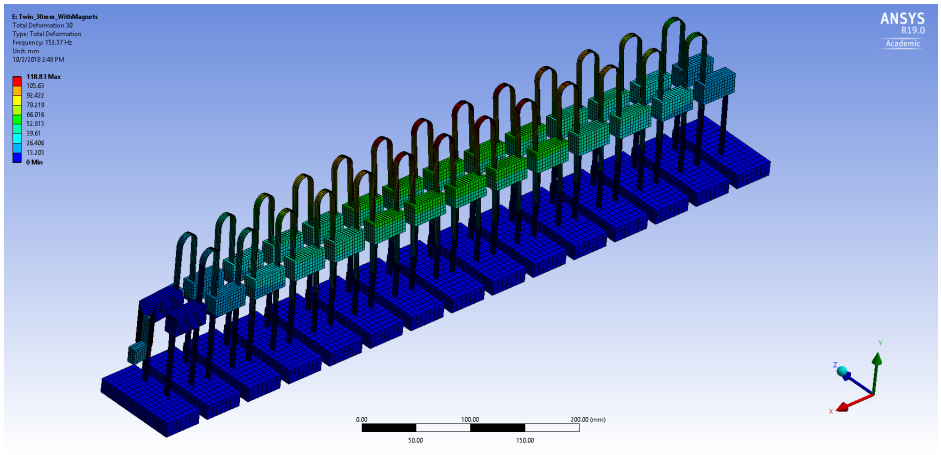

(a) Isometric view

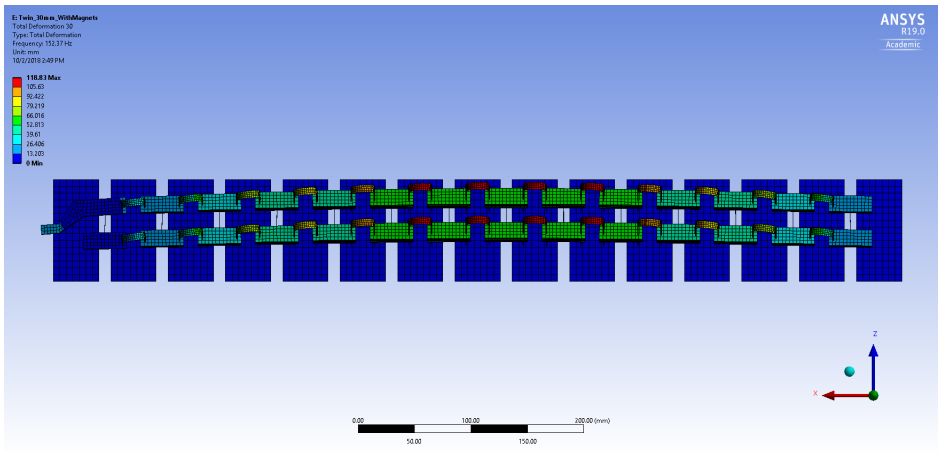

(b) Top view

Figure 5.18. 152.37 Hz

5.6 Experimental setup

The experimental set-up is composed by the twin-wave systems, the sensors and the equipment necessary to excite the system. Figure 5.19 shows the set-up chain and indicates in blue the path followed by the input signal and in black the output signal.

The masses and the basis have been 3D printed using PLA material. The basis are bolted on the optical table, which ensures the correct positioning and the stability of the structure. Metallic strip behave as both ground-hook springs and they further connect the mass with each other. To perform a longitudinal motion and to easily link the masses, the springs have been bended and the assembly considers the springs to be bended before they are inserted in the magnet holders. At last their free ends are glued on the basis. Each mass hosts a magnet and magnets are arranged so to produce only inter-body interactions, as the North-South position is such that their effect rapidly vanishes along the waveguide they belong to, but it is stronger in the transverse direction, i.e. they are attractive between the waveguides

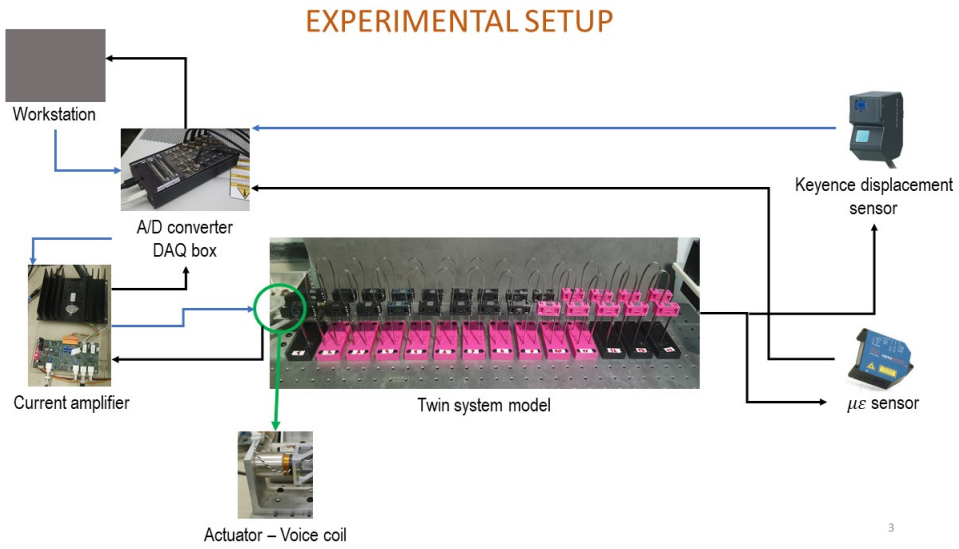

Figure 5.19. Experimental set-up

and repulsive within the same waveguide. The strength of the magnets is such that the related parameter χ is in the range between -1 and 1. This means that, among all the analysed propagation phenomena, the expected one is the *mode migration*. Anticipating what later will be discussed, the post-processing investigation must consider this aspect and an input force allowing an accurate modal analysis is preferable. The first mass of the behind waveguide is connected to the voice coil actuator, and from now on it is referred to this wavegudie as "main" waveguide.
The voice coil actuator provides the excitation onto the longitudinal direction. The excitation is imposed in terms of the current supplied to the actuator: if an harmonic force is desired, to be harmonic is actually the current and theoretically the resulting force is proportional to the current: $F = \alpha I$; however, the real force is:

$$F = \alpha I + \varepsilon I^3 \tag{5.17}$$

where the additional term, even though small, brings distortions in the input signal and further frequency contributions, which are not necessarily negligible. The voice coil support, as shown in Figure 5.20, is composed by a basement and two nonlinear springs and during the evaluation of the measurements, the dynamics of this system must be considered.
The input signal is generated by the workstation, then sent to the A/D converter, which also receives the output signal on a different channel. The sampling range of the digital converter can be decided depending on the amplitude of the output signal. For instance, if the amplitude is around 9V, the sampling range should be $[-10V; +10V]$; for an output signal of 0.5V, the sampling range should be reduced to $[-2V; 2V]$. Since the number of used bits is the same, it is preferable to use a as small as possible sampling range, so to increase the resolution. Before reaching the actuator, the input signal is sent to the current amplifier, which has its internal feedback control with a gain to correct the current. The current amplifier is also connected to its power supply system. Three laser sensors, two Keyence and

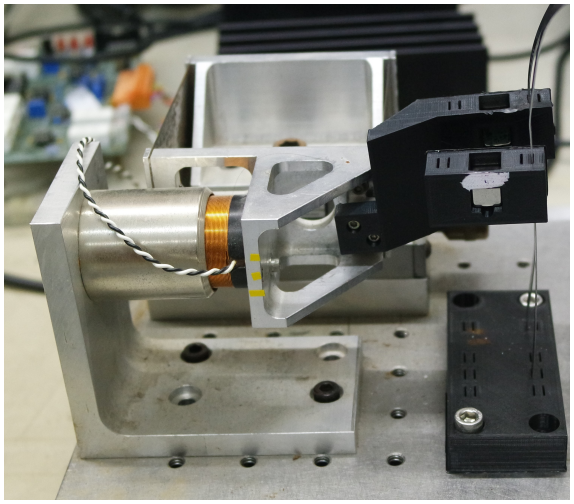

Figure 5.20. Voice coil support

one $\mu\varepsilon$, are used to read the displacement of one mass each. Each sensor has its own power supply. Laser sensors are used as the non-contact principle enables wear-free measurements since the sensors are not subject to any physical contact with the target. Furthermore, the laser triangulation principle is ideal for very fast measurements with high accuracy and resolution. Laser triangulation sensors operate with a laser diode which projects a visible light spot onto the surface of the measurement target. The light reflected from the spot is imaged by an optical receiving system onto a position-sensitive element. If the light spot changes its position, this change is imaged on the receiving element and evaluated. The three sensors are all red semiconductor lasers, with a reference distance of measurements of 50 mm. The dimensions are rather similar: 75 mm x 70 mm x 33 mm for the Keyence and 48 mm x 65 mm x 20 mm for the $\mu\varepsilon$, and similar is also their weight of approximately 100 gr. Since all these sensors have a specific reference distance, they need to be calibrated before the measurements are taken. Besides, they must be mounted on a support which can adjust the position of the laser, so to be at the right distance from the target. Keyence lasers are slightly more sensitive, since the dimensions of the spot are $50\mu m$ x $2\mu m$, while the $\mu\varepsilon$ has a diameter spot of $110\mu m$. The measuring range of the Keyence is ± 10 mm, more extended is the one of the $\mu\varepsilon$: 50 mm overall.
A Sony RX10iv camera, which records the motion of the entire twin-wave system for four seconds, with a sampling rate of 960 frame per second, completes the set-up. The unit of measurements of the displacement provided by the camera is the pixel. Two considerations follow: first of all, a conversion from pixel to mm is required; this is not straightforward as also the curvature of the lenses and the zoom have distortion effects on the image. This distortion causes a non direct proportionality between a length in an image and the real length. For this reason, a calibration process is required before the run of the experiment and it has to be repeated any time the position of the camera changes with respect to the framed object. This is done by taking several picture of the set-up from always different point of views. A chessboard image is placed close to the twin-system, as shown in Figure 5.21:

the dimensions of the chessboard are known both in pixels and in mm; from the comparison between the dimensions and the displacement of the masses and the chessboard, it is possible to translate the sizes from pixels to mm. Secondly it must be noticed that a pixel is also the resolution of the camera, and if the amplitude of the displacement is smaller than a pixel, numerical errors might occur. In order to recover the displacement of the masses, the sub-pixel interpolation is used: through the values of the displacement calculated for points corresponding to the pixels, it applies a proper curve fitting so to rebuild the signal of the masses for all those points that do not correspond to the pixel grid. This ensures that the displacement can be retraced even if its amplitude is smaller than a pixel.
Before start the data acquisition process, three operations are required:

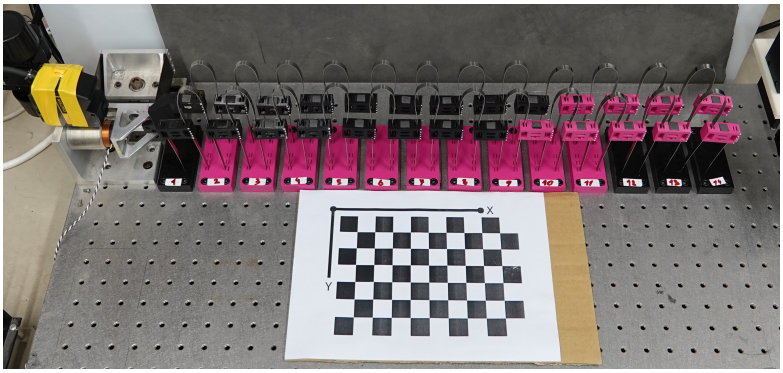

Figure 5.21. Camera calibration

- lasers warm up;
- lasers calibration;
- camera calibration.

The laser sensors calibration is aimed at recovering the offset in the input voltage, so to prevent the sensor to saturate in one of the directions, due to their rather small range, and to optimize the dynamic range on the A/D. The lasers have been positioned so to follow the three masses at the edge of the two waveguides, except for the first mass of the main waveguide, which is directly connected to the voice coil. This represent the only possible arrangement, otherwise the apparatus composed by the laser sensor and its support would screen the system from the camera.
The aim of the experimental campaign is to retrace the dispersion curve, so to be able to compare it with the theoretical findings. The most logical way to identify the dispersion curve is through the measure of the phase velocity at any frequency. Remembering that the phase velocity is given by the ratio between the displacement of the mass and the delay time, the identification of the dispersion curve is reduced to the evaluation of the delay time, through the cross-correlation of the signals outputs of different masses. For this purpose and, as previously mentioned, according to the type of the expected propagation phenomenon (*mode migration*), the choice of the excitation has to be accurate, in terms of the modal characteristics they introduce in the system. A perfect excitation should allow a frequency by

frequency analysis, thus should have a narrow spectrum in the frequency domain, similar to the one of a harmonic excitation, and narrow in space, so to involve the least number of degrees of freedom. This is an important aspect in the evaluation of the delay time. The measure of the delay time occurring between two masses is much more complicated if the propagation affects both of them. On this regard, the case of a sinusoidal excitation, hence a single harmonic, would not be correct, as its stationary feature would prevent the occurrence of a delay time; moreover, the unavoidable reflections impede actually a stationary motion. The application of a single period of a sinusoidal force is another incorrect excitation: indeed, the Fourier Transform considers the entire input history, and the truncation of the signal, necessary to cut the force and maintain only one period, is interpreted as a step, which translated in the frequency domain has a wide spectrum. In the same way, any "long-time" excitation would cause resonating phenomena, as the tilting of the masses, which would not occur for "short-time" excitations.
Table 5.3 specifies the types of applied excitations, which are later explained, and the investigated range of frequencies of these preliminary tests.

The Gauss pulse is probably the type of excitation that better responds to the

Table 5.3. Tests

Excitation	Type	To find	Frequency range	Analysis method
Gauss pulse	Transient	Dispersion curve	10-60 Hz 115-130 Hz	Correlation DIC
Step sine	Steady-state	FRF	10-60 Hz 115-130 Hz	Fitting sine DIC
Step response	Transient	FRF		DIC HT
Chirp Slow and fast	Transient	Dispersion curve	115-130 Hz 50 and 4 seconds	HT
HT:Hilbert	transform			

requirements imposed in space and frequency domains, and it provides a frequency by frequency scanning. Indeed, it is model so to have a 2 Hz frequency bandwidth spectrum and, consequently, it is applied every 2 Hz, covering the entire frequency range.
Both the step sine and the step response are used to calculate the frequency response. The step sine retraces the frequency response scanning one frequency at the time, and conveying the entire amount of energy in a single frequency. With step response is intended a square wave excitation, a wide spectrum input that involves all the frequency at the same time. Theoretically, the frequency response obtained with a square wave excitation, or any wide-spectrum excitation, and with a step sine should be the same. However, the step sine presents a better signal-to-noise ratio, due to the fact that exciting one frequency at the time, it forwards the energy onto a single specific frequency. The square wave instead, exciting all the frequencies at the same time, easily loses information about the frequencies which produce small responses. In a real system, there is no equi-distribution of the energy, which is not evenly spread over the spectrum. This implies the existence of frequencies more

energy-consuming than others. Eventually, the resulting frequency response is not the same, and the step sine is preferred.

5.7 Results and comparison

The analysis of the data involves two aspects and thus two methods have been chosen to evaluate the results: the Digital Image Correlation (DIC), which operates with the videos taken with the camera, is used to investigate the displacements of the degrees of freedom, so to recreate the dispersion curve; the Fit Sine, which analyses the data coming from the laser sensors, provides the frequency response of the system. Since the experimental campaign is only at its pilot stage, the practical limitations, which are further discussed in the next section, prevent the achievement of accurate results. However, these preliminary considerations are useful to enlighten the aspects that necessarily must be revised and enhanced for the future experiments. From this perspective only the most significant results, among many, are here reported.

As previously mentioned, the amplitude of the displacement depends on the frequency excitation, and while at low frequencies it can reach few mm, at high frequencies it reduces to few tenths of mm, thus it could even be smaller than a pixel. This usually provokes a loss of data; the sub-pixel interpolation instead, by curve-fitting the output data, is able to rebuild the signal, even in the absence of reference points.
This approach, defined within the major context of digital image correlation, provides a very precise measurement of the displacement of the selected points through the evaluation of the cross-correlation function, as additional step with respect to the pixel resolution method. Based on the fact that an image can be interpreted as a discrete frame (grid) composed by pixels, the pixel resolution provides only the values of the cross-correlation function corresponding to the pixel and rebuild the displacement starting from that information.
The basic approach of the pixel resolution, and also of the sub-pixel interpolation, which guarantees a higher grade of efficiency, considers a given an image of the system under analysis, and one of its possible smaller frame, selected so to follow the motion of the selected degree of freedom. The initial position, and hence the main frame, is considered as reference, and when the system moves, it does it with respect to the initial configuration. At each time, the new position is compared with the initial one, so to rebuild the displacement history line. This process is done step by step, considering the displacement in terms of pixels, which define the grid or mesh of the image. The displacement is evaluated through the cross-correlation function, which compares the moving frame, considered as a scaled delayed signal, and the initial configuration, i.e. the original signal. The cross-correlation function returns the exact delay time, as long as it has the chance to measure it everywhere. The pixel resolution, indeed, it is not sufficient when the maximum value of the function happens to be in between pixels, reason why, if a more exact estimation is needed, one has to use the sub-pixel interpolation.

The concept of correlation is associated to the grade of similarity between two variables, but it can be further extended to the case of two signals and whenever it is possible to find a law linking the two variables/signals, then it is allowed to talk about correlation and hence define a functional relationship.
There are several means to analyse the correlation rate, depending on the available data and on what it is required: the autocorrelation function, which provides a measure of the periodicity of a signal, is used when the same signal is interpreted as unique input, whose history line is considered and the signal is evaluated at different instants; the cross-correlation function, when applied to digital image processing, compares the frames, obtained by a single input but divided in multiple frames, as if different signals. Both functions are defined in the time domain. The autocorrelation function is used to identify deterministic periodic data hidden within external noise: while a deterministic signal has a correlation lasting in time, the correlation of a random signal, as noise, for long time intervals, decays to zero. The cross-correlation function measures the grade of similarity between two signals at different instants and it is defined by:

$$R_{xy}(t,\tau) = E\left[x(t) \cdot y(t+\tau)\right] \tag{5.18}$$

which simplifies into:

$$R_x(\tau) = \lim_{T\to+\infty} \frac{1}{T} \int_{-\frac{T}{2}}^{\frac{T}{2}} x(t) \cdot y(t+\tau)dt \tag{5.19}$$

for ergodic, time independent signals.
Cross-correlation is useful for determining the time delay between two signals, e.g. for determining time delays for the propagation of acoustic signals across a microphone array. After calculating the cross-correlation between the two signals, the maximum (or minimum if the signals are negatively correlated) of the cross-correlation function indicates the point in time where the signals are best aligned. The great power of the cross-correlation function is the chance to extract random data hidden within external noise, to provide a time delay estimation and also identifies the transmission ways, since each one produces its own time delay; this is possible since cross-correlation function shows a peak at the exact delay time:

$$t_d = \frac{d\gamma_{xy}(\tau)}{d\tau} = 0 \tag{5.20}$$

This is possible because the cross-correlation function slides the delayed function along the t-axis, calculating the integral of their product at each position. When the functions match, the value of cross-correlation is maximized, since when positive areas are aligned, they make a large contribution to the integral. So do the negative areas given the fact that the product of two negative areas is positive.

The sub-pixel interpolation has a precise methodology, which can be summarised in the following steps:

- evaluation of the cross-correlation for each frame;

- finding the maximum value of the correlation function and the corresponding indices through pixel resolution;
- definition of a sub-grid centred at the maximum pixel and composed by at least five neighbouring points;
- collection of the values of $\hat{\Gamma}_{xy}$ corresponding to the neighbouring points;
- curve fitting through least square method;
- differentiation;
- finding of the extrapolated position (x, y).

Let us consider the mathematical model behind this approach for a two-dimensional case, i.e. an image whose displacement occurs along two axes x and y.
The reference frame, the first level sub-frame, is a portion of a larger picture, defined by the function $g(x, y)$; the delayed frame, second level sub-frame, is a portion of the first level sub-frame, given by $f(x, y) = \alpha g(x + \Delta x, y + \Delta y)$. One could also consider directly the main picture as first level sub-frame, however, especially when a system is composed by a large number of degrees of freedom and when displacements are small, it might be more precise to select a window, first level sub-frame, including only the selected degree of freedom, and a further smaller frame, second level sub-frame, only around a portion of the mass, signed with markers. The markers are applied on the degrees of freedom that one wants to analyse and they are the points, whose displacement is then followed and whose purpose is to produce a better contrast with the surrounding objects in the image. This ensures that no ambiguity affects the measurements, since not only one can follow one degree of freedom per time, but also the selection of a narrow window around the markers ensures no ambiguity.
The normalised cross-correlation function can be calculated through:

$$\Gamma_{x,y}(\xi, \eta) = \frac{1}{\sigma_f \sigma_g} E\left[\left(f\left(x + \xi, y + \eta\right) - \mu_f\right)\left(g\left(x, y\right) - \mu_g\right)\right] \tag{5.21}$$

where σ_f and σ_g are standard deviations, i.e. $\sigma_x^2 = E[x^2] - E^2[x]$, μ_f and μ_g are means, which are all constants over time due to stationarity and $E[x]$ indicates the expected value.
Figure 5.22 shows the meaning of first-level frame, the green squared picture $g(x, y)$, whose initial position is the reference configuration, and second-level sub-frame $f(x, y) = \alpha g(x + \Delta x, y + \Delta y)$, i.e. the light-blue rounded sub-frame, which moves around with respect to the first one. This procedure is widely used since it increases the efficiency of the evaluation approach and prevent ambiguity when many degrees of freedom are involved, as it is possible to analyse the motion of different points separately.
Basically, the cross-correlation function $\hat{\Gamma}_{xy}$ is evaluated for each position of the second-level sub-frame.The pixel resolution, considering only the cross-correlation associated to pixels, returns the optimum pixel only, but not the exact value of the maximum of the cross-correlation, which might occur in between the pixels. When

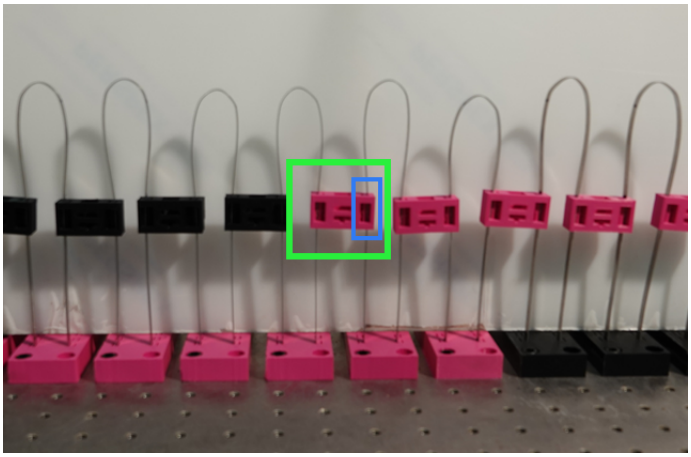

Figure 5.22. First and second level sub-frame

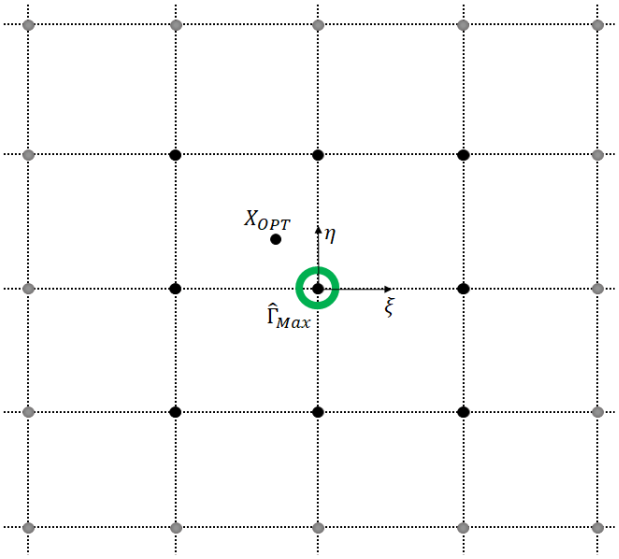

Figure 5.23. Neighbouring points grid

the maximum value of $\hat{\Gamma}_{xy}$ is detected through the pixel resolution, a grid of neighbouring point (pixels) around this maximum must be defined, as in Figure 5.23. The origin of the new reference system (ξ, η) is set at the maximum of the cross function and the neighbouring points are such that $i = -1, 0, 1$ and $j = -1, 0, 1$.
The values $\Gamma\left(\xi_{i,j}, \eta_{i,j}\right)$ of the cross-correlation function corresponding to the neighbouring pixels are known, since they have already been calculated so to find the maximum.

For image-processing applications in which the brightness of the image and template can vary due to lighting and exposure conditions, the images can be first normalized. This is typically done at every step by subtracting the mean and dividing by the standard deviation. The actual value of the cross-correlation function is

then:

$$\Gamma_{xy} = \frac{1}{\sigma_f \sigma_g} E\left[\left(f\left(x+\xi, y+\eta\right) - \mu_f\right)\left(g\left(x,y\right) - \mu_g\right)\right] \tag{5.22}$$

However, it is sufficient to evaluate the integral form defined over a finite interval and averages can be used instead of distributions. The expression of the approximated cross-correlation function is:

$$\hat{\Gamma}\left(\xi,\eta\right) = \frac{1}{\sigma_f \sigma_g} \int_{x_{min}}^{x_{max}} \int_{y_{min}}^{y_{max}} f\left(x+\xi, y+\eta\right) g\left(x,y\right) dxdy \tag{5.23}$$

Eventually, this expression is further approximated, considering the discrete counterpart, which is in wide sense stationary:

$$\hat{\Gamma}_{i,j} = \frac{\sum_m \sum_n \left(f_{i+m,j+n} - \mu_f\right)\left(g_{m,n} - \mu_g\right)}{\sqrt{\sum_m \sum_n \left(f_{i+m,j+n} - \mu_f\right)^2} \sqrt{\left(g_{m,n} - \mu_g\right)^2}} \tag{5.24}$$

This is the expression through which the cross-correlation is evaluated for each position of the second level sub-frame, sliding pixel by pixel around the first level sub-frame.
Once the maximum value of $\hat{\Gamma}_{xy}$ is obtained for the pixel closest to the optimum point, if it assumable that the distance between the maximum pixel and the optimum point is reasonably smaller with respect to the integration intervals, i.e. $\Delta x \ll x_{max} - x_{min}$ and $\Delta y \ll y_{max} - y_{min}$, then the cross-correlation function can be extended through a Taylor series up to the second order:

$$\begin{aligned}\Gamma\left(\xi,\eta\right) \approx \Gamma\left(\Delta x, \Delta y\right) + \begin{pmatrix} \frac{\partial \Gamma}{\partial \xi} & \frac{\partial \Gamma}{\partial \eta} \end{pmatrix} \begin{pmatrix} \xi - \Delta x \\ \eta - \Delta y \end{pmatrix} + \\ + \frac{1}{2} \begin{pmatrix} \xi - \Delta x & \eta - \Delta y \end{pmatrix} \begin{bmatrix} \frac{\partial^2 \Gamma}{\partial \xi^2} & \frac{\partial^2 \Gamma}{\partial \xi \partial \eta} \\ \frac{\partial^2 \Gamma}{\partial \eta \partial \xi} & \frac{\partial^2 \Gamma}{\partial \eta^2} \end{bmatrix} \begin{pmatrix} \xi - \Delta x \\ \eta - \Delta y \end{pmatrix}\end{aligned} \tag{5.25}$$

that rewritten in a concise form becomes:

$$\Gamma\left(\xi,\eta\right) \approx \Gamma_0 + \boldsymbol{b}^T \boldsymbol{h} + \frac{1}{2} \boldsymbol{h}^T \boldsymbol{B} \boldsymbol{h} \tag{5.26}$$

which is a parabolic surface with maximum at $\xi = \Delta x$ and $\eta = \Delta y$.
$\boldsymbol{h} \triangleq \begin{pmatrix} \xi - \Delta x \\ \eta - \Delta y \end{pmatrix}$ represents the discrepancy between the exact position of the maximum and the one given by pixel resolution, as in Figure 5.24.
$\hat{\Gamma}_{MAX}\left(\xi,\eta\right)$ is the maximum found through the pixel resolution and $X_{OPT}\left(\Delta x, \Delta y\right)$ is the maximum to be found through the sub-pixel interpolation.
Through the known values of the cross-correlation function obtained in correspondence of the pixels, the curve fitting, based on the expression (5.26), is able to provide the value of the cross-correlation function through an interpolation procedure for any position, not necessarily corresponding to a specific pixel, accessing the sub-pixel level.

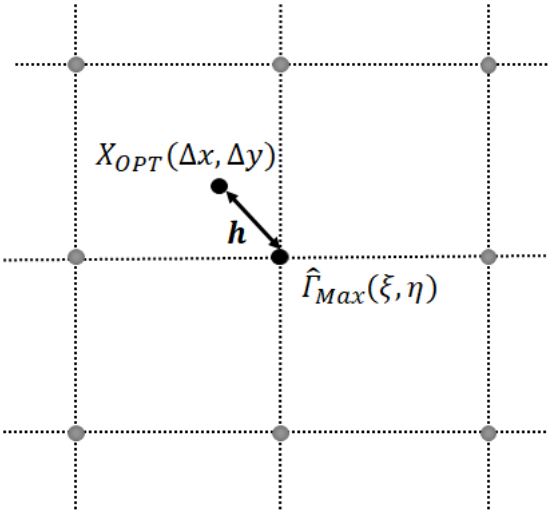

Figure 5.24. Optimum point through sub-pixel interpolation

The problem (5.26) can be rewritten as:

$$\Gamma\left(\xi_{i,j}, \eta_{i,j}\right) = \begin{pmatrix} 1 & h[1] & h[2] & \frac{1}{2}h[1]h[1] & h[1]h[2] & \frac{1}{2}h[2]h[2] \end{pmatrix} \begin{pmatrix} \Gamma_0 \\ b_1 \\ b_2 \\ B_{11} \\ B_{12} \\ B_{22} \end{pmatrix} \tag{5.27}$$

where $\boldsymbol{a} = \begin{pmatrix} \Gamma_0 & b_1 & b_2 & B_{11} & B_{12} & B_{22} \end{pmatrix}$ is the vector of the coefficients, with $B_{12} = B_{21}$ since $\dfrac{\partial^2\Gamma}{\partial\xi\partial\eta} = \dfrac{\partial^2\Gamma}{\partial\eta\partial\xi}$.
Solving for $\boldsymbol{a}$ implies finding the missing coefficients of equation (5.26). The spatial displacements Δx and Δy are such that

$$\frac{d\Gamma_{xy}(\xi,\eta)}{d\xi} = \frac{d\Gamma_{xy}(\xi,\eta)}{d\eta} = 0 \tag{5.28}$$

At this point, to find the optimal value, the only remaining step is the differentiation with respect to $\boldsymbol{h}$:

$$\frac{d\Gamma_{xy}(h)}{dh} = 0 \tag{5.29}$$

$\boldsymbol{Bh} = -\boldsymbol{b}$ and hence to $\boldsymbol{h} = -\boldsymbol{B}^{-1}\boldsymbol{b}$, which is the interpolated location of the maximum value.
Video processing is very useful when systems are too large or include many degrees of freedom, and thus would require a large number of sensors, when there is no room for sensors. Indeed, great advantages of this process are related to the small invasiveness, compared to the accelerometers apparatus, and the simple required set-up.

The here presented results regards only the step response excitation, as they are the most significant ones. For each frame, the sub-pixel interpolation rebuilds the displacement of any single mass in pixel and in time and it recreates its history. The result is a matrix whose columns correspond to the degrees of freedom and whose rows correspond to the time t: each entire column provides the history of the displacement for a specific mass. The Fourier Transform in space and time produces a dispersion surface. The importance of the dispersion curve is not only related to the chance of comparing experimental data with the theoretical findings, but is mainly associated to the possibility to identify the propagation regions and to evaluate phase and group velocity. However, the system is composed by too few degrees of freedom to obtain a high resolution dispersion curve. Indeed, when the Fourier Transform is applied, it translates the space dependency onto the wavenumber domain. Having available only few degrees of freedom implies few wavenumbers at which the dispersion curve is evaluated. Moreover, the accuracy of the obtained dispersion curve is further reduced when the FFT is performed in Matlab: the FFT has a domain defined from $-\infty$ to $+\infty$, and the data are split into a negative and a positive contribution; the FFT operation in Matlab translates the negative contribution in the positive range of the domain, but it is still only a reflection. This means that only half of the data are truly significant and can be employed. For this reason, the results are solely presented in terms of the displacement of the two waveguides, as showed in Figure 5.25, where the blue stems are associated to the displacement of the main waveguide and the orange ones to the second waveguide. The plot displays the displacement of the two entire waveguides at five different instants.

Even though the preliminary aspect of this experimental campaign has been dis-

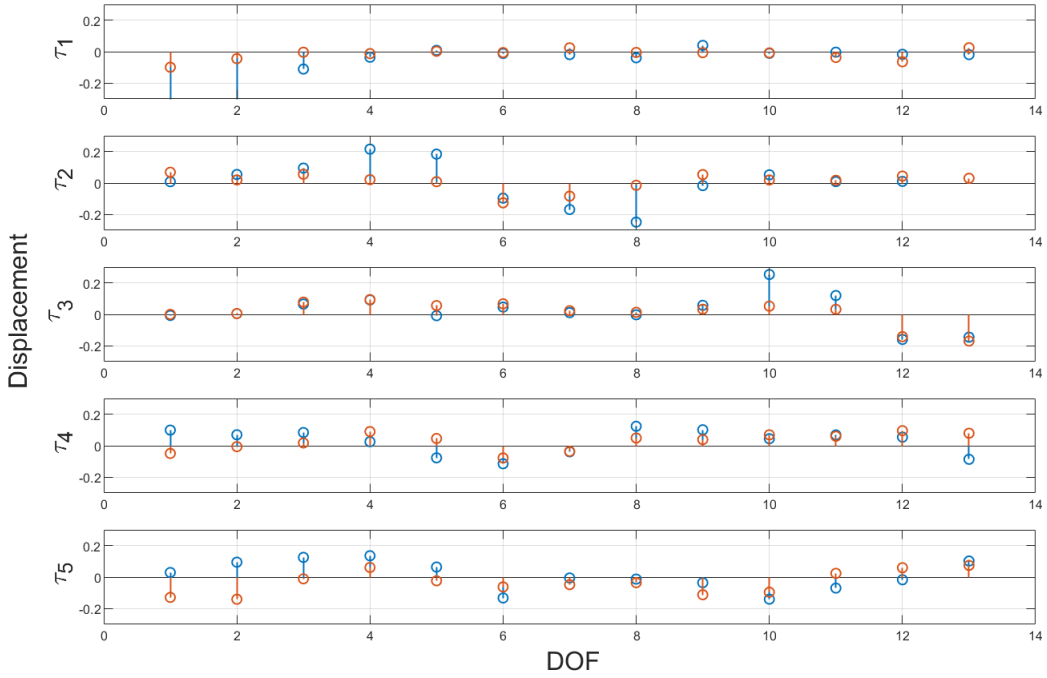

Figure 5.25. Displacement in the twin-wave system

cussed several times, the results already show interesting effects: first of all the propagation occurring in the second waveguide demonstrates the efficiency of the long-range coupling effect, even if the awaited phenomena do not emerge yet. Besides, the reaction of the second waveguide appears with a slowed down wave propagation and dispersion over its length. However, given the few degrees of freedom available and hence, due to the unavoidable poor resolution, this result can only be considered as an introductory representation of the twin-wave system.

Results are here presented also in terms of frequency response. Theoretically, to find the frequency response it could be sufficient to compare the output and input signals. However, the input itself is not perfect, and instead of being a perfect sinusoid, it presents more peaks in the frequency domain. This phenomenon finds its reasons in the presence of noise, and probably in the non perfect synchronization between the current sent to the voice coil and its reaction. Eventually, the two signals are not comparable as they are and the output signal modelling is crucial.
The Fit Sine procedure transforms the measured signal to a finite Fourier series with the addition of noise. It is assumed that the signal contains a base frequency and its multiplications, usually 1x...5x. The base frequency is not a priori known since the clock generating the sine wave, i.e. the input to the voice coil, has a finite resolution: even an error of a fraction of a Hz in the frequency leads to a huge error in the phase, when measuring a large amount of periods. The actual frequency is estimated with the non-linear least squares from the cleanest measured signal, usually the generator. The Sine Fit is a two-step approach:

- firstly the exact frequency is evaluated through a nonlinear least square method;
- then the signal is redefined, when its coefficients are obtained.

The aim of the first step is to find the exact frequency, which is used later to fit the output signal.
The non-linear least square method is the form of least squares analysis used to fit a set of observations with a model that is non-linear in a number of unknown parameters, smaller than the number of observations. The basis of the method is to approximate the model by a linear one and to redefine the parameters by successive iterations. The objective function is quadratic with respect to the parameters only in a region close to its minimum value, where the truncated Fourier series is a good approximation to the model. The more the parameter values differ from their optimal values, the more the contours deviate from elliptical shape. A consequence of this is that initial parameter estimates should be as close as practicable to their optimal values, even if unknown.
The used model here used is:

$$s(t) = a_1 \sin(b_1 t + c_1) \tag{5.30}$$

where b_1 is the exact frequency.
Once the exact frequency is estimated, the aim of the second step is to rebuild the output signals. Any signal can be written and considered as a Fourier series of

increasing orders of harmonic contributions:

$$s(t) = A_1 \sin \omega t + B_1 \cos \omega t + A_2 \sin 2\omega t + B_2 \cos 2\omega t + A_3 \sin 3\omega t + B_3 \cos 3\omega t + ... \tag{5.31}$$

where A_i and B_i are the coefficients related to the i-th order. The higher is the number of considered orders, the better is the approximation of the signal. The output signal, or actually any sinusoidal signal, for a single frequency, is described by two parameters only, i.e. the amplitude and the phase, and it can be written either as $\hat{s}(t) = A \sin \omega t + B \cos \omega t$ or as $\hat{s}(t) = C \cos(\omega t + \phi)$. The two formulations are equivalent since $C = \sqrt{A^2 + B^2}$ and $\phi = tg\frac{B}{A}$, but the first one is a linear model, and thus preferred. The goal is then to find A and B of all of the measured signals. To obtain an accurate estimation of these coefficients, equation 5.31 is used as it considers more than the first order.
The problem can be presented as:

$$\boldsymbol{y} = \begin{pmatrix} y_1 \\ \cdot \\ \cdot \\ \cdot \\ y_n \end{pmatrix} = \begin{bmatrix} \cos \omega t_1 & \sin \omega t_1 & \cos 2\omega t_1 & \sin 2\omega t_1 & \\ ... & ... & ... & ... & 1 \\ & & & & \end{bmatrix} \begin{pmatrix} A_1 \\ B_1 \\ A_2 \\ B_2 \\ A_0 \end{pmatrix} \tag{5.32}$$

which can be rewritten as: $\boldsymbol{y} = \boldsymbol{C}\boldsymbol{c}$, where n is the number of measured data, $\boldsymbol{y}$ is the vector of the measured data, $\boldsymbol{c}$ is the vector of the unknown coefficients and $\boldsymbol{C}$ is a matrix containing the coefficients of the model in equation (5.31), which are the more accurate, the higher is the considered order and which are known, since the frequency has been evaluated through the nonlinear least square method. The problem is easily solved through: $\boldsymbol{c} = \boldsymbol{C}^{-1}\boldsymbol{y}$. The output signal can now be redefined considering only the first order coefficients. This is based on the assumption that the higher orders are related to noise, but neglecting them from the beginning would have caused a worse approximation.
This procedure must be repeated for each degree of freedom, whose displacement has been measured. Once all the pairs A_l and B_l, where l indicates the l-th degree of freedom, are defined, the complex frequency response is straightforward to calculate.

$$H_{1,l} = \frac{(A_1 - iB_1)_l}{(A_1 - iB_1)_1} \tag{5.33}$$

and

$$H_{vc,l} = \frac{(A_1 - iB_1)_l}{(A_1 - iB_1)_v\, c} \tag{5.34}$$

where *vc* stands for voice coil. These expressions provide the frequency response obtained from the comparison between the l-th degree of freedom and the first degree of freedom in equation (5.33) and between the l-th degree of freedom and the voice coil in equation (5.34).
Figure 5.26 reports the complex frequency response of the three edge masses, compared to the voice coil input signal, calculated from 10 Hz up to 60 Hz. Instead of using a single step or multiple single step, a slow square wave excites the system and time domain average over all the steps is performed so to reduce the random

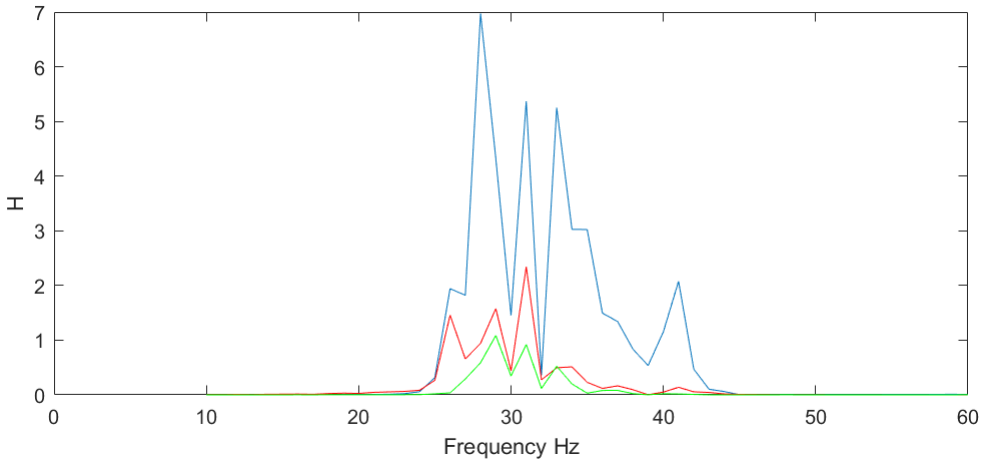

Figure 5.26. Frequency response

error. Even though the phase resolution is very poor, it clearly shows a group of natural frequencies occurring mainly in the range between 24 Hz and 40 Hz, in agreement with the results of the FEM analysis. Finally, regarding the resolution, note that about 10 frequencies are expected within a bandwidth of some Hz, which implies that about 10 crossings of 90 degrees should be measured within the bandwidth. This requires a very high resolution, due to the presence of many frequencies: indeed, if 10 is the minimum number of points per frequency, at least 100 points are needed for the entire frequency bandwidth and for a 5 Hz bandwidth, this means a 0.05 Hz resolution.

5.8 Final remarks

In this chapter, the case of the twin-wave system is analysed not only to complete the records of the long-range families, but also to present a first extension to a more complicated network of objects, anticipating the future application on large populations and on swarm dynamics. The mathematical model and numerical simulations are presented together with the FEM analysis and the experimental investigation.
The experimental campaign, even if at its earliest stage, is a useful tool to properly investigate the dynamic of the system. It enlightens the effect of the magnets, which are powerful enough to clearly couple the two waveguides, but probably not enough the give rise to the unconventional phenomena presented in the previous chapters. There are several aspects that can be enhanced for the future experiments. In this section, an overview of the main issues is presented.
Firstly, the FEM analysis should extend the magnetic interaction, coupling not only face-to-face masses, but also elements arranged diagonally with respect to the selected mass. A more accurate finite element analysis helps the understanding of the effects of the magnetic interaction and provides a more precise estimation of the natural frequencies of the system. A way to enhance the description of the magnetic interaction entails the manual modification of the mass and stiffness matrix, extrap-

olated from Ansys, adding the contributions of the magnetic interaction. Despite the guaranteed high level of accuracy the resulting matrices would reveal, this approach is not simple, since it involves the correction of the physical parameters of the degrees of freedom defined in the FEM.
Regarding the experimental set-up and in particular the twin-system itself, the number of used degrees of freedom should be enlarged. This brings two advantages: first of all, a larger system implies a larger amount of time before the wave reflections occur; this is important when the theoretical model finds its focus on infinite-size structures. Besides, to perform the dispersion curve through FFT, only half of the data can be beneficially used; hence, the larger is the number of employed degrees of freedom, the larger is the number of available wavenumbers and the better is the resolution of the dispersion curve.
A further consideration concerns the realization process. It must be noticed that inevitably the 3D printer has a limited preciseness and repetitiveness, both because the plastic material tends to shrink during the printing process and also because the high tolerances obtained with conventional materials, as steel and aluminium, cannot be achieved with PLA; this indicates that the masses are not all equal. Besides, as previously mentioned, the springs are made out by a unique piece that inserted in the basis, passes through the magnet holders. To be able to use this type of assembly, the strips have to be bended before they are linked to the masses. However, the process of inserting the strip in the magnet holders, since it is manually done and since the specific holes are not always precise for the aforementioned reasons, might cause further deformations of the strip, which have a random feature.
The greatest reason of discrepancy between the theoretical model and the experiments stands in the intrinsic nonlinearities of the system and in the assumption that the single waveguides can be considered one-dimensional. Several are the sources of nonlinearity, as they can refer to architectural imperfections or they can be addressed to the assumptions of the model. The main reasons of nonlinearity are:

- the presence of an offset in the alignment of the voice coil with the center of the face of the first mass;
- the stiffness of the springs depending upon the amplitudes of the vibrations, which causes a shift of the natural frequencies of the system. This aspect surely involves the the springs of the voice coil support that stiffen the higher is the amplitude of the vibrations, but it might also refer to the metal strips;
- the force input signal is not linear, both because it is not directly proportional to the current, but it is further affected by a higher order term, which, even though small, induces additional harmonics, and because of the intrinsic dynamics of its support;
- the magnetic coupling.

The effects of the nonlinearities due to architectural imperfections, namely the stiffness of the springs and voice coil dynamics, can be quantified through the Lissajous curve technique [117], which is often used to detect the nonlinearities of the experimental model. This method measures for any investigated frequency the

ratio between the output signal and the input signal, which in the case of a linear system is an elliptic curve. The frequency is chosen so to be the natural frequency of the object under analysis. Distortions of the elliptic curve unveil the presence of nonlinearities.
Furthermore, the theoretical model considers the waveguides as one-dimensional; however, the misalignment of the masses produces a motion in the transverse direction, with respect to the length of the waveguide. The system becomes two dimensional and cross-section effects influence the dispersion curve: in fact, in a two-dimensional system, to each frequency there is a set of associated wavenumbers that unveils the superposition of different modes.
A last consideration is about the post-processing analysis. The presented results are affected by a very poor resolution, which prevents a proper identification of the dispersion curve. Once the experimental set-up is appropriately improved, the tests should be run for different type of excitations, as each type brings its own advantages.

Chapter 6

Conclusions

This work investigates the effects of long-range interactions introduced in an elastic metamaterials on the dynamic response of a system. The main aspiration is the shaping of the desired dynamic response by tailoring the magnetic coupling.
The first chapter introduces the fundamental basis of the proposed theory: from the elasticity theory proposed by Navier and Cauchy, and the first digression about non localities presented by Brillouin and Kröner, to Eringen's nonlocal theory, the mathematical model is presented in its general form.
Several researches about long-range interaction and metamaterials have already been developed and many are the authors who steered the attention towards this new topics. Especially the topic of metamaterial can be tackled by different point of views, depending on their nature, whether they are acoustic, electromagnetic or mechanical. However, the combination of metamaterials and long-range interactions is an absolute novelty, and the newly arising concept of *elastic* metamaterial represents a breakthrough in the whole panorama of metamaterials.
Long-range interactions have the power to revolutionise the classical dynamics, anchored to short range connectivity and communication channels involving only close neighbour particles. The dynamics of systems equipped with long-range connections is described by an integral-differential equation, in which the convolution term is representative of their nonlocal nature, according to Eringen's theory.
A wide family of forces is considered, and in particular two types, i.e. Gauss-like and Laplace-like, induce a variety of unconventional propagation phenomena. These forces, described in terms of their nature and physical interpretation, act in addition to the classical short-range connections occurring between closest neighbours. They present three advantages, as they rapidly decay with the distance, they satisfy the action-reaction principle and their associated Fourier Transform is such that closed form analytical solutions are available for their dispersion relationship. These advantages makes these forces perfect candidates to mimic magnetic inclusions, which embedded within the matrix of a material, would practically produce long-range forces.
The willingness to define a general propagation behaviour related to the long-range interactions promotes the investigation of a simple one-dimensional waveguide. A complete theoretical analysis is presented: the nonlocal theory of Eringen is applied to Navier-Cauchy equations; a linearisation procedure, applied to long-

range forces modelled as power-law, guarantees the achievement of closed form analytical solutions of the dispersion relationship. The results, and especially the extraordinary emerging phenomena, are discussed in terms of a unique parameter χ, which provides a measure of the strength of the long-range forces. Indeed, since $\chi = \frac{E^*}{E}$, χ takes into account the ratio of the long-range elastic modulus $E^* = \frac{\mu\beta^3}{2\sqrt{2}}$ and the Young modulus E, where E^* can be either positive or negative, depending on the attractive or repulsive nature of the interaction force.
Varying of E^*, hence of χ, the results show three different scenarios:

- for large and negative χ wave-stopping arises and negative group velocity induces a backward propagation;
- for large and positive χ, after a region of instability because of the presence of imaginary solutions, superluminal propagation occurs due to the high values of the group velocity;
- for $|\chi|$ close to 1, a mode migration appears and modes are transported from high to low frequencies and vice versa.

The general feature of the forces is warranty of the universal representation of the propagation scenarios. This implies the legitimacy of the results for a wide class of both long-range forces and elastic metamaterials.
Since long-range interactions do not strongly interact with matter, their influence spread out across the surrounding environment, and they become messengers and communicating patterns, which might involve several objects. This work presents the simplest case of two identical waveguides, coupled with each other by the mean of the long-range interactions. However, the extension to more complicated systems, as even an entire population of single elements (swarm dynamics), is not pure imagination. The mathematical analysis applied on the *twin-wave* system duplicates the case of a single waveguide, and the results confirm the overall effectiveness of the approach, also to more complicated problems. FEM and experimental campaign, held at Technion, Israel Institute of Technology, further develop the investigation, unveiling more interesting properties of long-range interactions. The experimental campaign is surely at its earliest stage, but it is still useful to investigate the dynamic of the system.
The experimental campaign enlightens several aspects:

- the effect of the magnets is powerful enough to couple the two waveguides, but not enough the give rise to the unconventional propagation phenomena;
- a more accurate FEM modelling of the magnetic coupling is required so to extend the interaction to other elements and not only to face-to-face masses;
- a larger number of masses should be involved so to gain preciseness for the FFT evaluation and so to have longer time before reflections occur;
- several sources of nonlinearity are detected and they are related to structural imperfections of the 3D printed components and of the springs, manually assembled to the main structure, to the the presence of an offset in the alignment

of the voice coil with the center of the face of the first mass, to the stiffness of the springs depending upon the amplitudes of the vibrations, to the input signal, to the magnetic force;

- the theoretical model considers the waveguides as one-dimensional, but misalignments of the masses, producing a motion in the transverse direction, would transform the system in a two-dimensional one.

These considerations are the starting points of the future developments of this work, which firstly concern the follow-up of the experimental campaign. Besides, since the aim is to present a general theory about the propagation characteristics of long-range interactions embedded within elastic metamaterials, all the applied hypothesis, regarding linearity and special kernels, should be removed.

Appendix A

About the single distribution

A.1 Single spring

Given the system presented in Figure 4.1 and here reported for seek of clarity, the

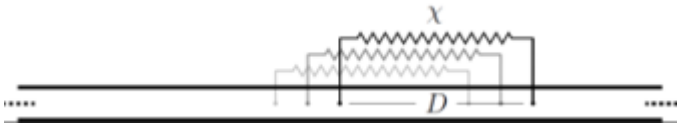

Figure A.1. Long-range as a single spring

related equation of motion is:

$$EA\frac{\partial^2 w(x,t)}{\partial x^2} - \rho A\frac{\partial^2 w(x,t)}{\partial t^2} + \chi\left[w(x) - w(x-D)\right] = 0 \tag{A.1}$$

To find the associated dispersion relationship, the displacement is assumed to be in the form: $w(x,t) = w_0 e^{j(kx-\omega t)}$. Substituting the displacement in equation (A.1), one obtains:

$$-\rho A\omega^2 + \chi\left(1 - e^{-jkD}\right) = 0 \tag{A.2}$$

If complex wavenumber are considered, it is admissible to set $k = k_R + jk_I$, which leads to:

$$\rho A\omega^2 - \chi\left(1 - e^{-j(k_R+jk_I)D}\right) = 0 \tag{A.3}$$

$$\rho A\omega^2 - \chi + \chi e^{-jk_R} e^{k_I D} = 0 \tag{A.4}$$

$$\rho A\omega^2 - \chi + \chi\left(\cos k_R D - j\sin k_R D\right) e^{k_I D} = 0 \tag{A.5}$$

Dividing real and imaginary part of equation (A.5), the following system is given:

$$\begin{cases} \rho A\omega^2 - \chi + \chi\cos k_R D e^{k_I D} = 0 \\ -\chi j \sin k_R D e^{k_I D} = 0 \end{cases}$$

Conditions on the wavenumber are sought: from the second equation $k_R^{(n)} = \dfrac{\pi n}{D}$ is obtained; substituted in the first equation of the system, it leads to:

$$\rho A\omega^2 - \chi + \chi(-1)^n e^{k_I D} = 0 \tag{A.6}$$

Considering that $\omega_n^2 = \dfrac{\rho A}{\chi}$ is the natural frequency of the single oscillator, the condition on the imaginary part of the wavenumber is:

$$k_I^{(n)} = \frac{1}{D} \ln \frac{1 - \frac{\omega^2}{\omega_n^2}}{(-1)^n} \tag{A.7}$$

This equation can be interpreted in terms of the frequency ω as well: $\Omega^2 = \left(\dfrac{\omega}{\omega_n}\right)^2 = 1 - e^{k_I D} \cos k_R D$, where still $\omega_n^2 = \dfrac{\rho A}{\chi}$.
This implies an infinite set of wavenumbers for any given value of the frequency ω.

A.2 Double spring

In the same way, also the case of a double spring, as in Figure 4.2, is reported.
The related equation of motion is:

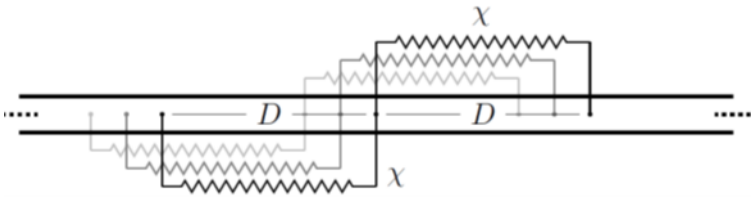

Figure A.2. Long-range as a double spring

$$EA\frac{\partial^2 w(x,t)}{\partial x^2} - \rho A\frac{\partial^2 w(x,t)}{\partial t^2} + \chi\left[w(x) - w(x-D)\right] + \chi\left[w(x+D) - w(x)\right] = 0 \tag{A.8}$$

Eliminating the contribution of the short-range forces, and assuming the displacement once again in the form $w(x,t) = w_0 e^{j(kx-\omega t)}$, equation (A.8) can be rewritten as:

$$\rho A\omega^2 + \chi\left(1 - e^{-jkD}\right) + \chi\left(e^{jkD} - 1\right) = 0 \tag{A.9}$$

$$\rho A\omega^2 + \chi\left(-e^{-jkD} + e^{jkD}\right) = 0 \tag{A.10}$$

For complex wavenumber $k = k_R + jk_I$, the dispersion relationship becomes:

$$\rho A\omega^2 + \chi\left(-e^{-jk_R D}e^{k_I D} + e^{jk_R D}e^{-k_I D}\right) = 0 \tag{A.11}$$

$$\rho A\omega^2 + \chi\left[-e^{k_I D}\left(\cos k_R D - j\sin k_R D\right) + e^{-k_I D}\left(\cos k_R D + j\sin k_R D\right)\right] = 0 \tag{A.12}$$

and finally:

$$\rho A\omega^2 + \chi\left[-2\cos k_R D \sinh k_I D + j2\sin k_R D \cosh k_I D\right] = 0 \tag{A.13}$$

Separation of real and imaginary part of equation (A.13) leads to:

$$\begin{cases} \rho A\omega^2 + \chi \left[\cos k_R D \left(e^{-k_I D} - e^{k_I D}\right)\right] = 0 \\ \chi j \sin k_R D \left(e^{-k_I D} + e^{k_I D}\right) = 0 \end{cases} \tag{A.14}$$

$$\begin{cases} \rho A\omega^2 - 2\chi \cos k_R D \sinh k_I D = 0 \\ \sin k_R D \cosh k_I D = 0 \end{cases} \tag{A.15}$$

To find the conditions on the wavenumber, from the second equation of the system (A.15) $k_R^{(n)} = \dfrac{\pi n}{D}$ is extracted; when inserted in the first equation, the condition on the imaginary part is achieved:

$$\begin{cases} k_R^{(n)} = \dfrac{\pi n}{D} \\ k_I^{(n)} = \dfrac{1}{D} \operatorname{arcsinh} \dfrac{\rho A\omega^2}{2\chi} \dfrac{1}{(-1)^n} \end{cases} \tag{A.16}$$

The second relation can be also interpreted in terms of the frequency ω: $\Omega^2 = \left(\dfrac{\omega}{\omega_n}\right)^2 = 2\cos k_R D \sinh k_I D$, where $\omega_n^2 = \dfrac{\rho A}{\chi}$.
As for the single spring, even this case shows the existence of an infinite number of values of the wavenumber for any single frequency.

Appendix B

Nondimensional dispersion relationship

$$\rho\frac{\partial^2 w}{\partial t^2} - E\frac{\partial^2 w}{\partial x^2} - g(x) * w(x) = 0 \tag{B.1}$$

The Fourier transform in space and time of the previous equation, for the Gauss-like force, leads to:

$$-\rho\omega^2\hat{\hat{w}} + Ek^2\hat{\hat{w}} - \frac{\mu\beta^3k^2}{2\sqrt{2}}e^{-\frac{\beta^2k^2}{4}}\hat{\hat{w}} = 0 \tag{B.2}$$

Dividing all terms by E and multiplying by β^2 produces:

$$\frac{\rho}{E}\beta^2\omega^2 - k^2\beta^2 + \frac{\mu\beta^3}{E2\sqrt{2}}\beta^2k^2e^{-\frac{\beta^2k^2}{4}} = 0 \tag{B.3}$$

Introducing the nondimensional parameters $\Omega = \sqrt{\frac{\rho}{E}}\beta\omega$, $K = \beta k$ and $\chi = \frac{\mu\beta^3}{2\sqrt{2}E}$, the resulting nondimensional relationship is:

$$\Omega^2 + K^2\left(\chi e^{-\frac{K^2}{4}} - 1\right) = 0 \tag{B.4}$$

Appendix C

Nondimensional dispersion relationship with viscous term

$$\rho\frac{\partial^2 w}{\partial t^2}+\gamma\frac{\partial w}{\partial t}-E\frac{\partial^2 w}{\partial x^2}-g(x)*w(x)=0 \tag{C.1}$$

The Fourier transform in space and time of the previous equation, for the Gauss-like force, leads to:

$$-\rho\omega^2\hat{\tilde{w}}-j\gamma\omega\hat{\tilde{w}}+Ek^2\hat{\tilde{w}}-\frac{\mu\beta^3k^2}{2\sqrt{2}}e^{-\frac{\beta^2k^2}{4}}\hat{\tilde{w}}=0 \tag{C.2}$$

Dividing all terms by E and multiplying by β^2 one obtains:

$$\frac{\rho}{E}\beta^2\omega^2+j\frac{\beta^2\gamma}{E}\omega-k^2\beta^2+\frac{\mu\beta^3}{E2\sqrt{2}}\beta^2k^2e^{-\frac{\beta^2k^2}{4}}=0 \tag{C.3}$$

Some nondimensional parameters are straightforward to define; indeed, $\Omega=\sqrt{\frac{\rho}{E}}\beta\omega$, $K=\beta k$ and $\chi=\frac{\mu\beta^3}{2\sqrt{2}E}$. The viscous term requires few mathematical passages:

$$\frac{\beta^2\gamma}{E}\omega=\frac{\beta\omega}{\sqrt{E}}\frac{\gamma\beta}{\sqrt{E}}=\beta\omega\frac{\sqrt{\rho}}{\sqrt{E}}\frac{\gamma\beta}{\sqrt{\rho E}} \tag{C.4}$$

the first term is Ω and the second one is Γ that from now on will measure the intensity of the dissipation contribution.
The resulting nondimensional relationship is:

$$\Omega=-j\frac{\Gamma}{2}\pm\sqrt{Q^2-\left(\frac{\Gamma}{2}\right)^2} \tag{C.5}$$

where $\Gamma=\frac{\gamma\beta}{\sqrt{\rho E}}$, $Q^2=K^2[1-\chi\phi(K)]$ and $\phi(K)=e^{-\frac{K^2}{4}}$ for the Gaussian case.
The group velocity is, in general, complex:

$$C_g=\frac{\partial\Omega}{\partial K}=\pm\frac{1}{\sqrt{1-\left(\frac{\Gamma}{2Q}\right)^2}}\frac{\partial Q}{\partial K}=\pm\frac{1}{\sqrt{1-\left(\frac{\Gamma}{2Q}\right)^2}}C_{g_{\Gamma=0}} \tag{C.6}$$

Appendix D

Interbody force

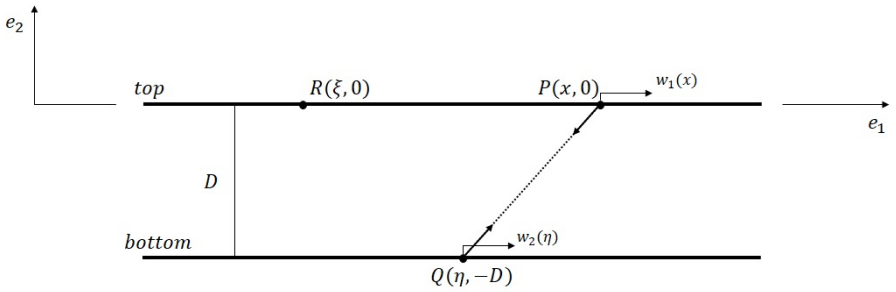

Figure D.1. Twin-waves model

First the geometrical parameters are defined.
Definition of the position vectors:
The coordinates of the point $\boldsymbol{P}$:

$$\boldsymbol{x} = \begin{pmatrix} x_1 \\ x_2 \end{pmatrix} = \begin{pmatrix} x \\ 0 \end{pmatrix}$$

The coordinates of the point $\boldsymbol{R}$:

$$\boldsymbol{\xi} = \begin{pmatrix} \xi_1 \\ \xi_2 \end{pmatrix} = \begin{pmatrix} \xi \\ 0 \end{pmatrix}$$

The coordinates of the point $\boldsymbol{Q}$:

$$\boldsymbol{\eta} = \begin{pmatrix} \eta_1 \\ \eta_2 \end{pmatrix} = \begin{pmatrix} \eta \\ -D \end{pmatrix}$$

Definition of the displacement vectors:
displacement within a single waveguide:

$$\boldsymbol{\varepsilon_s} = \begin{pmatrix} w_1(x) - w_2(\xi) \\ 0 \end{pmatrix}$$

displacement of the twin system:

$$\boldsymbol{\varepsilon_{cr}} = \begin{pmatrix} w_1(x) - w_2(\eta) \\ 0 \end{pmatrix}$$

Definition of the distance vectors:
distance between $\boldsymbol{P}$ and $\boldsymbol{R}$

$$\boldsymbol{r_s} = \boldsymbol{x} - \boldsymbol{\xi} + \boldsymbol{\varepsilon_s} = \begin{pmatrix} x_1 - \xi_1 + \varepsilon_{s1} \\ x_2 - \xi_2 + \varepsilon_{s2} \end{pmatrix} = \begin{pmatrix} x - \xi + \varepsilon_{s1} \\ 0 \end{pmatrix}$$

distance between $\boldsymbol{P}$ and $\boldsymbol{Q}$

$$\boldsymbol{r_{cr}} = \boldsymbol{x} - \boldsymbol{\eta} + \boldsymbol{\varepsilon_c r} = \begin{pmatrix} x_1 - \eta_1 + \varepsilon_{cr1} \\ x_2 - \eta_2 + \varepsilon_{cr2} \end{pmatrix} = \begin{pmatrix} x - \eta + \varepsilon_{cr1} \\ D \end{pmatrix}$$

modulus $|\boldsymbol{r}| = \left[(x - \eta + \varepsilon_{cr1})^2 + D^2 \right]^{\frac{1}{2}}$
distance between $\boldsymbol{P}$ and $\boldsymbol{Q}$

$$\boldsymbol{r_0} = \boldsymbol{x} - \boldsymbol{\eta} = \begin{pmatrix} x - \eta \\ D \end{pmatrix}$$

For the Gauss-like force $F(r) = \mu r e^{-\left(\frac{r}{\beta}\right)^2}$, the analytical expressions of the two long-range contributions f_0 and h_0 within the same waveguide are:

$$f_0 = \mu e^{-\left(\frac{|r_0|}{\beta}\right)^2} \tag{D.1}$$

$$\boldsymbol{h_0} = \left. \frac{\partial f\left(|\boldsymbol{r_{cr}}|\right)}{\partial |\boldsymbol{r_{cr}}|} \right|_{\boldsymbol{\varepsilon_{cr}}} \frac{(\boldsymbol{x} - \boldsymbol{\eta}) \otimes (\boldsymbol{x} - \boldsymbol{\eta})}{|\boldsymbol{x} - \boldsymbol{\eta}|} \tag{D.2}$$

Expliciting the components:

$$\boldsymbol{h_0} = -\mu \frac{2}{\beta^2} e^{-\left(\frac{|r_0|}{\beta}\right)^2} \begin{bmatrix} (x - \eta)^2 & (x - \eta) D \\ D (x - \eta) & D^2 \end{bmatrix} \tag{D.3}$$

Since

$$\boldsymbol{F}(\boldsymbol{r}) = f(|\boldsymbol{r}|) \boldsymbol{r} = f_0 \cdot (\boldsymbol{x} - \boldsymbol{\eta}) + \boldsymbol{h_0 \varepsilon_d} + f_0 \boldsymbol{\varepsilon_d} \tag{D.4}$$

then

$$\boldsymbol{F}(\boldsymbol{r}) = \mu e^{-\left(\frac{|r_0|}{\beta}\right)^2} \begin{bmatrix} (x - \eta) - \frac{2}{\beta^2} (x - \eta)^2 [w_1(x) - w_2(\eta)] + [w_1(x) - w_2(\eta)] \\ D - \frac{2}{\beta^2} D (x - \eta) \end{bmatrix} \tag{D.5}$$

The integral term of the equation becomes:

$$\int_{\eta\in\mathbb{R}} \mu e^{-\left(\frac{D}{\beta}\right)^2} e^{-\frac{(x-\eta)^2}{\beta^2}} (x-\eta)\, d\eta - w_1(x) \int_{\eta\in\mathbb{R}} \mu e^{-\left(\frac{D}{\beta}\right)^2} e^{-\frac{(x-\eta)^2}{\beta^2}} \left[1 - \frac{2}{\beta^2}(x-\eta)^2\right] d\eta + \int_{\eta\in\mathbb{R}} \mu e^{-\left(\frac{D}{\beta}\right)^2} e^{-\frac{(x-\eta)^2}{\beta^2}} \left[1 - \frac{2}{\beta^2}(x-\eta)^2\right] w_2(\eta)\, d\eta \quad \text{(D.6)}$$

Only the third integral brings a non-null contribution and can be rewritten as:

$$-\left[h_{011} + f_0\right](x) * w_2(x) \quad \text{(D.7)}$$

or alternatively:

$$-l(x) * w_2(x) \quad \text{(D.8)}$$

This represents the long-range contribution due to the bottom waveguide on the upper one.

Appendix E

Effective stiffness of the twin-wave model

The measured magnetic force is:

$$F_M = C_1 + C_2 \frac{1}{x^4} \tag{E.1}$$

with $C_1 = 7.45[N]$ and $C_2 = 1.2610^5[N * m^4]$. To obtain the values of the stiffness, the magnetic force must be linearised according to equation (3.24):

$$f(|\boldsymbol{r}|)\boldsymbol{r} \sim (\boldsymbol{x} - \boldsymbol{\xi})\, f_0 + \boldsymbol{h}_0 \boldsymbol{\varepsilon} + f_0 \boldsymbol{\varepsilon} \tag{E.2}$$

In this way, the force can be interpreted as $F = Kx$, where K is the value of the effective stiffness.
The resulting values are $k_x = 4.92 \frac{N}{m}$ and $k_y = 16.9 \frac{N}{m}$.
The effective stiffness depends on the mutual distance between the magnets, as shown in Figure E.1. According to Figure E.1, the matrix of the distances is:

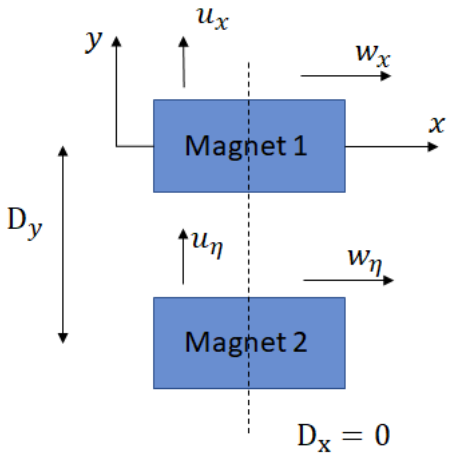

Figure E.1. Magnet position

$$\begin{bmatrix} D_x^2 & D_x D_y \\ D_y D_x & D_y^2 \end{bmatrix} = \begin{bmatrix} 0 & 0 \\ 0 & (30mm)^2 \end{bmatrix} \tag{E.3}$$

The only two terms of the linearised force that should be considered are $\boldsymbol{h}_0\boldsymbol{\varepsilon}$ and $f_0\boldsymbol{\varepsilon}$:

$$f_0\boldsymbol{\varepsilon} = \frac{C_2}{|x_0|^5}\begin{bmatrix} w(x) - w(\eta) \\ u(x) - u(\eta) \end{bmatrix} \tag{E.4}$$

and

$$\boldsymbol{h}_0\boldsymbol{\varepsilon} = -\frac{5C_2}{|x_0|^7}10^{-6}\begin{bmatrix} 0 & 0 \\ 0 & (30mm)^2 \end{bmatrix}\begin{bmatrix} w(x) - w(\eta) \\ u(x) - u(\eta) \end{bmatrix} \tag{E.5}$$

Combining the two contributions, two equations are obtain: one associated to the first row, which related to the x axis provides the effective stiffness k_x, and one associated to the second row that, related to the y axis, leads to the effective stiffness k_y. Indeed,

$$F_x = \frac{C_2}{|x_0|^5}\left[w(x) - w(\eta)\right] \tag{E.6}$$

produces $k_x = \dfrac{C_2}{|x_0|^5} = 4.92\dfrac{N}{m}$ and

$$F_y = \frac{C_2}{|x_0|^5}\left[u(x) - u(\eta)\right] - \frac{5C_2}{|x_0|^7}10^{-6}D_y^2\left[u(x) - u(\eta)\right] \tag{E.7}$$

provides $k_y = \dfrac{C_2}{|x_0|^5}\left[1 - \dfrac{5}{|x_0|^2}10^{-6}D_y^2\right] = 16.9\,\dfrac{N}{m}$.

Appendix F

Modes shape

In this section, most of the obtained modes are reported. The displacement is not real scale. As mentioned in the paragraph related to the FEM analysis, modes related to the two waveguides appear very close to each other, with gaps of tenths of Hz.

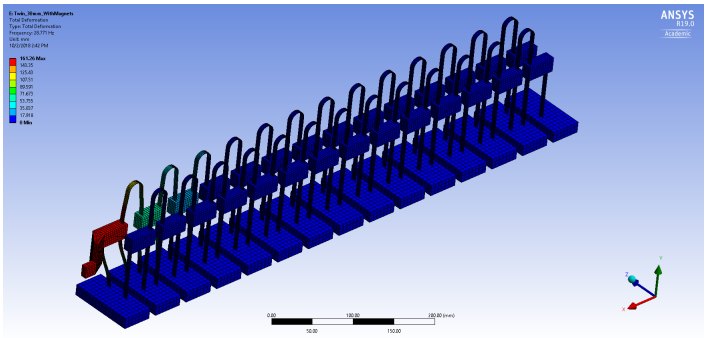

Figure F.1. 28.771 Hz

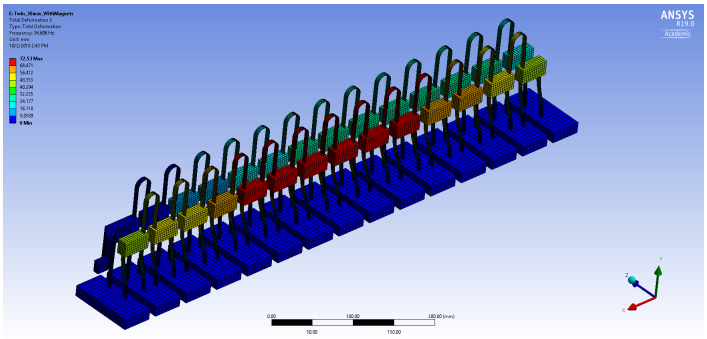

Figure F.2. 36.6 Hz

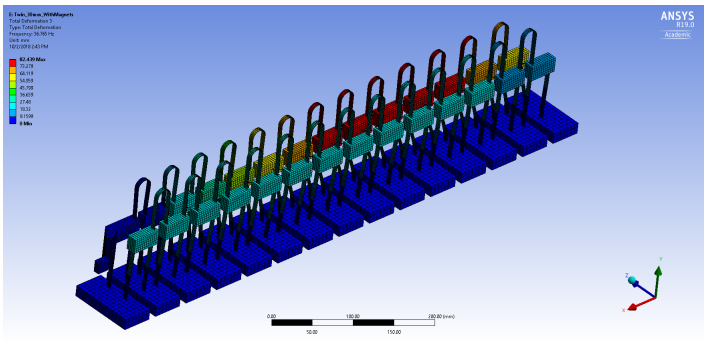

Figure F.3. 36.75 Hz

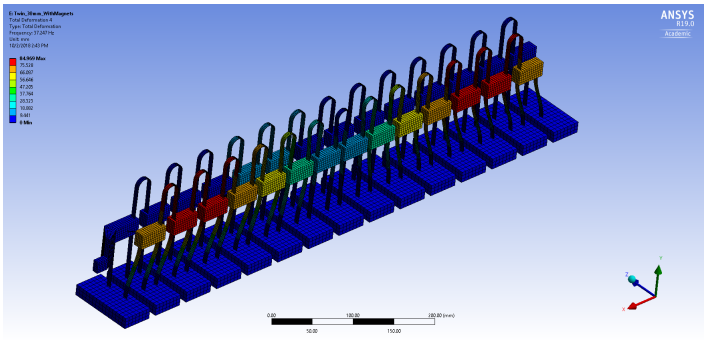

Figure F.4. 37.247 Hz

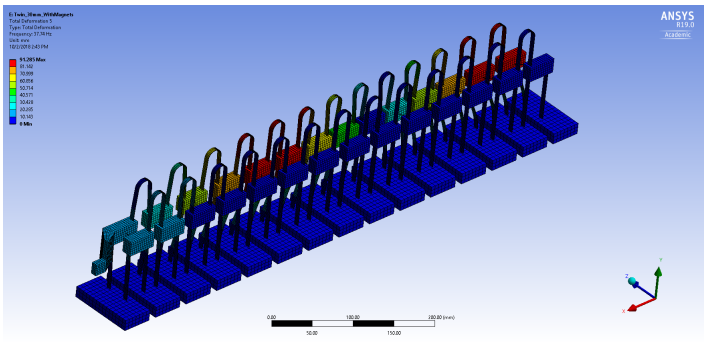

Figure F.5. 37.74 Hz

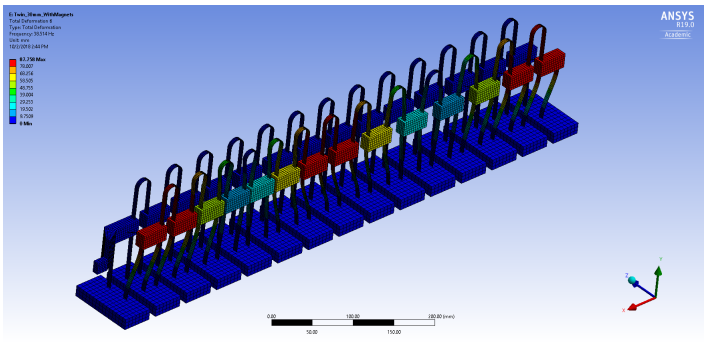

Figure F.6. 38.514 Hz

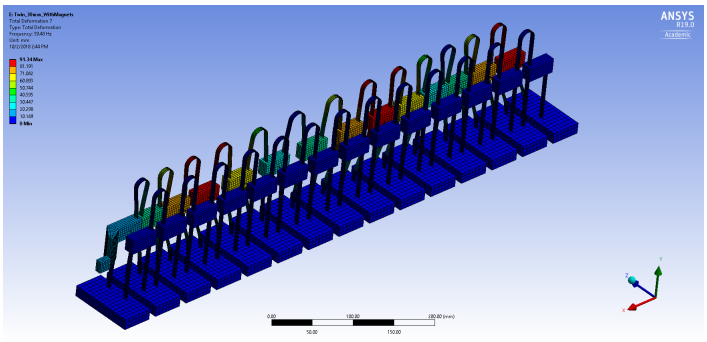

Figure F.7. 39.48 Hz

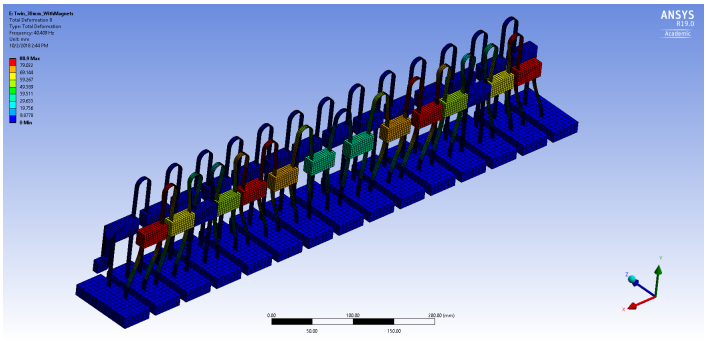

Figure F.8. 40.409 Hz

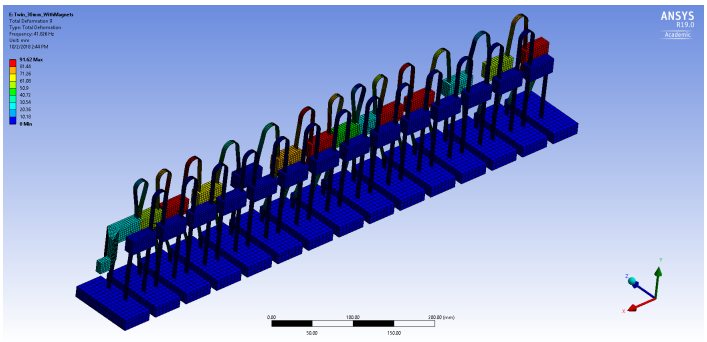

Figure F.9. 41.826 Hz

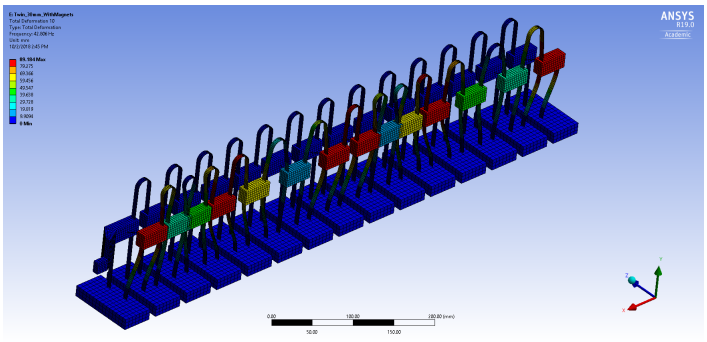

Figure F.10. 42.806 Hz

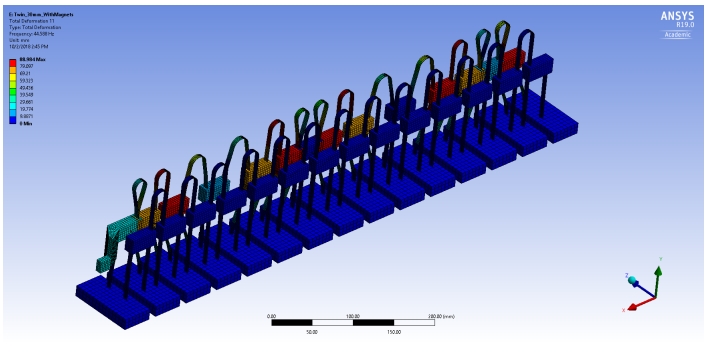

Figure F.11. 44.588 Hz

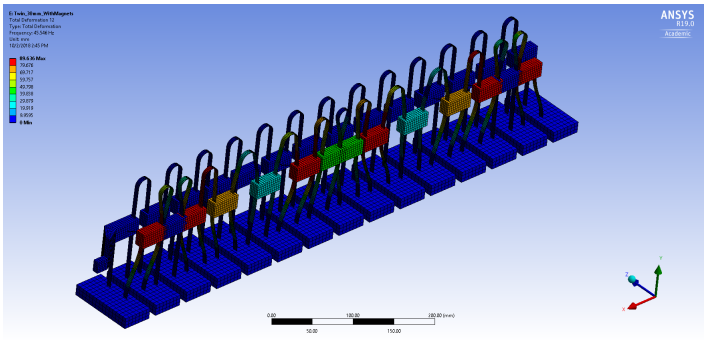

Figure F.12. 45.546 Hz

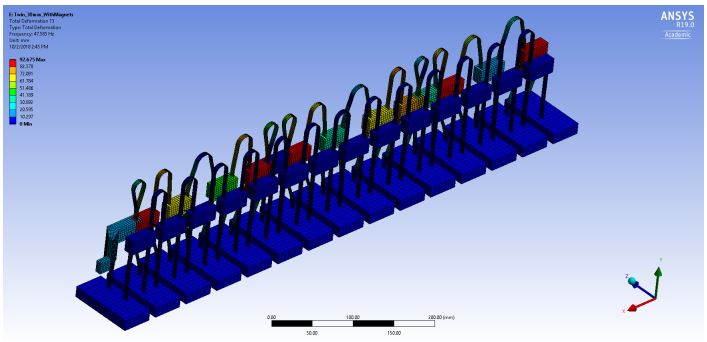

Figure F.13. 47.583 Hz

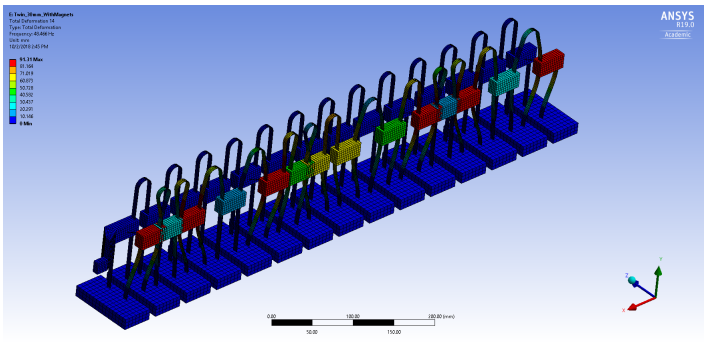

Figure F.14. 48.466 Hz

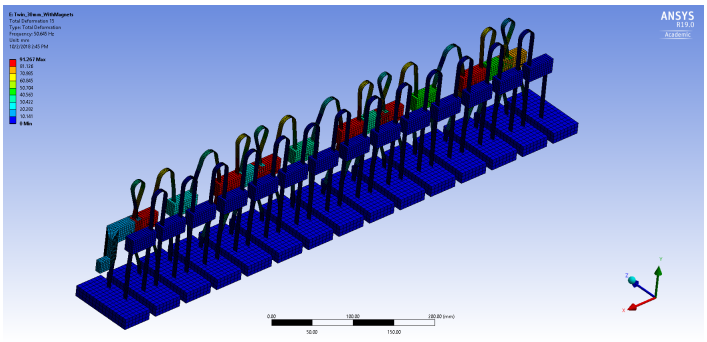

Figure F.15. 50.645 Hz

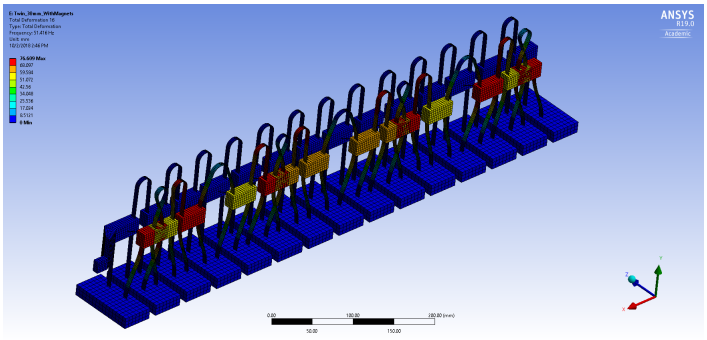

Figure F.16. 51.416 Hz

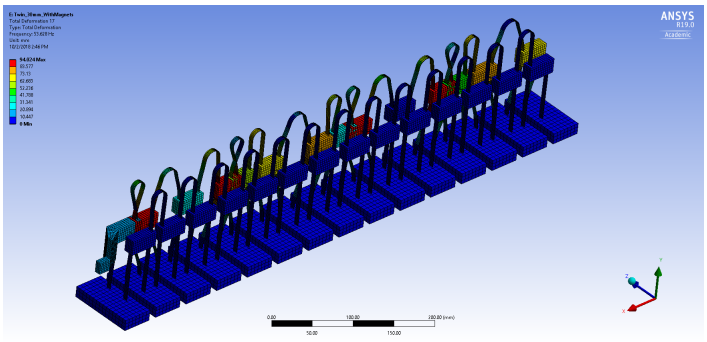

Figure F.17. 53.628 Hz

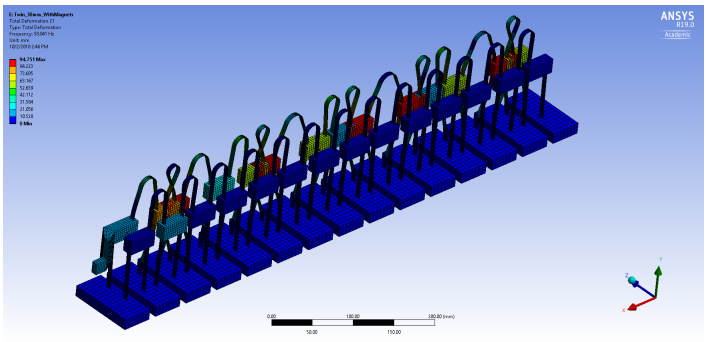

Figure F.18. 58.841 Hz

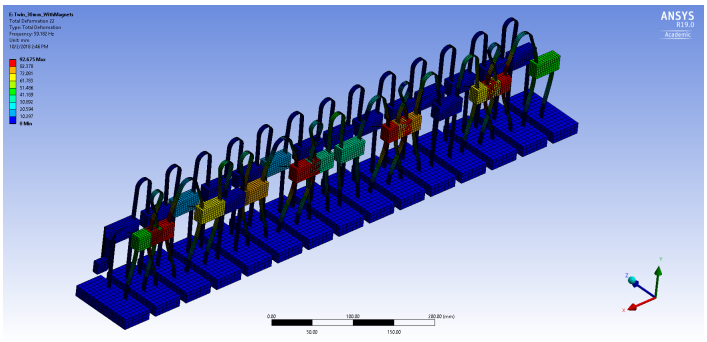

Figure F.19. 59.182 Hz

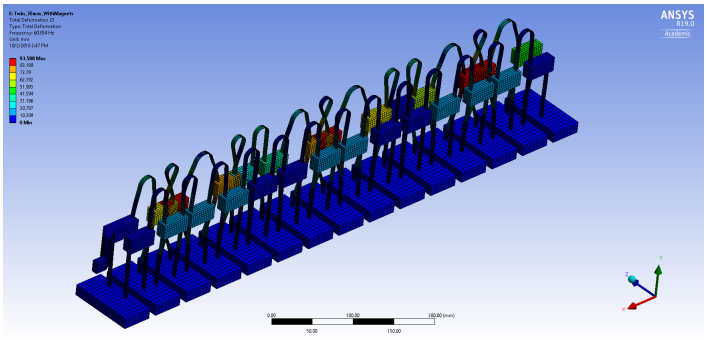

Figure F.20. 60.854 Hz

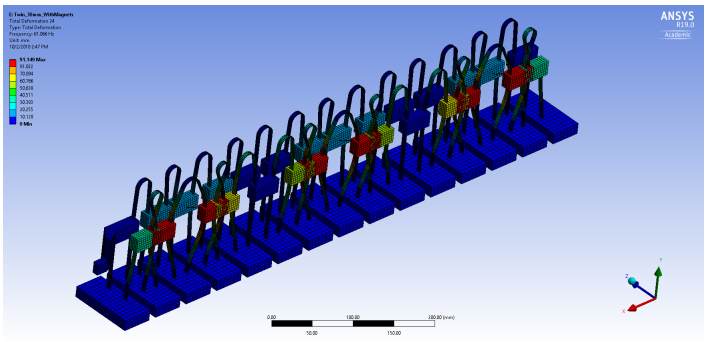

Figure F.21. 61.066 Hz

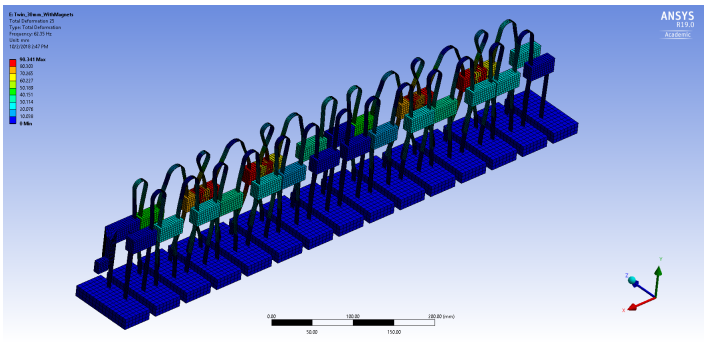

Figure F.22. 62.35 Hz

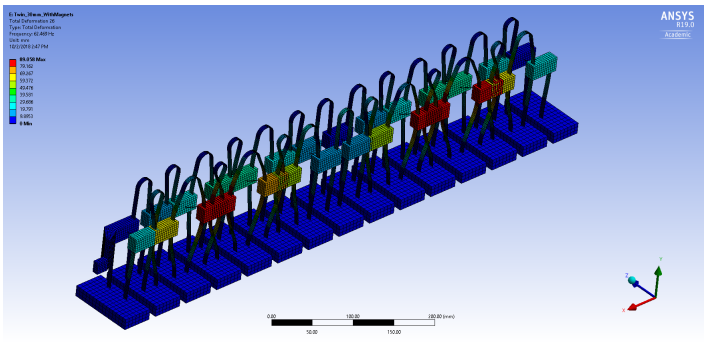

Figure F.23. 62.469 Hz

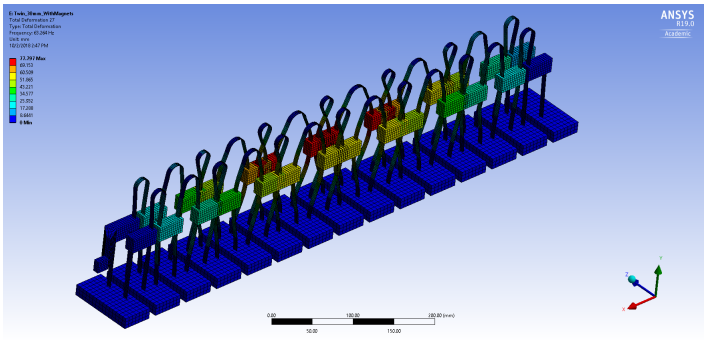

Figure F.24. 63.264 Hz

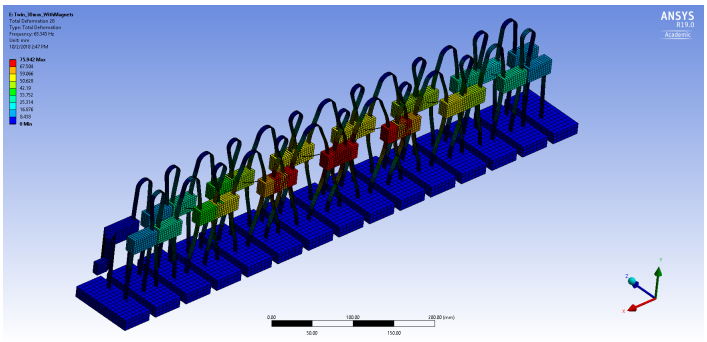

Figure F.25. 63.343 Hz

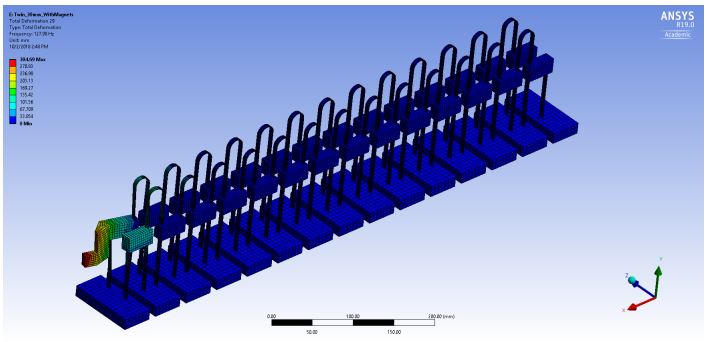

Figure F.26. 127.98 Hz

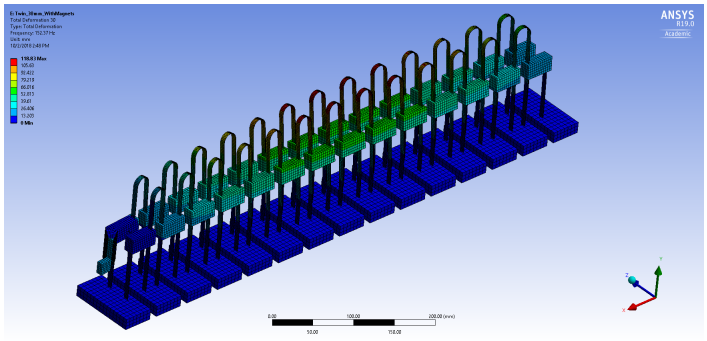

(a) Isometric view

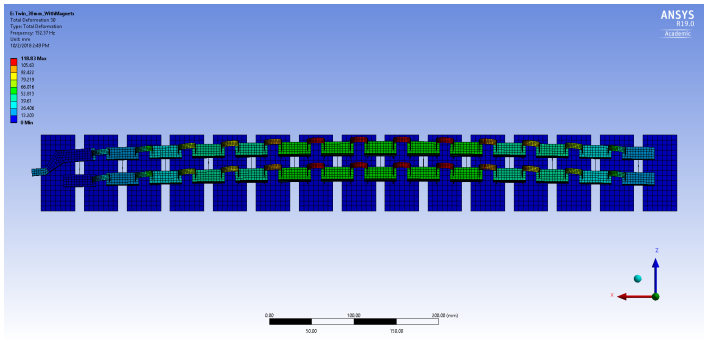

(b) Top view

Figure F.27. 152.37 Hz

Bibliography

[1] L. L. Spada, F. Bilotti, and L. Vegni, "Metamaterial biosensor for cancer detection," in *2011 IEEE SENSORS Proceedings*, IEEE, oct 2011.

[2] A. Dubey and T. Shami, "Metamaterials in electromagnetic wave absorbers," *Defence Science Journal*, vol. 62, pp. 261–268, jul 2012.

[3] S. Zhang, *Acoustic metamaterial design and applications*. PhD thesis, University of Illinois at Urbana-Champaign, 2010.

[4] Y. Tao and G. Wang, "Hyperthermia of large superficial tumor with a flat LHM lens," in *2012 IEEE/MTT-S International Microwave Symposium Digest*, IEEE, jun 2012.

[5] Y. Shang and R. Bouffanais, "Influence of the number of topologically interacting neighbors on swarm dynamics," *Scientific Reports*, vol. 4, feb 2014.

[6] C. N. Parker and S. E. Halford, "Dynamics of long-range interactions on DNA: the speed of synapsis during site-specific recombination by resolvase," *Cell*, vol. 66, no. 4, pp. 781–791, 1991.

[7] A. Carcaterra, F. Dell'Isola, R. Esposito, and M. Pulvirenti, "Macroscopic description of microscopically strongly inhomogenous systems: a mathematical basis for the synthesis of higher gradients metamaterials," *Archive for Rational Mechanics and Analysis*, vol. 218, no. 3, pp. 1239–1262, 2015.

[8] D. Schurig, J. J. Mock, B. J. Justice, S. A. Cummer, J. B. Pendry, A. F. Starr, and D. R. Smith, "Metamaterial electromagnetic cloak at microwave frequencies," *Science*, vol. 314, pp. 977–980, nov 2006.

[9] J. Hunt, J. Gollub, T. Driscoll, G. Lipworth, A. Mrozack, M. S. Reynolds, D. J. Brady, and D. R. Smith, "Metamaterial microwave holographic imaging system," *Journal of the Optical Society of America A*, vol. 31, p. 2109, sep 2014.

[10] D. Ye, Y. Salamin, J. Huangfu, S. Qiao, G. Zheng, and L. Ran, "Observation of wave packet distortion during a negative-group-velocity transmission," *Scientific reports*, vol. 5, p. 8100, 2015.

[11] D. Ye, G. Zheng, J. Wang, Z. Wang, S. Qiao, J. Huangfu, and L. Ran, "Negative group velocity in the absence of absorption resonance," *Scientific reports*, vol. 3, p. 1628, 2013.

[12] D. M. Storch, M. Van den Worm, and M. Kastner, "Interplay of soundcone and supersonic propagation in lattice models with power law interactions," *New Journal of Physics*, vol. 17, no. 6, p. 063021, 2015.

[13] J. Qu, A. Gerber, F. Mayer, M. Kadic, and M. Wegener, "Experiments on metamaterials with negative effective static compressibility," *Physical Review X*, vol. 7, no. 4, p. 041060, 2017.

[14] N. Brunner, V. Scarani, M. Wegmüller, M. Legré, and N. Gisin, "Direct measurement of superluminal group velocity and signal velocity in an optical fiber," *Physical review letters*, vol. 93, no. 20, p. 203902, 2004.

[15] K. L. Tsakmakidis, T. W. Pickering, J. M. Hamm, A. F. Page, and O. Hess, "Completely stopped and dispersionless light in plasmonic waveguides," *Physical review letters*, vol. 112, no. 16, p. 167401, 2014.

[16] M. F. Yanik and S. Fan, "Stopping light all optically," *Physical review letters*, vol. 92, no. 8, p. 083901, 2004.

[17] D. E. Chang, A. H. Safavi-Naeini, M. Hafezi, and O. Painter, "Slowing and stopping light using an optomechanical crystal array," *New Journal of Physics*, vol. 13, no. 2, p. 023003, 2011.

[18] A. D. Neira, G. A. Wurtz, and A. V. Zayats, "Superluminal and stopped light due to mode coupling in confined hyperbolic metamaterial waveguides," *Scientific reports*, vol. 5, p. 17678, 2015.

[19] M. I. N. Rosa, J. R. de França Arruda, and M. Ruzzene, "Investigating interface modes on periodic acoustic waveguides and elastic rods using spectral elements," in *Lecture Notes in Mechanical Engineering*, pp. 501–510, Springer International Publishing, jul 2018.

[20] P. Kerrian, A. Hanford, D. Capone, and S. Miller, "Acoustic ground cloaks revisited," *The Journal of the Acoustical Society of America*, vol. 137, pp. 2299–2299, apr 2015.

[21] P. Kerrian, A. Hanford, B. Beck, and D. Capone, "Underwater acoustic ground cloak development and demonstration," *The Journal of the Acoustical Society of America*, vol. 143, pp. 1918–1918, mar 2018.

[22] B. Beck, A. Hanford, and P. Kerrian, "Metamaterial ground cloak with anisotropic solid inclusions," *The Journal of the Acoustical Society of America*, vol. 140, pp. 3104–3104, oct 2016.

[23] T. A. Schaedler, A. J. Jacobsen, A. Torrents, A. E. Sorensen, J. Lian, J. R. Greer, L. Valdevit, and W. B. Carter, "Ultralight metallic microlattices," *Science*, vol. 334, pp. 962–965, nov 2011.

[24] J. Bauer, S. Hengsbach, I. Tesari, R. Schwaiger, and O. Kraft, "High-strength cellular ceramic composites with 3D microarchitecture," *Proceedings of the National Academy of Sciences*, vol. 111, pp. 2453–2458, feb 2014.

[25] A. Madeo, P. Neff, I.-D. Ghiba, and G. Rosi, "Reflection and transmission of elastic waves in non-local band-gap metamaterials: a comprehensive study via the relaxed micromorphic model," *Journal of the Mechanics and Physics of Solids*, vol. 95, pp. 441–479, oct 2016.

[26] N. Roveri, A. Carcaterra, and A. Akay, "Vibration absorption using non-dissipative complex attachments with impacts and parametric stiffness," *The Journal of the Acoustical Society of America*, vol. 126, pp. 2306–2314, nov 2009.

[27] A. Carcaterra, A. Akay, and I. M. Koç, "Near-irreversibility in a conservative linear structure with singularity points in its modal density," *The Journal of the Acoustical Society of America*, vol. 119, pp. 2141–2149, apr 2006.

[28] A. Carcaterra and A. Akay, "Fluctuation-dissipation and energy properties of a finite bath," *Physical Review E*, vol. 93, no. 3, p. 032142, 2016.

[29] A. Carcaterra and A. Akay, "Dissipation in a finite-size bath," *Physical Review E*, vol. 84, no. 1, p. 011121, 2011.

[30] A. Carcaterra, A. Akay, and C. Bernardini, "Trapping of vibration energy into a set of resonators: theory and application to aerospace structures," *Mechanical Systems and Signal Processing*, vol. 26, pp. 1–14, jan 2012.

[31] A. Carcaterra, F. Coppo, F. Mezzani, and S. Pensalfini, "Long-range elastic metamaterials," *The Journal of the Acoustical Society of America*, vol. 141, pp. 3744–3744, may 2017.

[32] X. N. Liu, G. K. Hu, G. L. Huang, and C. T. Sun, "An elastic metamaterial with simultaneously negative mass density and bulk modulus," *Applied Physics Letters*, vol. 98, p. 251907, jun 2011.

[33] S. Yao, X. Zhou, and G. Hu, "Experimental study on negative effective mass in a 1D mass-spring system," *New Journal of Physics*, vol. 10, p. 043020, apr 2008.

[34] V. A. Eremeyev, L. P. Lebedev, and H. Altenbach, *Foundations of micropolar mechanics*. Springer Science & Business Media, 2012.

[35] A. C. Eringen, "Linear theory of micropolar elasticity," *Journal of Mathematics and Mechanics*, pp. 909–923, 1966.

[36] A. C. Eringen, "Plane waves in nonlocal micropolar elasticity," *International Journal of Engineering Science*, vol. 22, no. 8-10, pp. 1113–1121, 1984.

[37] S. Pensalfini, F. Coppo, F. Mezzani, G. Pepe, and A. Carcaterra, "Optimal control theory based design of elasto-magnetic metamaterial," *Procedia Engineering*, vol. 199, pp. 1761–1766, 2017.

[38] B. P. Abbott, R. Abbott, T. D. Abbott, and et al., "Multi-messenger observations of a binary neutron star merger," *The Astrophysical Journal*, vol. 848, p. L12, oct 2017.

[39] E. Kröner, "Elasticity theory of materials with long range cohesive forces," *International Journal of Solids and Structures*, vol. 3, pp. 731–742, sep 1967.

[40] A. C. Eringen, "On differential equations of nonlocal elasticity and solutions of screw dislocation and surface waves," *Journal of Applied Physics*, vol. 54, pp. 4703–4710, sep 1983.

[41] A. C. Eringen, "Linear theory of nonlocal elasticity and dispersion of plane waves," *International Journal of Engineering Science*, vol. 10, no. 5, pp. 425–435, 1972.

[42] F. Coppo, A. S. Rezaei, and A. Mezzani F. Pensalfini S. Carcaterra, "Waves path in an elastic membrane with selective nonlocality," in *ISMA 2018 Proceedings*, 2018.

[43] A. Carcaterra, F. Coppo, F. Mezzani, and S. Pensalfini, "Long-range retarded elastic metamaterials: wave-stopping, negative and hypersonic group velocity," *Physical Review Applied*, Under review.

[44] M. Di Paola, G. Failla, A. Pirrotta, A. Sofi, and M. Zingales, "The mechanically based non-local elasticity: an overview of main results and future challenges," *Phil. Trans. R. Soc. A*, vol. 371, no. 1993, p. 20120433, 2013.

[45] M. D. Paola, A. Pirrotta, and M. Zingales, "Mechanically-based approach to non-local elasticity: variational principles," *International Journal of Solids and Structures*, vol. 47, pp. 539–548, mar 2010.

[46] G. Gottone, M. D. Paola, and M. Zingales, "Dynamics of non-local systems handled by fractional calculus," *Advances in Numerical Methods*, 2009.

[47] M. D. Paola, G. Failia, and M. Zingales, "Physically-based approach to non-local elasticity," *Journal of Elasticity*, 2008.

[48] V. E. Tarasov and G. M. Zaslavsky, "Conservation laws and Hamilton's equations for systems with long-range interaction and memory," *Communications in Nonlinear Science and Numerical Simulation*, vol. 13, pp. 1860–1878, nov 2008.

[49] V. E. Tarasov and G. M. Zaslavsky, "Fractional dynamics of systems with long-range interaction," *Communications in Nonlinear Science and Numerical Simulation*, vol. 11, pp. 885–898, dec 2006.

[50] V. E. Tarasov and G. M. Zaslavsky, "Fractional dynamics of coupled oscillators with long-range interaction," *Chaos: An Interdisciplinary Journal of Nonlinear Science*, vol. 16, no. 2, p. 023110, 2006.

[51] V. E. Tarasov, "Continuous limit of discrete systems with long-range interaction," *Journal of Physics A: Mathematical and General*, vol. 39, no. 48, p. 14895, 2006.

[52] V. E. Tarasov, "Lattice model of fractional gradient and integral elasticity: long-range interaction of grünwald-letnikov-riesz type," *Mechanics of Materials*, vol. 70, pp. 106–114, mar 2014.

[53] V. E. Tarasov, "Lattice with long-range interaction of power-law type for fractional non-local elasticity," *International Journal of Solids and Structures*, vol. 51, pp. 2900–2907, aug 2014.

[54] N. Korabel, G. M. Zaslavsky, and V. E. Tarasov, "Coupled oscillators with power-law interaction and their fractional dynamics analogues," *Communications in Nonlinear Science and Numerical Simulation*, vol. 12, pp. 1405–1417, dec 2007.

[55] S. Gupta and S. Ruffo, "The world of long-range interactions: a bird's eye view," *International Journal of Modern Physics A*, vol. 32, p. 1741018, mar 2017.

[56] J. G. Ángyán, I. C. Gerber, A. Savin, and J. Toulouse, "Van der Waals forces in density functional theory: perturbational long-range electron-interaction corrections," *Physical Review A*, vol. 72, jul 2005.

[57] M. Decker, N. Feth, C. M. Soukoulis, S. Linden, and M. Wegener, "Retarded long-range interaction in split-ring-resonator square arrays," *Physical Review B*, vol. 84, aug 2011.

[58] M. Maródi, F. d'Ovidio, and T. Vicsek, "Synchronization of oscillators with long range interaction: phase transition and anomalous finite size effects," *Physical Review E*, vol. 66, jul 2002.

[59] S. Flach, "Breathers on lattices with long range interaction," *Physical Review E*, vol. 58, pp. R4116–R4119, oct 1998.

[60] A. V. Shytov, D. A. Abanin, and L. S. Levitov, "Long-range interaction between adatoms in graphene," *Physical review letters*, vol. 103, no. 1, p. 016806, 2009.

[61] S. Tanaka and H. A. Scheraga, "Medium- and long-range interaction parameters between amino acids for predicting three-dimensional structures of proteins," *Macromolecules*, vol. 9, pp. 945–950, nov 1976.

[62] Y. Tawada, T. Tsuneda, S. Yanagisawa, T. Yanai, and K. Hirao, "A long-range-corrected time-dependent density functional theory," *The Journal of Chemical Physics*, vol. 120, pp. 8425–8433, may 2004.

[63] S. Nambu and D. A. Sagala, "Domain formation and elastic long-range interaction in ferroelectric perovskites," *Physical Review B*, vol. 50, pp. 5838–5847, sep 1994.

[64] T. Leininger, H. Stoll, H.-J. Werner, and A. Savin, "Combining long-range configuration interaction with short-range density functionals," *Chemical Physics Letters*, vol. 275, pp. 151–160, aug 1997.

[65] J. Israelachvili and R. Pashley, "The hydrophobic interaction is long range, decaying exponentially with distance," *Nature*, vol. 300, no. 5890, pp. 341–342, 1982.

[66] N. Kawakami and S.-K. Yang, "Finite-size scaling in one-dimensional quantum liquid with long-range interaction," *Physical Review Letters*, vol. 67, pp. 2493–2496, oct 1991.

[67] D. T. Son, "Superconductivity by long-range color magnetic interaction in high-density quark matter," *Physical Review D*, vol. 59, apr 1999.

[68] M. Goulian, R. Bruinsma, and P. Pincus, "Long-range forces in heterogeneous fluid membranes," *EPL (Europhysics Letters)*, vol. 22, no. 2, p. 145, 1993.

[69] A. Sanyal, B. R. Lajoie, G. Jain, and J. Dekker, "The long-range interaction landscape of gene promoters," *Nature*, vol. 489, no. 7414, p. 109, 2012.

[70] J. Kotakoski, A. V. Krasheninnikov, and K. Nordlund, "Energetics, structure, and long-range interaction of vacancy-type defects in carbon nanotubes: atomistic simulations," *Physical Review B*, vol. 74, dec 2006.

[71] K. Smith and L. F. Mollenauer, "Experimental observation of soliton interaction over long fiber paths: discovery of a long-range interaction," *Optics Letters*, vol. 14, p. 1284, nov 1989.

[72] S. F. Mingaleev, Y. S. Kivshar, and R. A. Sammut, "Long-range interaction and nonlinear localized modes in photonic crystal waveguides," *Physical Review E*, vol. 62, pp. 5777–5782, oct 2000.

[73] E. M. Dianov, A. V. Luchnikov, A. N. Pilipetskii, and A. M. Prokhorov, "Long-range interaction of picosecond solitons through excitation of acoustic waves in optical fibers," *Applied Physics B*, vol. 54, no. 2, pp. 175–180, 1992.

[74] D. Gorbonos, R. Ianconescu, J. G. Puckett, R. Ni, N. T. Ouellette, and N. S. Gov, "Long-range acoustic interactions in insect swarms: an adaptive gravity model," *New Journal of Physics*, vol. 18, p. 073042, jul 2016.

[75] R. C. Fetecau, Y. Huang, and T. Kolokolnikov, "Swarm dynamics and equilibria for a nonlocal aggregation model," *Nonlinearity*, vol. 24, pp. 2681–2716, aug 2011.

[76] N. Roveri, S. Pensalfini, and A. Carcaterra, "Small-world based interactions in elastic metamaterials," in *ISMA 2018 Proceedings*, 2018.

[77] D. Helbing, A. Hennecke, V. Shvetsov, and M. Treiber, "Micro-and macrosimulation of freeway traffic," *Mathematical and computer modelling*, vol. 35, no. 5-6, pp. 517–547, 2002.

[78] H. Gayathri, P. Aparna, and A. Verma, "A review of studies on understanding crowd dynamics in the context of crowd safety in mass religious gatherings," *International Journal of Disaster Risk Reduction*, 2017.

[79] D. Helbing and P. Molnar, "Social force model for pedestrian dynamics," *Physical review E*, vol. 51, no. 5, p. 4282, 1995.

[80] D. Beli, J. R. F. Arruda, and M. Ruzzene, "Wave propagation in elastic metamaterial beams and plates with interconnected resonators," *International Journal of Solids and Structures*, vol. 139-140, pp. 105–120, may 2018.

[81] A. Madeo, G. Barbagallo, M. V. d'Agostino, L. Placidi, and P. Neff, "First evidence of non-locality in real band-gap metamaterials: determining parameters in the relaxed micromorphic model," in *Proc. R. Soc. A*, vol. 472, p. 20160169, The Royal Society, 2016.

[82] F. Mezzani, F. Coppo, and A. Carcaterra, "Long-range coupling of waveguides," in *ISMA 2018 Proceedings*, 2018.

[83] F. Mezzani, F. Coppo, S. Pensalfini, N. Roveri, and A. Carcaterra, "Twin-waves propagation phenomena in magnetically-coupled structures," *Procedia engineering*, vol. 199, pp. 711–716, 2017.

[84] A. A. Vlasov, "On high-frequency properties of electron gas," *Journal of Experimental and Theoretical Physics*, vol. 8, no. 3, pp. 291–318, 1938.

[85] F. Bouchet, S. Gupta, and D. Mukamel, "Thermodynamics and dynamics of systems with long-range interactions," *Physica A: Statistical Mechanics and its Applications*, vol. 389, no. 20, pp. 4389–4405, 2010.

[86] A. Carcaterra, N. Roveri, and A. Akay, "Connectivity in waves and vibrations: one-to-six, one-to-all, all-to-all and random connections," in *ISMA 2018 Proceedings*, 2018.

[87] A. D. Pierce, "Resonant-frequency-distribution of internal mass inferred from mechanical impedance matrices, with application to fuzzy structure theory," *Journal of Vibration and Acoustics*, vol. 119, pp. 324–333, 07 1997.

[88] A. O. Caldeira and A. J. Leggett, "Path integral approach to quantum Brownian motion," *Physica A: Statistical mechanics and its Applications*, vol. 121, no. 3, pp. 587–616, 1983.

[89] F. Jauffred, R. Onofrio, and B. Sundaram, "Universal and anomalous behavior in the thermalization of strongly interacting harmonically trapped gas mixtures," *Journal of Physics B: Atomic, Molecular and Optical Physics*, vol. 50, no. 13, p. 135005, 2017.

[90] R. P. Feynman and F. L. Vernon Jr, "The theory of a general quantum system interacting with a linear dissipative system," *Annals of physics*, vol. 281, no. 1-2, pp. 547–607, 2000.

[91] V. D. Vaidya, Y. Guo, R. M. Kroeze, K. E. Ballantine, A. J. Kollár, J. Keeling, and B. L. Lev, "Tunable-range, photon-mediated atomic interactions in multimode cavity QED," *Physical Review X*, vol. 8, no. 1, p. 011002, 2018.

[92] S. Puri, C. K. Andersen, A. L. Grimsmo, and A. Blais, "Quantum annealing with a network of all-to-all connected, two-photon driven Kerr nonlinear oscillators," *arXiv preprint arXiv:1609.07117*, 2016.

[93] A. Carcaterra and A. Akay, "Theoretical foundations of apparent-damping phenomena and nearly irreversible energy exchange in linear conservative systems," *The Journal of the Acoustical Society of America*, vol. 121, pp. 1971–1982, apr 2007.

[94] I. M. Koç, A. Carcaterra, Z. Xu, and A. Akay, "Energy sinks: vibration absorption by an optimal set of undamped oscillators," *The Journal of the Acoustical Society of America*, vol. 118, pp. 3031–3042, nov 2005.

[95] Y. I. Bobrovnitskii, "Energy characteristics of oscillatory systems with internal (Hidden) degrees of freedom," *Acoustical Physics*, vol. 59, pp. 1–5, jan 2013.

[96] L. Brillouin, *Wave propagation in periodic structures: electric filters and crystal lattices*. Courier Corporation, 2003.

[97] M. Zingales, "Wave propagation in 1d elastic solids in presence of long-range central interactions," *Journal of Sound and Vibration*, vol. 330, pp. 3973–3989, aug 2011.

[98] M. D. Paola and M. Zingales, "Long-range cohesive interactions of non-local continuum faced by fractional calculus," *International Journal of Solids and Structures*, vol. 45, pp. 5642–5659, oct 2008.

[99] V. E. Tarasov, "Theoretical physics models with integro-differentiation of fractional order," *IKI, RCD*, 2011.

[100] A. Carcaterra and A. Akay, "Transient energy exchange between a primary structure and a set of oscillators: return time and apparent damping," *The Journal of the Acoustical Society of America*, vol. 115, pp. 683–696, feb 2004.

[101] N. Challamel, L. Rakotomanana, and L. Le Marrec, "A dispersive wave equation using nonlocal elasticity," *Comptes Rendus Mécanique*, vol. 337, no. 8, pp. 591–595, 2009.

[102] D. Del Vescovo and I. Giorgio, "Dynamic problems for metamaterials: review of existing models and ideas for further research," *International Journal of Engineering Science*, vol. 80, pp. 153–172, 2014.

[103] A. E. H. Love, *A treatise on the mathematical theory of elasticity*. Cambridge university press, 2013.

[104] M. Reiner, "Elasticity beyond the elastic limit," *American Journal of Mathematics*, vol. 70, p. 433, apr 1948.

[105] S. A. Shan and Q. Haque, "Low frequency electrostatic nonlinear structures in an inhomogeneous magnetized non-maxwellian electron–positron–ion plasma," *Physics Letters A*, vol. 382, no. 2-3, pp. 99–105, 2018.

[106] K. Okamoto, *Fundamentals of optical waveguides*. Academic press, 2006.

[107] E. J. Skudrzyk, B. R. Kautz, and D. C. Greene, "Vibration of, and bending-wave propagation in plates," *The Journal of the Acoustical Society of America*, vol. 33, pp. 36–45, jan 1961.

[108] F. J. Fahy and P. Gardonio, *Sound and structural vibration: radiation, transmission and response*. Elsevier, 2007.

[109] Y. K. Cheung, *Finite strip method in structural analysis*. Elsevier, 2013.

[110] T. Kaneko, "On Timoshenko's correction for shear in vibrating beams," *Journal of Physics D: Applied Physics*, vol. 8, pp. 1927–1936, nov 1975.

[111] C. G. J. Vreedenburgh, "The shell with double curvature considered as a plate on an elastic foundation," 1962.

[112] L. Brillouin, *Wave propagation and group velocity*, vol. 8. Academic Press, 2013.

[113] A. K. LJ Wang and A. Dogariu, "Gain-assisted superluminal light propagation," *Nature (London)*, vol. 406, p. 277, 2000.

[114] A. K. A. Dogariu and L. J. Wang, "Transparent anomalous dispersion and superluminal light-pulse propagation at a negative group velocity," *PHYSICAL REVIEW A, VOLUME 63, 053806*, 2001.

[115] A. D. A. Kuzmich and L. J. Wang, "Signal velocity, causality, and quantum noise in superluminal light pulse propagation," *PHYSICAL REVIEW LETTERS*, 2001.

[116] P. Lax and B. Wendroff, "Systems of conservation laws," *Communications on Pure and Applied Mathematics*, vol. 13, pp. 217–237, may 1960.

[117] H. A. H. Al-Khazali and M. R. Askari, "Geometrical and graphical representations analysis of lissajous figures in rotor dynamic system," *IOSR Journal of Engineering*, vol. 2, no. 05, pp. 971–978, 2012.